SENIOR HONORS THESIS IN ENGINEERING

Algorithm for Detection of Spikes in the Small Intestine

Investigating the Effects of Induced Ischemia on Small Intestine Electrical Activity

By Raisa Velasco Castedo

Thesis Advisor: Dr. Jonathan C. Erickson

Department of Physics and Engineering

Washington and Lee University

May, 2012

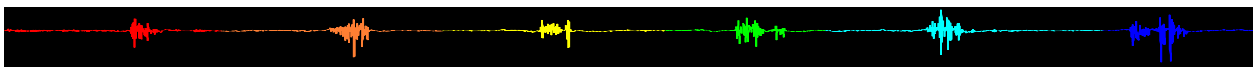

Contents

ABSTRACT

This thesis presents an algorithm for spike detection designed to analyze data from induced ischemia experiments. Algorithm design and validation are discussed in detail. Other topics addressed include: electrical activity in the small intestine, electro-mechanical coupling in the intestine, observations during intestinal ischemia, previous spike detection methods, induced ischemia experimental details, signal contamination, need for automated method, algorithm performance analysis, and possible applications of the algorithm for future research.

Chapter 1

Introduction

1.1 The Digestive System and the Small Intestine

The human digestive system processes food into components useful for the body. Digestion is extremely important as it provides the nutrients and energy required for proper cell functioning. The digestive tract is composed of the: mouth, pharynx, esophagus, stomach, small intestine, large intestine, rectum and anus (figure 1.1). Disease affecting any of these regions in the digestive tract will have negative effects on digestion. It is important for scientists and health professionals to understand the functions of the digestive tract and how disease disrupts these functions. This study focuses on the small intestine and investigates its myoelectrical activity as a possible indicator of disease.

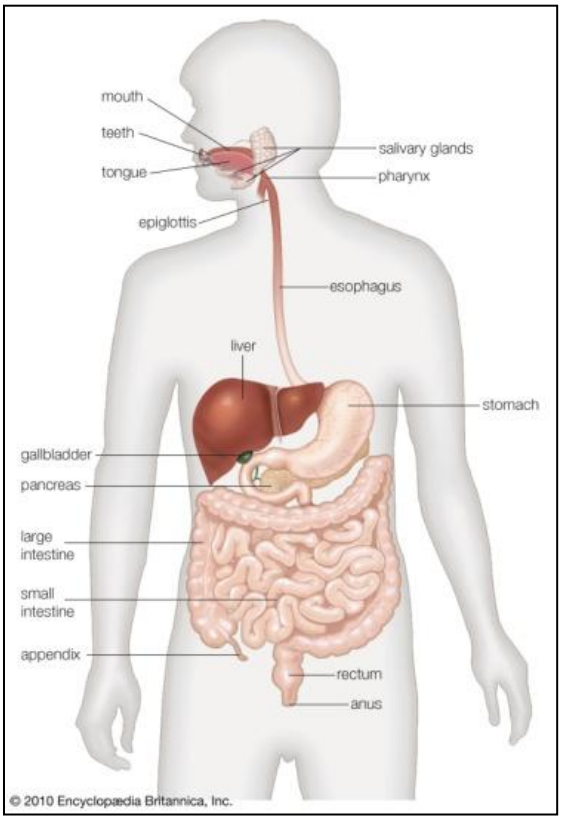

Figure 1.1. Digestive System [Source: Encyclopedia Britannica]

http://www.britannica.com/EBchecked/media/1087/The-human-digestive-system-as-seen-from-the-front

The small intestine is part of the gastrointestinal (GI) tract and it is divided into three segments: the duodenum, jejunum and ileum (figure 1.2). The majority of chemical digestion and nutrient absorption take place in the small intestine. The duodenum carries on the food break down process while the jejunum and ileum are responsible for mechanical mixing, nutrient diffusion into the bloodstream and waste motility in the anal direction. Mechanical mixing and waste motility are accomplished through waves of muscular contraction and relaxation; a process called peristalsis.

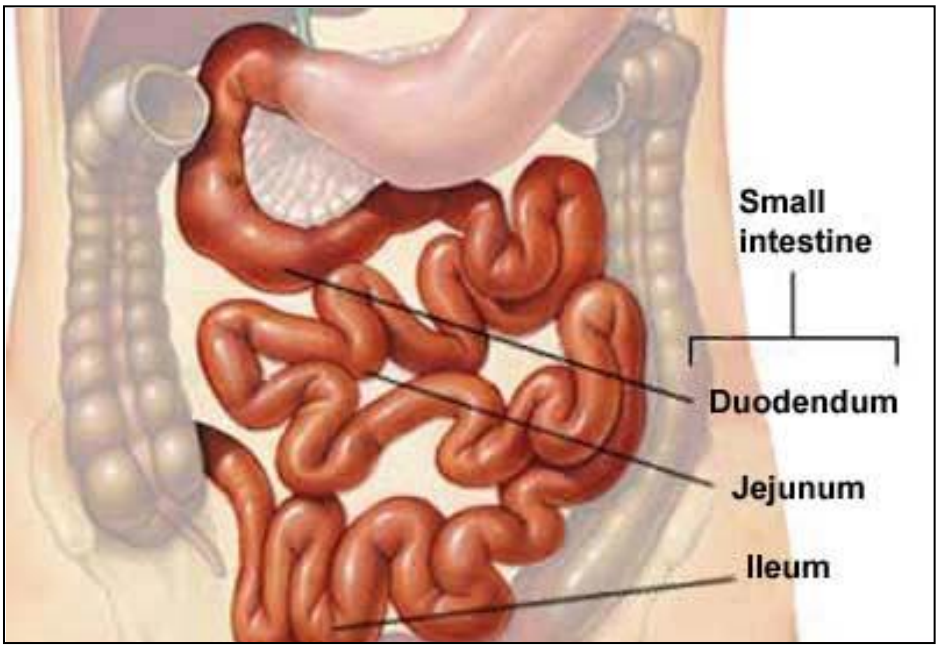

Figure 1.2. The three segments in the small intestine. [Source: Mayo Foundation]

http://www.mayoclinic.com/health/medical/IM00140

The small intestine tube is composed of several layers: the peritoneum or serosal surface, smooth muscle, Nerve plexi, the submucosa and the mucosa (figure 1.3). The serosa is composed of veins, nerves and arteries which link the intestine to other organs. The outer smooth muscle layer has longitudinal fibers while the inner layer has circular fibers. These muscles carry peristalsis by contracting and relaxing and as such they are responsible for the mechanical mixing and the transport of the chyme. The myenteric plexus and the submucosal plexus make up the rich and complex nervous system of the GI tract. See figure 1.4 for a photograph of a small intestine taken during surgery; note the complex and dense blood network.

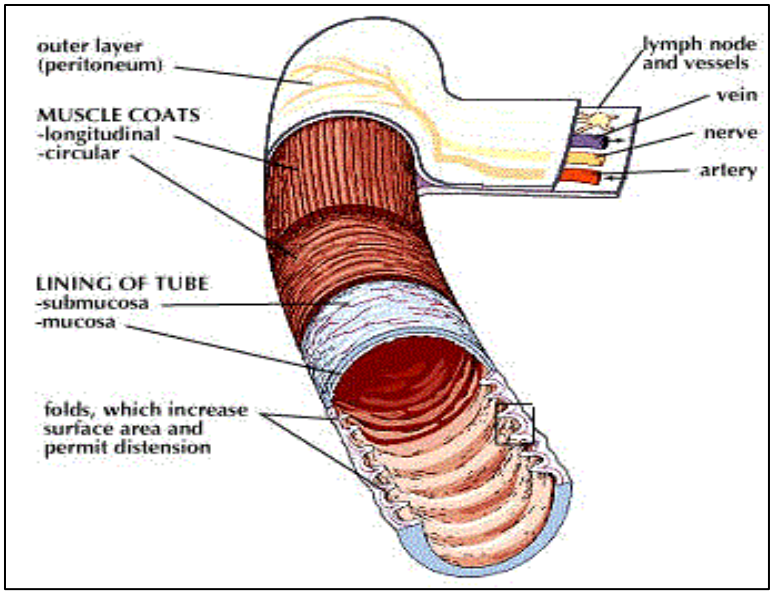

Figure 1.3 Structure of the digestive tube. [Modified from Encyclopedia Britannica]

http://kids.britannica.com/comptons/art-53188

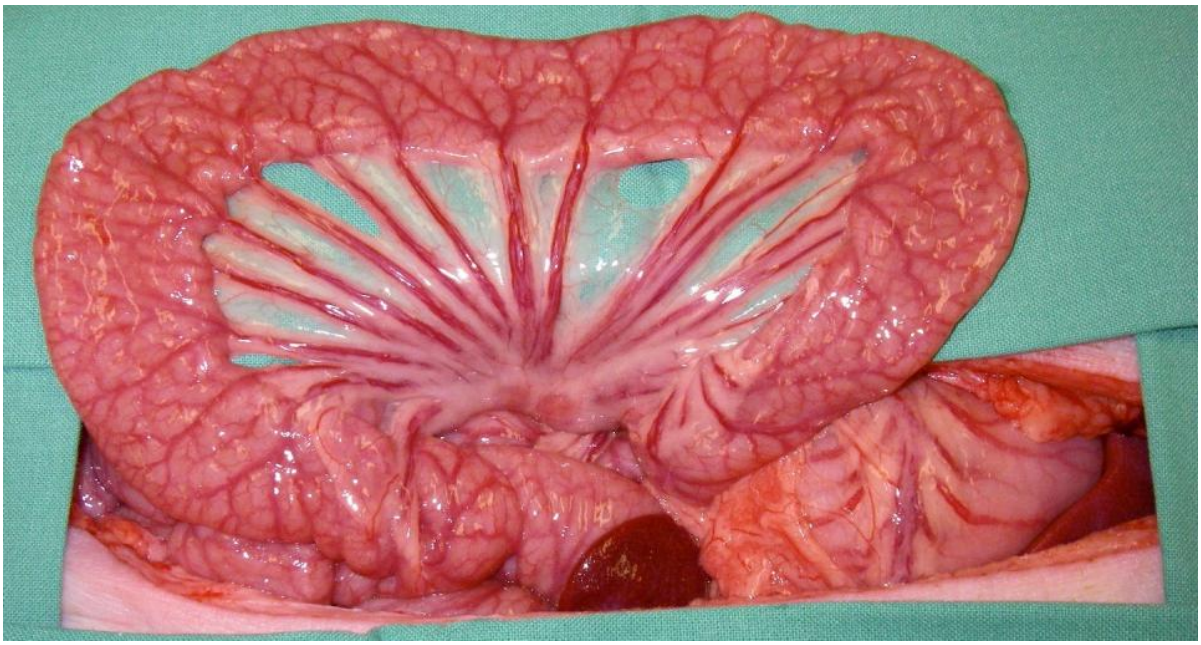

Figure 1.4 Photograph of segment from a pig's small intestine. Complex and dense blood network visible at serosal surface. [Source: Auckland Bioengineering Institute]

http://sites.google.com/site/gimappingsuite/research-projects

1.2 Interstitial Cells of Cajal

The electrically active cells in the intestine nervous system transmit electrical impulses continuously. This electrical activity has been observed for many years through extracellular recordings (Serosal Electrode Recordings: SERs). Recent findings suggest that this continuous electrical activity, referred to as the slow wave, is originated by Interstitial Cells of Cajal (ICC): "ICC in the myenteric region play a pacemaker role in gastrointestinal motility by giving origin to continuous electrical activity" (Farrugia 2008).

ICC are found throughout the intestine. These neuron-like cells form extensive networks through gap junctions. Their filaments spread across the thin gastric wall; facilitating extracellular recording of electrical activity (figure 1.5 and 1.6). Three types of ICC have been identified by electron microscopy; structural differences are thought to reflect cell specialization. (Farrugia 2008). While some ICC specialize in generation and propagation of slow waves, others participate in neurotransmission (Farrugia 2008).

The slow wave is generated at a pacemaker ICC cell and spreads through other ICC across the intestine (figure 1.7) eventually reaching the intestinal smooth muscle. Previous research links the slow wave to muscle contraction (Lammers 2001). Thus, ICC have gained a lot of interest as pacemakers for the slow wave and key players in muscle contraction. In fact, recent research shows that "abnormalities in ICC numbers are associated with several gastrointestinal motility disorders" (Farrugia 2008). As such, "ICC are now recognized as another cell type that are required for the normal functioning of the gastrointestinal tract" (Farrugia 2008).

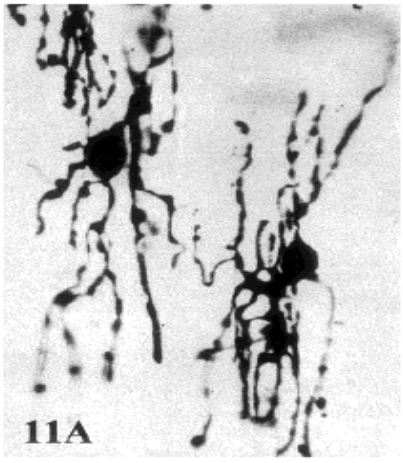

Figure 1.5 Micrograph. Golgi Staining Method. Guinea pig ICC (Taxi 1952). Note cell filaments. Other staining techniques yield different results [Source: Thuneberg 1999].

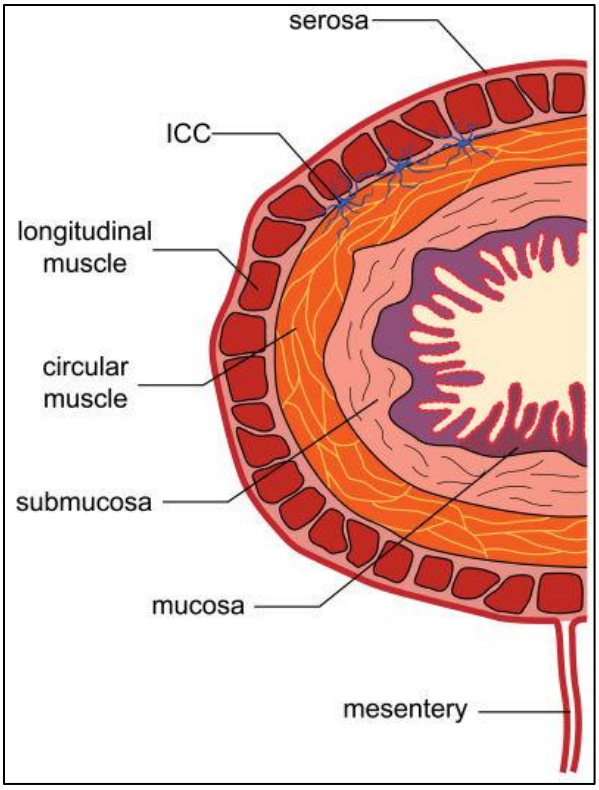

Figure 1.6 Cross section of GI wall. Note that in reality ICC filaments spread across the thin intestinal wall. For a well distended lumen, the small bowel wall is only 1-2mm thick. (Macari 2001). [Source: GIST Support Int.]

http://www.gistsupport.org/for-new-gist-patients/understanding-your-pathology-report-for-gist/diagnosing-gist.php

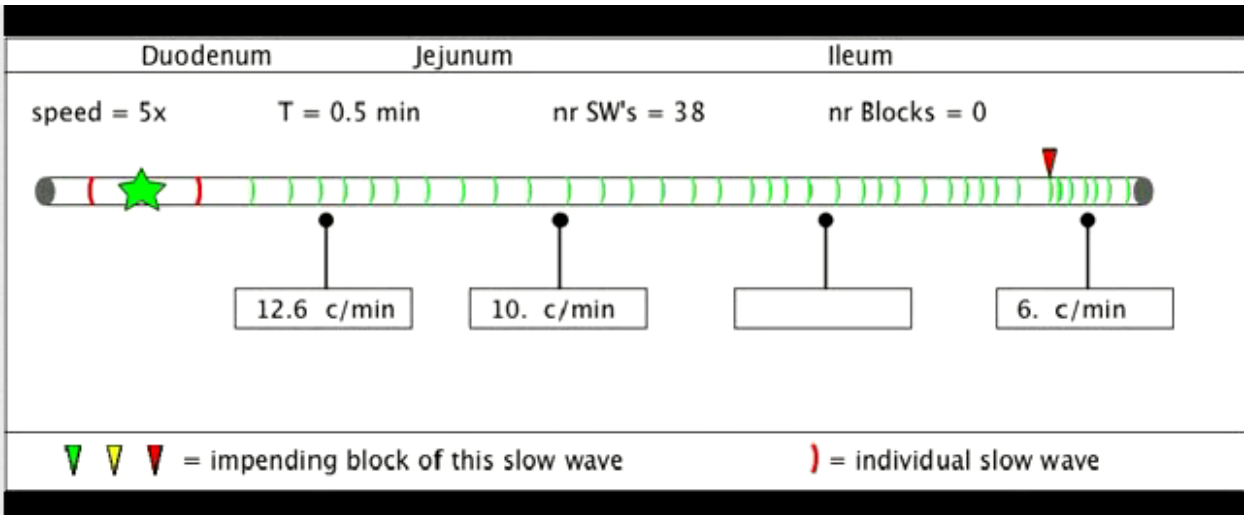

Figure 1.7 Diagram of normal slow wave propagation. Wavefronts are emphasized. Activity generated at pacemaker ICC (green star) and spreads in aboral direction (duodenum to ileum) [From Lammers 2007].

http://www.youtube.com/watch?v=PH6zkPoEOc4

1.3 Electrical Activity in the Small Intestine

Electrical activity in the small intestine has been reported for many years. The two types of waves observed in this region of the GI tract are referred to as slow waves and spikes. See table 1.1 for a summary of current understanding regarding these two waveforms. Slow waves and spikes are often linked to muscle contraction: "intestinal motility is initiated by slow waves and by action potentials (spikes) that may or may not occur in the wake of the slow wave" (Lammers 2003). It is of interest to investigate and model the temporal relationship between slow waves, spikes and contractions.

Slow Waves

Slow waves in animal duodenum and jejunum have been studied extensively since the 1960s (Bortoff 1966, Szurszewski 1968, Lammers 1997-2001-2003-2005-2008,). In a healthy intestine, the slow wave is continuous and periodic with a frequency close to 12-15 cycles per minute (cpm) in humans; characteristics depend on the species. Figure 1.8 provides an example of an extracellular recording showing slow wave spread. The extracellular recording is the raw signal and important information such as the wave's spatial propagation can be derived from it. Falling-Edge Variable Threshold (FEVT) is a validated automated method to detect activation times (ATs) of slow waves (Erickson 2009). ATs are then synchronized with electrode placement information in order to generate spatial propagation maps (See figure 1.9). Several studies have focused on the spatial mapping of slow wave propagation in the small intestine (Lammers 1997-2005-2008-2008) and in the stomach (Erickson 2010).Extensive understanding regarding slow wave propagation patterns has been attained in the recent years, however, slow wave origin mechanisms are still debated and several hypotheses have been proposed (Farrugia 2008).

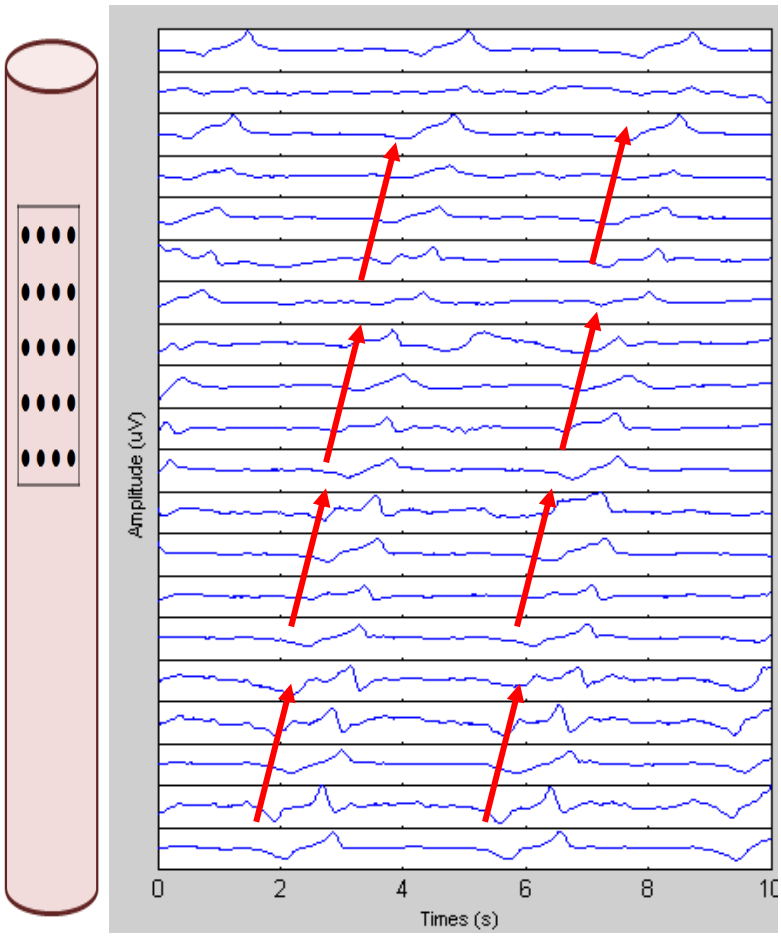

Figure 1.8 Slow wave extracellular electrical activity. Pig SER (Serosal Electrode Recording). Diagram on the left suggests electrode placement on an intestinal segment.

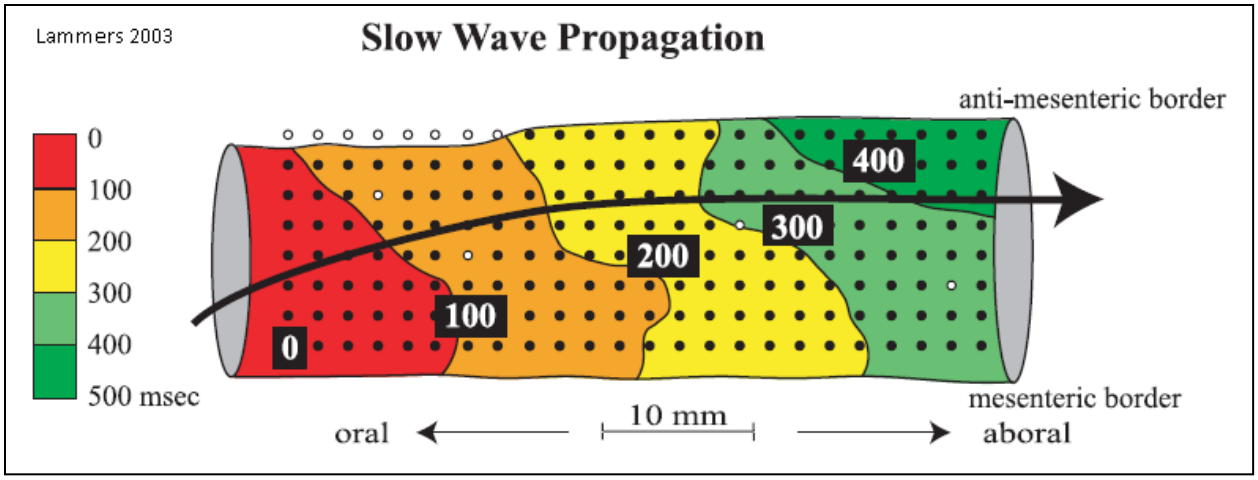

Figure 1.9 Example of spatial propagation map of a slow wave. Different colors indicate time delay in aboral direction [Source: Lammers 2003]

Spike Bursts

Spikes are fast downward and upward deflections which tend to happen in clusters (figure 1.10 and 1.11). In contrast to slow waves, spike activity remains largely unexplored; little literature investigating spikes has been published in contrast to the one addressing slow waves. Spike origin and propagation patterns are still subject of discussion. Unlike slow waves, spikes are not believed to be originated at ICC; they are often associated with smooth muscle cell."The mechanisms responsible for determining the origin of spikes are also not known, but their spatial relationship to slow waves implies a causal relationship" (Lammers 2001). It is believed that slow waves always precede spikes. However, not all slow waves are followed by spikes. Furthermore, previous research on feline tissue (duodenum in vitro tissue) reported that "each spike propagated over small, self-limiting areas before terminating spontaneously" (Lammers 2001). Similar results were observed in a canine model (in vivo) "at every level in the small intestine spikes propagated in all directions before stopping abruptly, thereby activating a circumscribed area termed a patch"(Lammers 2003).

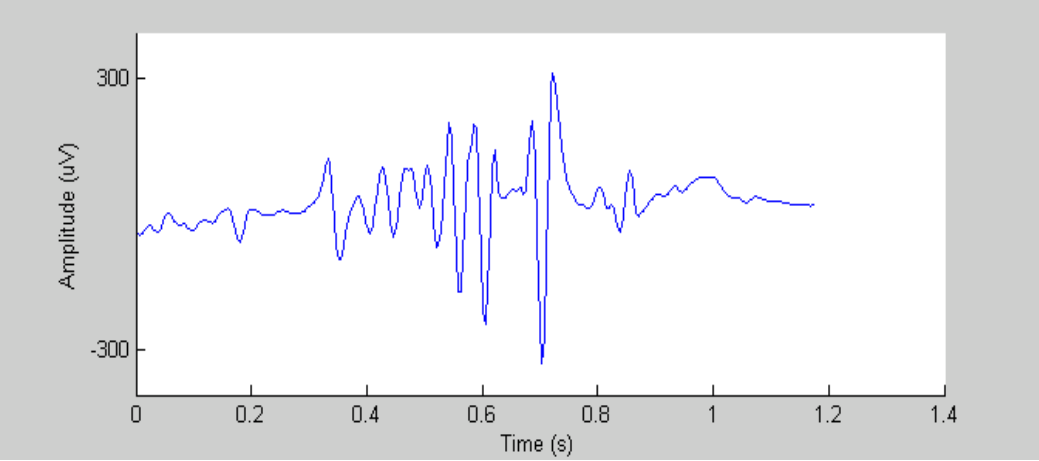

Figure 1.10. Example of a single spike cluster. Pig SERs, one channel. Note time scale and amplitude of waveforms. Very fast deflections reaching large amplitudes.

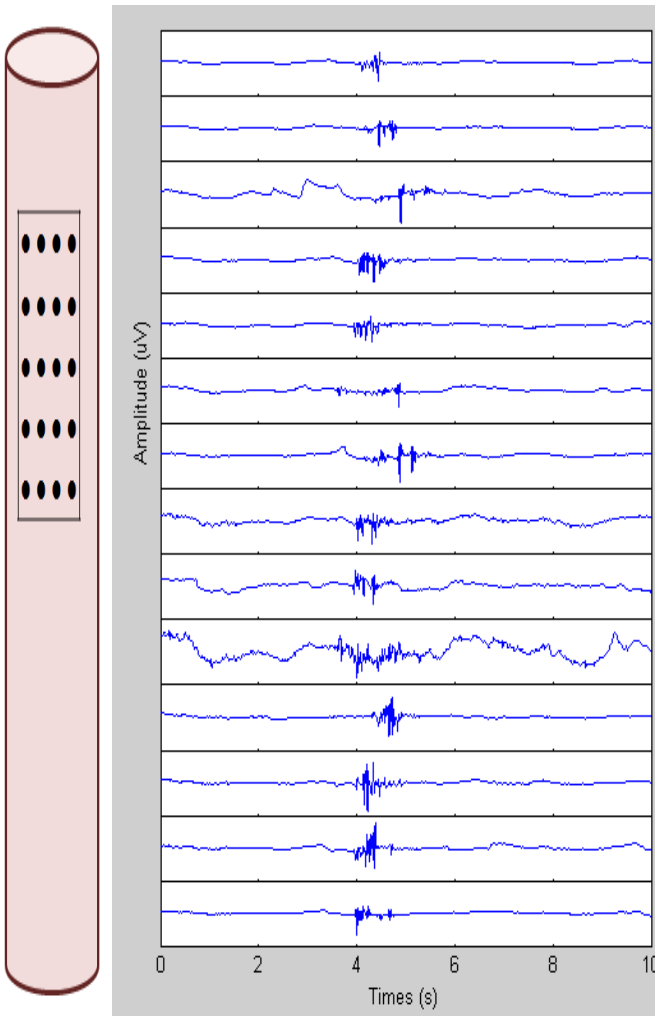

Figure 1.11 Spike extracellular electrical activity. Pig SER. Diagram on the left suggests electrode placement on an intestinal segment

Summary of current understanding of the small intestine electrical activity:

Table 1.1 Summary of small intestine electrical activity

Two waveforms observed:	**Slow wave**	**Spikes**
Activity	Continuous, periodic	Irregular
Frequency	Slow 10-12cpm	Fast
Observed in cell tissue	ICC	Smooth muscle
Origin mechanism	Not fully understood	Not fully understood
Spatial propagation (experiments on feline and canine models)	Uniform Longitudinal Typically aborally, also orally Peripheral pacemakers (Lammers 2005)	Small areas called "patches" End abruptly Observed propagation in all directions (Lammers 2001, 2003)
Automated Detection Methods (non-extensive). See section 1.10 for more details.	Erickson 2009	Summers 1982 Groh 1984 Lammers 2008

1.4 Electro-Mechanical Coupling

The relation between small intestine electrical activity and muscle contraction has been studied for many years. Lammers has observed results (Lammers 2001) that seem to confirm an early model: "the slow wave is an advancing zone of excited excitability which, when further enhanced by local factors, leads to actions potentials and contractions" (Daniel and Chapman 1963). It suggested that the slow wave depolarizes membrane potentials during its propagation. Whenever a certain depolarization threshold is met, spikes are observed. "Smooth muscle spikes, initiated in response to the slow wave, appear to propagate through the smooth muscle layer and are often the first step in the excitation coupling mechanism leading to contraction" (Lammers 2001).

Figure 1.12 demonstrates the relation between the intracellular electrical activity and the contractile reaction of the muscle (Mintchev 1995). In this diagram the slow wave is observed as a rapid depolarization. When a certain threshold is met, spikes succeed the initial depolarization. Based on this model, a weak contraction occurs when the slow wave is energetic enough to go over a plateau. In turn, a stronger contraction is expected when the slow wave goes over the plateau and is accompanied by spikes. It is important to be aware that there is controversy in the field regarding what spikes represent. While we present spikes as an electrical activity preceding muscular activity, others suggest that spikes are the result of the physical motion. Nevertheless, slow waves and spikes are drastically different waveforms; fact which encourages the study and characterization of both.

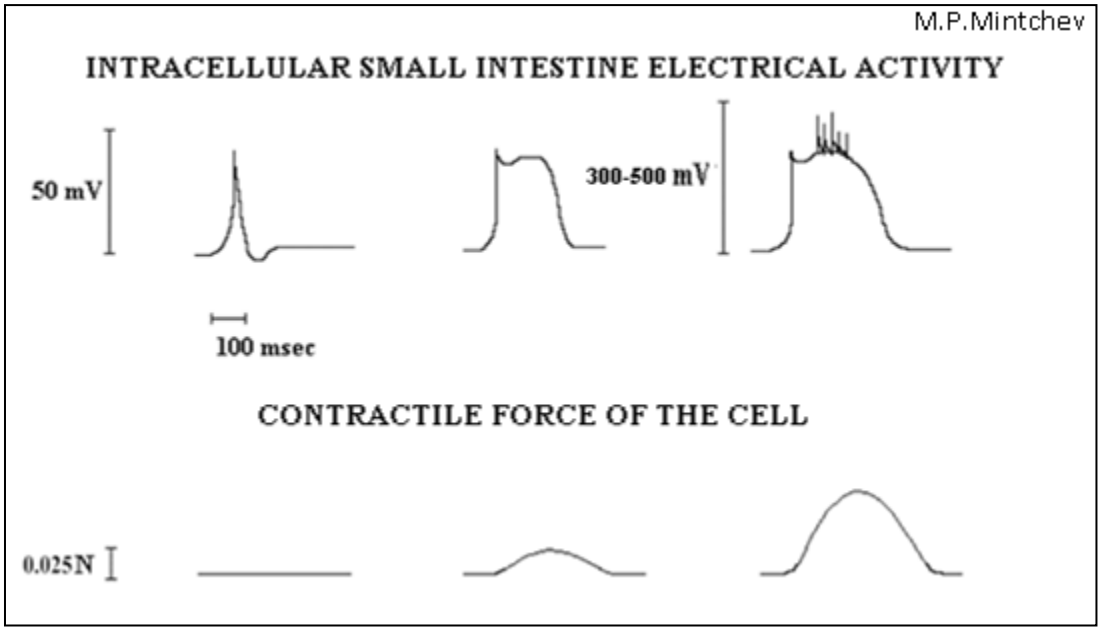

Figure 1.12 Illustration of electro-mechanical coupling in small bowel smooth muscle cell. [Modified from: Mintchev 1995 for gastric electrical activity]

http://www.enel.ucalgary.ca/People/Mintchev/stomach.htm

1.5 Driving Force: Medical Application

As mentioned previously, the slow wave has been investigated to a larger extent than spikes. The benefits of studying spike activity are immense. Greater understanding of spike activity would help clarify the temporal relationship between slow waves, spikes and muscle contraction. More importantly, the medical necessity to conduct further studies is large: in 2009, between 60 and 70 million Americans were affected by digestive diseases such as Crohn's disease, Celiac disease, slow transit constipation, diabetes, etc. (National Institute of Diabetes and Digestive and Kidney Diseases). Knowledge about electrical activity in a healthy small intestine could help understand what is observed in diseased organs. As such, we envision the monitoring of the intestine's electrical activity as a diagnostic tool. This new technique would be non invasive, possibly using cutaneous electrodes, and more informative than current methods like enteroscopy.

1.6 Intestinal Ischemia

This study focuses on small intestine spike activity and investigates the extent to which it is affected by ischemia. Intestinal ischemia is severe condition whereby the intestine suffers diminished blood supply and receives insufficient oxygen and nutrients essential for normal functioning. According to Mayo Clinic experts, intestinal ischemia has many causes. Acute mesenteric ischemia may be due to blood clots, fatty deposits built up on the wall of the artery (atherosclerosis) and low blood pressure (Mayo Clinic 2010). Chronic mesenteric ischemia also results from atherosclerosis. Another type of ischemia takes place when outward blood flow is obstructed; condition known as mesenteric venous thrombosis. Causes for this type of intestinal ischemia are: pancreatitis, abdominal infection, bowel diseases like Crohn's disease or diverticulis,etc. (Mayo Clinic 2010).

1.7 Previous Observations: Induced Ischemia and Electrical Activity

It is reasonable to suggest that ischemia could disrupt electrical activity in the small intestine given that ICC (the pacemakers for slow waves) appear to be very sensitive to damage by hypoxia (Farrugia 2008). Several studies have investigated the effects of induced ischemia on the activities of the small intestine. Ischemia is induced by either occluding an artery or an artery and a vein; each technique possibly yielding different results.

Szurszweski reported the effects of temporary (4 hours) hypoxia on dog jejunum (Szurszweski 1968). He observed that hypoxic perfusion lowered the frequency of slow waves and affected slow wave propagation direction. The usual direction of slow wave propagation is caudad. However, hypoxic areas showed propagation in orad, caudad, or both directions. Szurszweski suggested that whenever the upper jejunum is affected by hypoxia, transitional pacemakers are unmasked in the lower regions. These transitional pacemakers give rise to the unusual propagation of slow wave.

Cabot studied the effects of ischemia induced by arterial occlusion on the electrical and contractile activities of canine small intestine (Cabot 1978). Like Szurszweski, he reported a decrease in slow wave frequency, irregular slow wave rhythm and the cessation of contractile activity upon occlusion. Interestingly, revascularization upon 3 hours of ischemia restored the contractile activity and regular slow wave rhythm. However, revascularization after prolonged periods of ischemia did not restore the normal functions. This suggests that prolonged exposure to ischemia has irreversible effects on pacemaker cells.

Lammers reported that acute (5-10 minutes) local ischemia in a feline small intestine induced major disturbances in the propagation of the slow wave (Lammers 1997). Local areas of inexcitability developed within minutes, often merging to form lines of conduction block. Similarly to Szurszweski, Lammers observed the appearance of subsidiary pacemakers.

Perhaps the most relevant resource for our study is a review paper written by Chou in 1982 "Relationship between Intestinal Blood Flow and Motility". Chou referenced Cabot 1978, Chou 1981, Guisan 1975, Meissner 1976, Kyi 1970 to argue that: "intestinal ischemia and hypoxia can alter electrical contractile activities of the stomach and intestine depending on the duration and severity of the ischemia and hypoxia. Ischemia and hypoxia produced a biphasic change in motility-i.e., an initial transient increase followed by a prolonged paralysis. Thus occlusion of the artery perfusing a gut segment, thrombin-induced mesenteric arterial and venous thrombosis or a 75% reduction in inhaled oxygen produced an immediate but transient increase in spike potentials and contractions lasting for 1-5min. The increased contractions appeared to be mediated by intrinsic nerves since local administration of tetrodotoxin abolished this response. This increase in motility progressively diminished and the gut became quiescent 1-15min after ischemia and hypoxia with the disappearance of spike potentials".

Furthermore, "the duration of ischemia determines whether or not the normal motor activity recovers after revascularization. When the circulation is restored within 1-3hr, the slow waves, spike potentials and spontaneous contractions returned to normal within 1-13min following revascularization. When completed ischemia persisted for more than 4 hr, revascularization did not restore the spontaneous contractions and spike potentials" (Chou 1982).

These studies suggest that ischemia has profound effects on the electrophysiology of the small intestine. Ischemia disrupts slow wave origin and propagation. Moreover, it produces an immediate increase in spike activity after which spike activity diminished progressively.

1.8 Induced Ischemia on Porcine Model Experiments

Several induced ischemia experiments were performed using a porcine model at the University of Auckland and Vanderbilt University. See Chapter 2, section _ for more details.A porcine model is employed because the GI system and abdominal wall architecture closely resemble that of a human. Note that the majority of previous experiments, such as those conducted by W.J.E.P Lammers, were conducted on canine or felines models. We were provided with the data along with the surgical and recording methodology for these experiments. Our initial interest focused on using the data from these experiments to investigate the effects of induced ischemia in small intestine spike activity. However, this type of analysis required us to first develop an automated detection method to process the extensive data sets and detect the spikes. Given the time constrain and in order to generate preliminary results we ran our algorithm on 5 experiments: 3 from Vanderbilt and 2 from Auckland

1.9 Need for Automated Detection Method

Data collected from induced ischemia experiments is extensive; particularly data generated with high resolution electrodes. For example, a 10-minute high resolution SER would produce 42 hours of data for analysis:

$$257\ channels\ \times 587\ \frac{seconds}{channel} \times \frac{1}{60}\frac{minute}{seconds} \times \frac{1}{60}\frac{hour}{minutes} = \ 41.9\ \ hours$$

High resolution experiments are desirable because they allow the generation of detailed spatial propagation maps. With these detailed maps it is possible to analyze extensively the patterns of spike propagation. Nevertheless, visual-manual techniques for marking spikes in extensive data sets is time consuming and burdensome. An automated method detection method could process a data set as such in a few minutes.

Furthermore, the complexity of gastroelectrical signals may give rise to disagreement about the legitimacy of a spike cluster. As mentioned above, spike clusters consist of fast upward/downward deflections easily distinguished from slow waves. However, small intestine SERs present signal contamination which makes spike clusters less obvious and gives rise to discrepancies amongst human markers. See Chapter 2, section _ for more details. Signal contaminants include respiration, cardiac frequency, etc. Hence, an automated spike detection method will not only reduce processing time, but it will mark clusters in a consistent and reproducible manner.

Initial Considerations for Automated Spike Detection Method

A satisfactory algorithm should specific, sensitive, and robust. The algorithm needs to be sensitive in order detect the majority of spikes in a data set. After all, we seek to measure possible changes on spike rates when ischemia is present. Moreover, the algorithm must be specific to only detect spike clusters. In other words, the method should distinguish amongst spikes, slow waves and signal contamination. Finally, the algorithm should be robust and not oversensitive to detection parameters.

1.10 Previous Spike Detection Methods

SUMMERS 1982

Summers reported a software to detect spike bursts (Summers 1982) which consisted of data digitizing, digital filtering and burst detection based on user-defined parameters. Seven channels of myoelectrical data were recorded with sampling frequency <50Hz. Digital filtering involved a second-order infinite impulse response filter. Data was bandpass filterered with cutoff frequencies 10 and 30 Hz. Burst detection was based on a peak detecting algorithm (Yakovle 1977) whereby discrete sample values are used to determine the beginning and end of a spike burst. The algorithm computes the ratio "localized signal intensity"/ "background intensity" by using average power (P). The localized signal is approximated by a constant length sliding window. The background signal is computed by the summation of all data samples preceding a spike burst, known as a "growing window". As explained by Summers:

$$\frac{P_{A_t}}{P_{B_t}} = \frac{\frac{1}{\tau}\sum_{t \in A_t} {X_t}^2}{\frac{1}{t - t^* + 1}\sum_{t \in B_t} {X_t}^2}$$

A_t is the constant length of a sliding window τ samples long
B_t is the growing window which is $t - t^* + 1$ samples long
t is the current sample being processed
X_t is the value of the data sample
τ is the legnth of the "sliding window" in samples
t^* is the sample number at which the growing window was last reset

The ratio $\frac{P_{A_t}}{P_{B_t}}$ has a user-defined threshold which determines the beginning or end of spike burst.

In contrast to high resolution experiments with 257 channels and 512 Hz sampling rate, Summers only processed 7 channels of data at 50 Hz sampling rate. His method utilized the rate of change of data as a means of detection and yielded a machine-observer inter-rater k value of 88.16 (k indicates strength of agreement). However, Summer's method does not address the possibility of signal contaminants being erroneously marked a spike clusters. Moreover, Summer's background signal or "growing window" is reset every time a signal with sufficiently high power is detected. This suggests that the method would be very sensitive to high amplitude artifacts. In contrast, our algorithm obtains the background signal by estimating the noise level for an entire channel's data.

Nevertheless, Summers discusses two important issues: the spike algorithm should avoid detecting isolated spikes and should provide the user the ability to fine-tune detection parameters. Isolated spikes, which do not show a propagation pattern, are not likely to reflect legitimate electrical activity. Allowing the user to fine-tune detection parameters will contribute towards the algorithm's robustness. Given the complexity of small intestine SERs, fine-tuning detection parameters for a given data set could yield slightly better results.

GROH 1984

Groh's method consisted of: bandpass filtering, slope averaging, threshold detection and statistical analysis. Initial stage used second-order Butterworth filter with bandpass frequency 10-20 Hz; attenuating the slow wave and other low frequency forms. The slope was averaged for a 0.2 second interval by using a modified moving average technique. Detected waves were separated through statistical analysis based on amplitude on duration. Perfect agreement between automated results and observer was reached for 78-89% of the 2-minute samples.

Groh's method, like Summer's, focused on the rate at which signal changes. A possibly pitfall of this method is that any waveform with similar amplitude and duration to spikes will be erroneously detected. Given the contaminants observed in our data, this method could yield many false positives. Our algorithm classifies waveforms by focusing on more features; for example, the signal's energy and signal to noise ratio. See Chapter 2, section _ for more details.

LAMMERS 2008

Lammers designed an on-line electrogram analysis for processing myoeletric readings from canine duodenum and antrum (Lammers 2008). 24 channels of data were recorded at 200 Hz and 1000 Hz sampling frequency. Signals were initially smoothed with a running average to remove 50 Hz noise. His method consisted of a slow wave/spike discriminator followed by specialized detection modules. Spikes were separated from slow waves by normalization of the signal and high-pass filtering set at 30 Hz. A series of steps were conducted to optimize the signal and reduce the noise. The signal was required to meet a threshold before into the spike detection module. The spike detection module consisted on: signal differentiation, inversion, conversion to absolute values, running median subtraction and finally, peak detection. Lammers argued these series of processing steps as a means to shift noise away.

In contrast to Summers and Groh, Lammers subjected signals to extensive processing. In particular, we question the initial signal smoothing and its effect on spike waveforms. Our algorithm attempts to

preserve spikes fine details by having a moving median filter with large window size and a high frequency filter set well above the expected for spikes. See chapter 2 section _ for more details. In addition, Lammers method is designed to detect single spikes while we are interested in detecting spike clusters. We expect our algorithm to have advantage in processing contaminated signals over the aforementioned methods.

This chapter has addressed several topics concerning the small intestine: intestinal wall structure, ICC, electrical activity, electro-mechanical coupling, ischemia, induced ischemia experiments, need for automated spike detection and previous attempts at automated spike detection. We are ready to move into chapter 2 where we will discuss the details specific to the induced ischemia experiments and fully describe our algorithm.

Chapter 2

Induced Ischemia Experiments: Methods and Data

2.1 Experimental Details

Our collaborators at Vanderbilt University and The University of Auckland conducted several induced ischemia experiments between 2008 and 2011. Both laboratories used a porcine model given the resemblance of the GI system and abdominal wall architecture to those of a human (Erickson 2009).Typically the animals were fasted during the 24 hours previous to the surgical procedures. All animal surgeries were carried out under strict Institutional Animal Care and Use Committee guidelines (IACUC).

Serosal Electrode Recordings (SERs)

SERs were made in vivo. The pig was anesthetized and place in supine position. A midline supra-umbilical incision was made. Once access to peritoneal cavity was gained, a segment of the small intestine was identified. The intestinal segment was placed on wet cotton gauze and an electrode array was attached to its serosal surface. Figure 2.1, illustrates this process with the use of a rigid electrode.

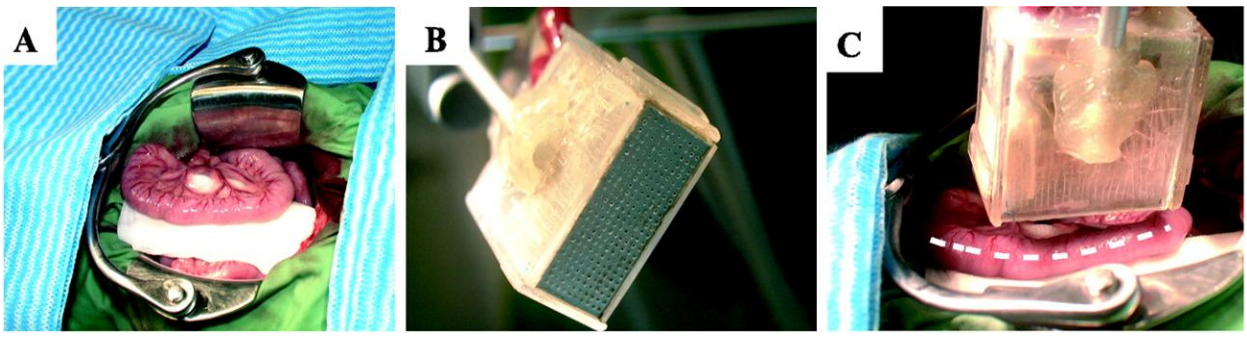

Figure 2.1. Example of a serosal electrode recording using a rigid electrode. A. Exposed segment of the small intestine. B. Rigid electrode. C. Electrode in contact with serosal surface. [Source: Lammers 2003]

Similarly to the experiment in figure 2.1, the Vanderbilt experiments utilized rigid electrodes. More specifically, 49 Ag/AgCl electrodes in various arrangements. Figure 2.2 illustrates the dimensions of an electrode and its placement on an intestinal segment. While this electrode was not used in our experiments, it is important to realize the relative size of this apparatus. The example shown in figure 2.2 has an area of 1.656 cm^2 and a 10 x 24 electrode array resulting in 240 channels of data.

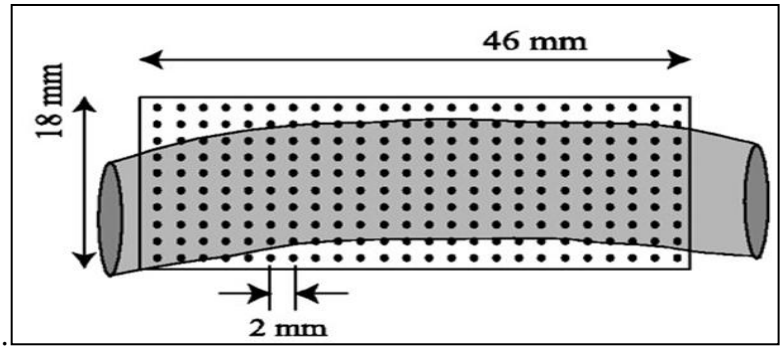

Figure 2.2. Sample diagram to illustrate an electrode's dimensions and placement on intestine. [Modified from: Lammers 2003]

The Auckland experiments relied on customized flexible printed circuit board electrodes (Peng Du 2009). See figure 2.3. These electrodes allowed high resolution mapping as they covered the entire intestinal circumference at a 512 Hz sampling rate and with 249 channels of data. The electrodes were held in place with warm gauze pads. Once electrode setup finished, the intestine was reintroduced into the abdominal cavity to avoid changes in the tissue's temperature and humidity.

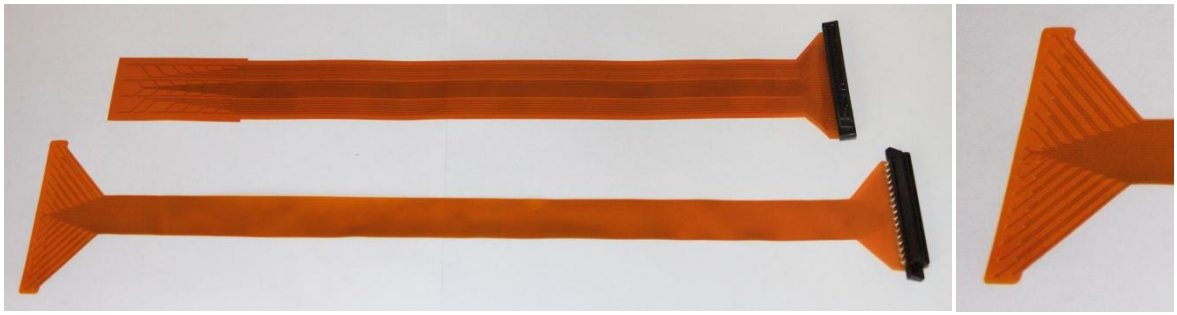

Figure 2.3. Flexible printed circuit board electrodes used by the researchers at University of Auckland. On the right, zoom showing actual electrode which folds 360º around the intestinal serosal surface. [Source: Auckland Bioengineering Institute]

Baseline recordings were taken for all the experiments lasting approximately 30 minutes for Vanderbilt experiments and 8-15 minutes for Auckland experiments. The baseline recording intends to show the electrical activity of the intestine in a healthy state. However, it is important to acknowledge several experimental factors that could give rise to abnormal activity. Firstly, the animals had been fasted for an extended period. Hence, there was little or no food circulating in the animal's intestine. Next, the animals were treated with anesthetics which impact nerve functions. Moreover, the recordings were made following a very invasive surgical procedure, the midline incision. These factors might have an effect on what we observe on the baseline recordings. Thus, the presumed baseline recordings might differ to an extent from the electrical activity in a true healthy intestine.

Induced Ischemia

Following the baseline recordings, ischemia was induced by occluding local arteries near the intestinal loop. Two types of ischemia experiments were conducted: segmental and partial ischemia. For the segmental experiments, full ischemia was induced by simply tying a surgical string around the local

arteries (figure 2.4). Data was collected for the particular ischemic segment. Thereafter, blood flow was restored and ischemia was induced on a different intestinal segment.

For the partial experiments, ischemia was induced progressively by using inflatable occlusion cuffs (figure 2.5). The intervals at which data was recorded were 50%, 75%, 90% and 100% ischemia.

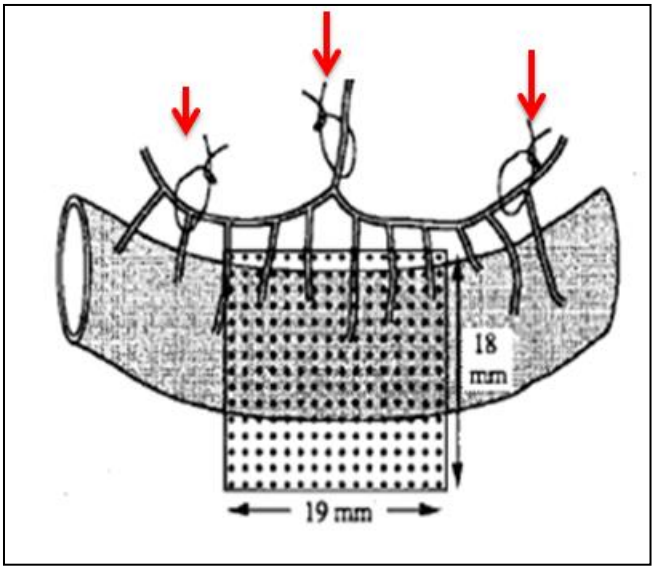

Figure 2.4. Inducing local full ischemia by tying a string around 3 arteries.[Source:Lammers 1997].

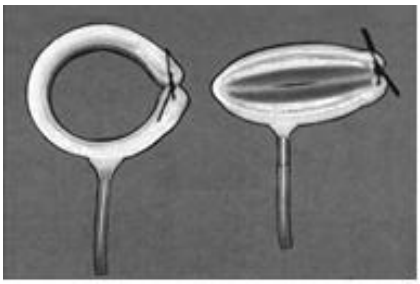

Figure 2.5. Occlusion cuff or vascular occluder. On the left, cuff allows unobstructed blood flow. On the right, inflated cuff obstructs blood flow and induces ischemia. [Modified from: Kent Scientific]

https://www.kentscientific.com/products/

2.2 Data Collected

The experimental details relevant for our analysis are: recording time, sampling rate, number of channels, and type of experiment: segmental or partial. The amount of data collected varies from experiment to experiment. See Table 2.1 for details. These differences arise primarily from the different recording technologies at the each laboratory and differences in recording time. Recording length ranged from 8 to 69 minutes.

Table 2.1. Summary of data collected from induced ischemia experiments and relevant information for signal processing

	Date	**Experiment type: Induced ischemia**	**Number of Channels**	**Sampling frequency (Hz)**	**Rec. Time (s)**	**Rec. Time (min)**
	Auckland					
	2011					
1	06.01.11	Pig 34 exp 10 baseline + full ischemia Pig 35 exp 12 baseline + segmental Pig 35 exp 13 baseline + segmental	257	512	2009 1828 1980	34 31 33
2	05.03.11	Pig 33 exp 9 baseline Pig 33 exp 10 full ischemia	257	512	478 587	8 10
	Vanderbilt					
	2010					
3	01.22.10	Baseline Segmental ischemia	49	256	1972 3781	33 63
	2009					
4	06.09.09	Baseline Segmental	49	256	1585 3820	27 64
5	05.29.09	Baseline Segmental	49	256	1870 3505	32 58
6	05.28.09	Baseline Segmental	49	256	1780 3626	30 60
7	05.22.09	Baseline Segmental	49	256	1801 3992	30 67
8	04.17.09	Partial a. baseline b. 50% ischemia c.75% ischemia d.90% ischemia e.100% ischemia	49	256	 1490 1711 1710 1614 3527	 25 29 29 27 59
9	04.16.09	Partial a. baseline b. 50% ischemia c.75% ischemia d.90% ischemia e.100% ischemia	49	256	 1720 1660 1415 1637 2965	 29 28 24 27 50
10	04.15.09	Partial a. baseline b. 50% ischemia c.75% ischemia d.90% ischemia e.100% ischemia	49	256	 1725 1485 1390 1618 2460	 29 25 23 27 41
11	04.14.09	Partial a. baseline b. 50% ischemia c.75% ischemia d.90% ischemia e.100% ischemia	49	256	1914 1873 1799 1801 3547	32 31 30 30 59
	2008	Additional experiments.				

2.3 Need for Automated Spike Detection Method

Large Data Sets

As we mentioned in chapter 1 section _, these data sets are extensive. For example, a segment of an Auckland experiment which recorded during 9.8 minutes results in 70 million samples and 42 hours of data to analyze. This is because these experiments were performed with high resolution electrodes.

$$257\ channels\ \times 587\ \frac{seconds}{channel} \times 512 \frac{samples}{second} =\ 77.2\ \times 10^6\ \ samples$$

$$257\ channels\ \times 587\ \frac{seconds}{channel} \times \frac{1}{60} \frac{minute}{seconds} \times \frac{1}{60} \frac{hour}{minutes} =\ 41.9\ \ hours$$

A segment of a Vanderbilt experiment which recorded for 30 minutes results in 23 million samples and 24.5 hours of data to analyze. The Vanderbilt experiments used lower resolution electrodes in comparison to the Auckland experiments.

$$49\ channels\ \times 1800\ \frac{seconds}{channel} \times 256 \frac{samples}{second} =\ 22.5\ \times 10^6\ \ samples$$

$$49\ channels\ \times 1800\ \frac{seconds}{channel} \times \frac{1}{60} \frac{minute}{seconds} \times \frac{1}{60} \frac{hour}{minutes} =\ 24.5\ \ hours$$

If the experiment mentioned above was a partial ischemia experiment it would have had 5 segments: baseline, 50%, 75%, 90%, and 100% ischemia. The result is an overwhelming 122.5 hours of data to analyze.

$$24.5\ \frac{hours}{segment\ of\ experiment} \times (1\ baseline\ segment +\ 4\ partial\ ischemia\ segments) = 122.5\ hours$$

An automated method will greatly reduce analysis time. Visual inspection is time consuming and surveying large data sets such as those mentioned above would be a laborious task for the human observer.

Signal Contamination

In signals like figure 2.6, spikes are easily identified through visual inspection. However, serosal recordings of the small intestine often present signal contamination. Some common contaminants are: cardiac waveform, respiration, artifacts, and baseline wander. The presence of these waveforms makes visual spike classification a complex task. Sometimes it is hard to confirm the presence of a spike due to the superimposed contaminants.

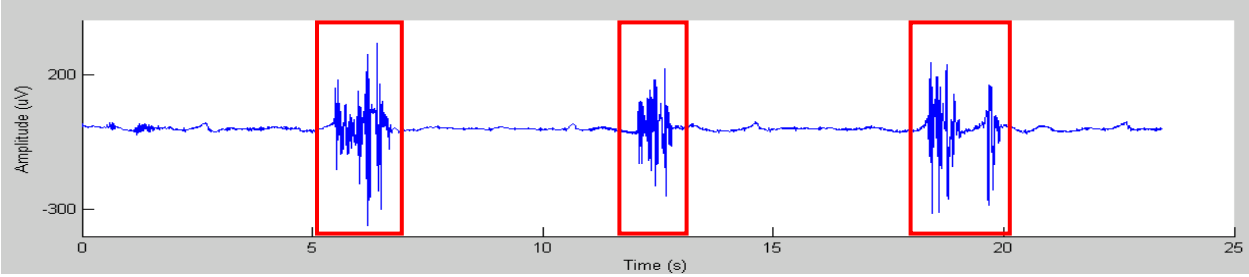

Figure 2.6. Easily recognizable spike clusters. Small data set, little noise, no signal contaminants.

The initial stage of signal processing was focused on becoming familiarized with the data from the small intestine recordings. We visually inspected the recordings and were surprised to observe a wide range of waveforms. The electrical activity observed originates from the subject's physiological activity but is also affected by the experimental conditions. Some factors that could influence the resulting data are: type of electrode, sampling frequency, surface contact between the tissue and the electrodes, electrical activity in other organs of the body like the cardiac waveform, respiration, body movement, etc.

We have observed signal contamination in the recordings from both of our sources: experiments carried in Vanderbilt University and the University of Auckland. In addition to the expected slow waves and spike clusters, it is possible to encounter: cardiac signals, respiration, several types of artifacts and a wandering baseline. The presence of these contaminants makes spike detection more challenging and demands an algorithm which can discriminate effectively amongst waveforms.

The cardiac signal is a small amplitude- high frequency waveform which occurs repetitively throughout a data channel (figure 2.7). If we look closely at figure 2.8, we observe an overlay of the cardiac signal over a larger amplitude-low frequency waveform. This low frequency waveform is respiration and it occurs approximately every 2.5s. In figure 2.9, we can observe a data section contaminated by respiration.

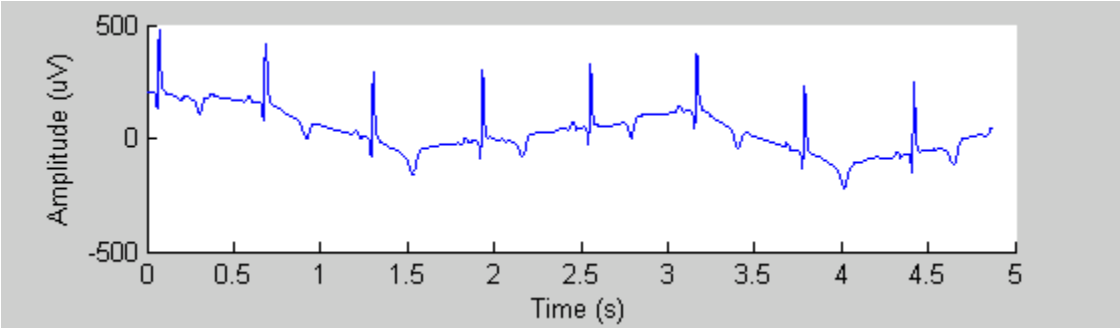

Figure 2.7.Cardiac waveform. Period approximately 0.5-0.6s.

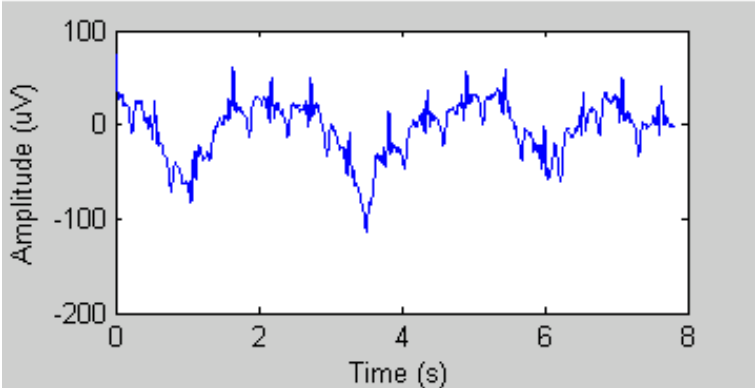

Figure 2.8. Cardiac signal overlay with respiration.

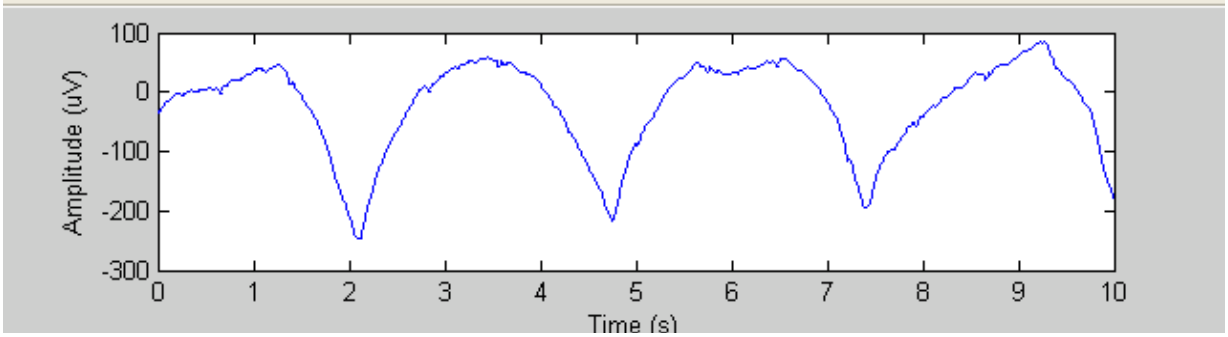

Figure 2.9. Contamination of signal by respiration with period approx. 2.5s.

Artifacts are large amplitude-medium frequency forms which occur once or twice in a data channel (figure 2.10 and 2.11). Typically, their frequency is lower than spike frequency but higher than respiration frequency. There is potential for confusing artifacts with slow waves or spikes. However, artifacts would seem isolated events with no clear spatial propagation unlike slow waves.

Moreover, high frequency artifacts can be distinguished from spikes given their unusually high amplitude. In figure 2.11, the artifact reaches 5,000µV as opposed to the physiologically-expected 400-1000 µV. Artifacts can be further distinguished from spikes because they do not happen in clusters. In artifacts we observe a single "spike-like" upward-downward deflection, however, we do not observe the clustering of deflections as we expect from small intestine spikes.

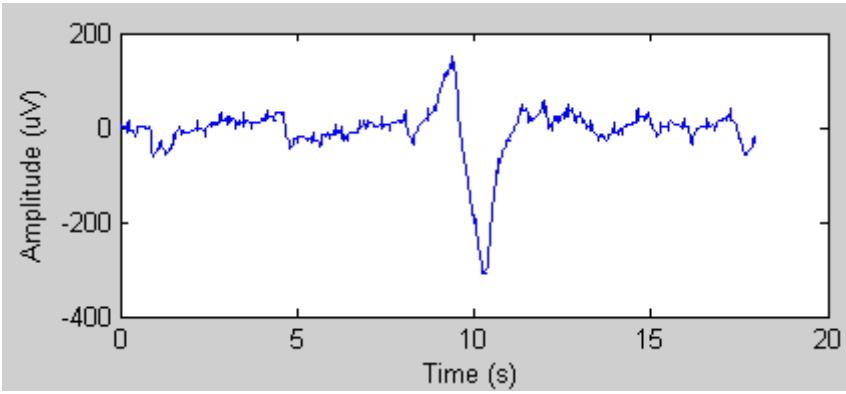

Figure 2.10. Smaller amplitude-low frequency artifact.

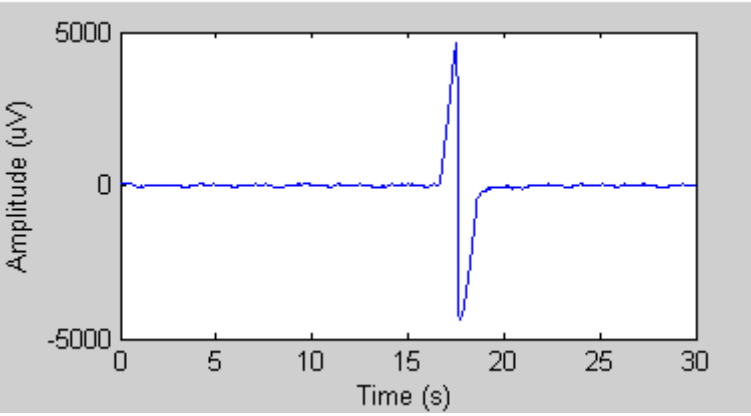

Figure 2.11. Large amplitude artifact.

It is common to observe baseline wander (figure 2.12) and noise (figure 2.13). Baseline wander in raw data can be addressed during the pre-processing filtering stage. However, channels with high levels of noise can pose a challenge for spike detection particularly if the spike clusters do not have high amplitudes.

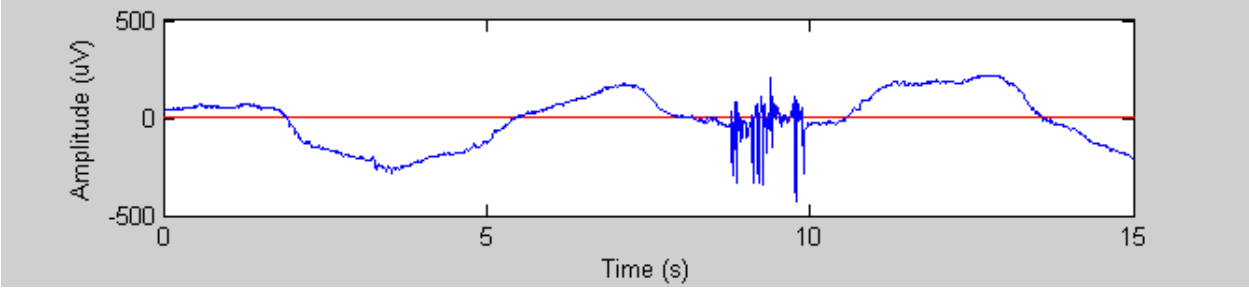

Figure 2.12. Baseline Wander. Red line is a zero potential to emphasize signal baseline wander.

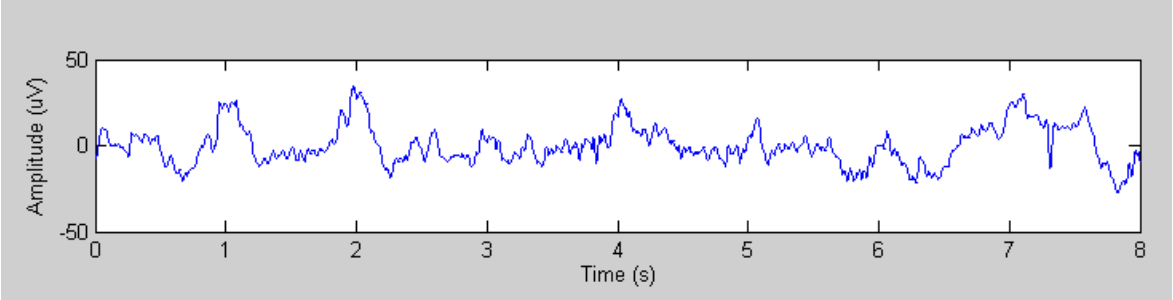

Figure 2.13. High levels of noise in channel.

Oftentimes, channels have very low average amplitudes of 0-5μV (figure) which could be due to poor contact between an electrode and the intestinal tissue. These channels are considered defective and ignored during spike detection.

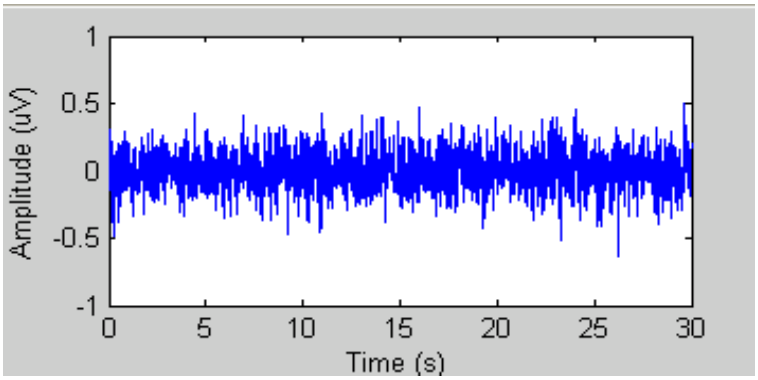

Figure 2.14. Defective channel

2.4 Examples: Increased Difficulty in Visual Spike Classification

The following are examples showing how contaminants and noise increase the difficulty of visually recognizing spike clusters.

A.

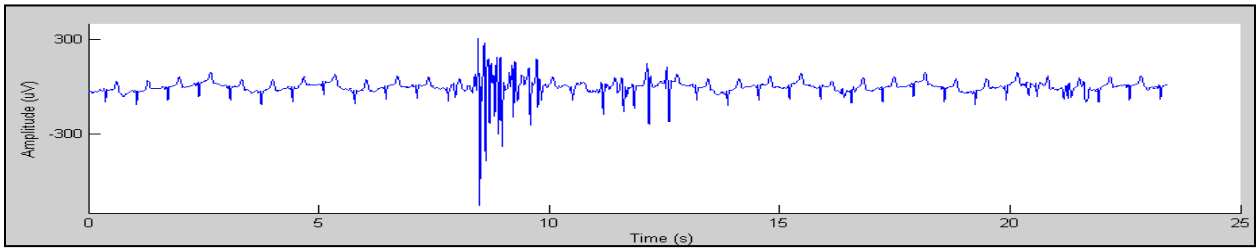

B.

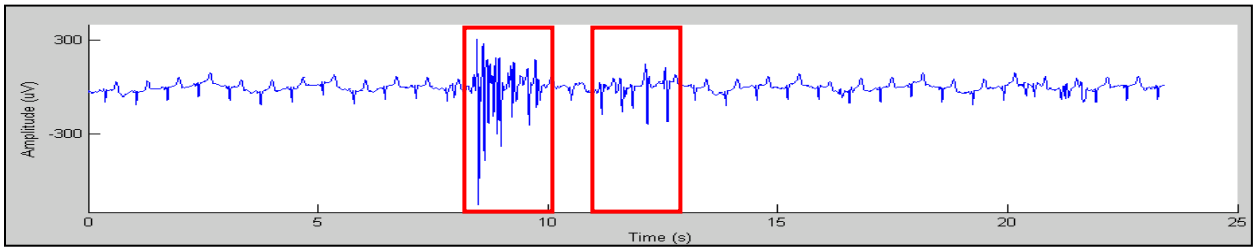

Figure 2.15. A: signal contaminated with cardiac waveform. B: two possible spike clusters found. Second cluster is questionable.

A.

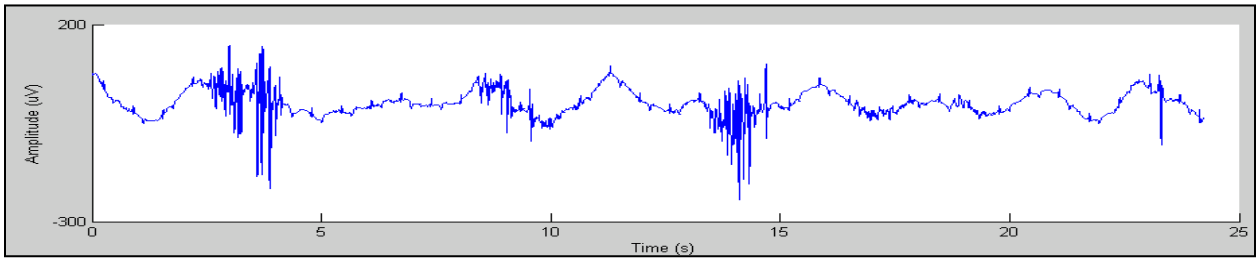

B.

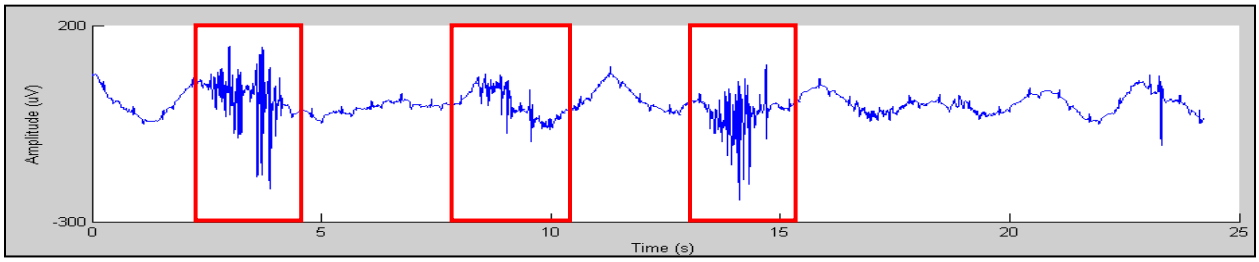

Figure 2.16. A: signal contaminated by baseline wonder and noise. B: three possible spike clusters. Middle cluster is questionable.

A.

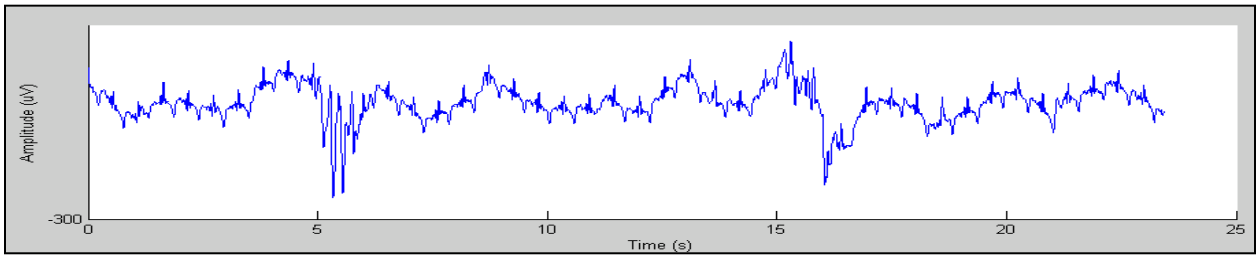

B.

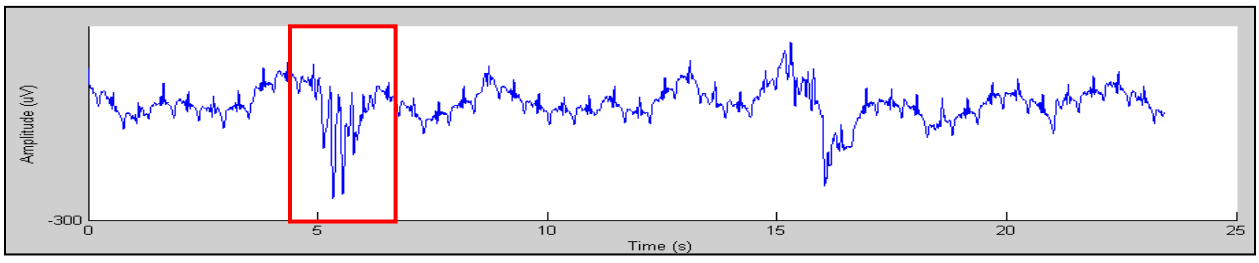

Figure 2.17. A: signal contaminated by heart waveform and respiration. B: Possible spike.

In chapter 2 we have discussed the experimental details of the induced ischemia experiments and become familiar with the obtained data. We have stated why it is necessary to have an automated method and what factors make spike detection challenging. We are ready to proceed into a detailed description of our algorithm.

Chapter 3

Spike Detection Algorithm Design

3.1 Analytical Method: Binary Classification

The algorithm was designed to classify waveforms into two categories: either a spike or not a spike. This procedure is called a binary classification and aligns perfectly with our interests. We do not need the algorithm to separate the other waveforms into individual classes like cardiac, respiration, artifact, etc. Hence, we created a fictitious class which comprises all the waveforms which are not spikes.
There are four possible outcomes for a binary classification (see table 2.2). A true positive (TP): if the sample is a spike and the method detected it. A false negative (FN): if the sample is a spike and the method missed it. A false positive (FP): if the sample is not a spike but the method detected it. A true negative (TN): if the sample is not a spike and the method did not detect it. The outcomes are summarized in the chart below.

Table 3.1. Possible Test Outcomes .

Test Outcome	True Identity of Sample: SPIKE	True Identity of Sample: NOT A SPIKE
POSITIVE	true positive	false positive
NEGATIVE	false negative	true negative

Thus, the outcomes that are sources of error are the FPs and FNs. We must keep in mind these sources of errors as we validate the algorithm and evaluate its performance.

3.2 Measures of Performance

Traditionally the two indicators of the performance of a test are sensitivity (SN) and positive prediction value (PPV) (or "specificity"). Sensitivity is referred to as the true positive rate and is defined as:

$$SN = \frac{TP}{TP + \boldsymbol{FN}}$$

A low number of TP or large number of FN will result in low sensitivity. In order to have perfect sensitivity the test must detect ALL the existent spikes. Perfect sensitivity is unlikely; however, we could achieve high sensitivity by detecting a large portion of the existing spikes.

The positive prediction value is referred to as the precision rate and is defined as:

$$PPV = \frac{TP}{TP + \boldsymbol{FP}}$$

A low number of TP or a large number of FP will result in low PPV or specificity. In order to have perfect PPV the test must detect ONLY spikes and no other waveforms. If other waveforms are detected they will become FPs and decrease PPV. Like we mentioned previously, it is unlikely to have perfect specificity. However, a high PPV could be achieved by having a low number of FP.

AROC: Area under the Receiving Operating Curve

For our analysis we employed a third performance metric termed AROC (Area under the Receiving Operating Curve) (Erickson 2009). AROC is defined as:

$$AROC = SN \times PPV$$

AROC is a measure of the algorithm's performance for a given set of parameters. Three parameters we are interested in analyzing are k, DT and windowL. A perfect AROC will have a value of 1. It is important to point out that acceptable values of SN and SPC might result in a smaller AROC given the multiplication operation. For example, 95% SN and 95% SPC will result in AROC = 0.9025. AROC will help us to understand how the algorithm performance is changing as parameters change and will also help us predict the best parameter values to optimize performance. For these we will generate plot such as the one showed in figure 1.18.

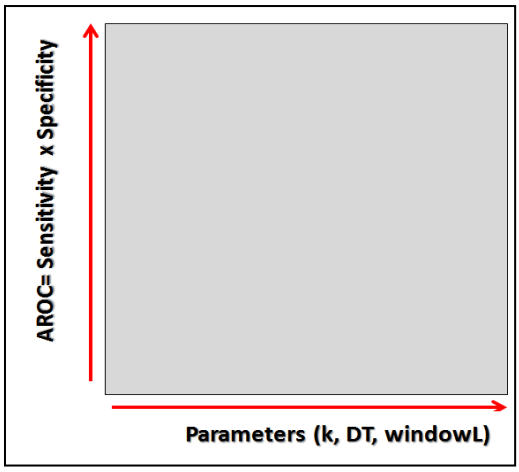

Figure 3.1. Plot to be constructed: AROC vs. detection parameter. Measuring algorithm performance.

3.3 "Gold" Standard Set: Compare Manual vs. Automated marks

In order to measure the algorithm performance we generated 5 sets of standard marks; each with 40 channels of data and 60 seconds long. The sets were selected from different experiments. Moreover, each set was analyzed separately by 3 observers. The observers agreed upon the general criteria to mark a spike. Then, each observer marked the spikes he observed in each data set. Some spike clusters are easier to identify than others which gives rises to disagreement between the 3 sets of manual marks. Also, it is difficult to determine precisely the start and end point of a spike cluster given the very small amplitudes present at the edges of a spike cluster and personal judgment. Thus, manual marks differ in start and end points by fractions of a second.

The marks of the 3 observers were pooled together; only those clusters marked by the 3 observers (regardless of small timing differences) were determined to be the standard marks. This set of standard marks was used for the algorithm validation discussed in chapter 4. The automated marks were compared to the standards and performance metrics were calculated.

3.4 The Spike Burst Detection Algorithm

The algorithm consists of four steps executed in the following manner: preprocessing, candidate detection, machine classification, and additional discrimination. Figure 3.1 illustrates the algorithm flow and provides more details regarding each step. The next section provides a thorough explanation for every step in the algorithm accompanied by illustrations of each method.

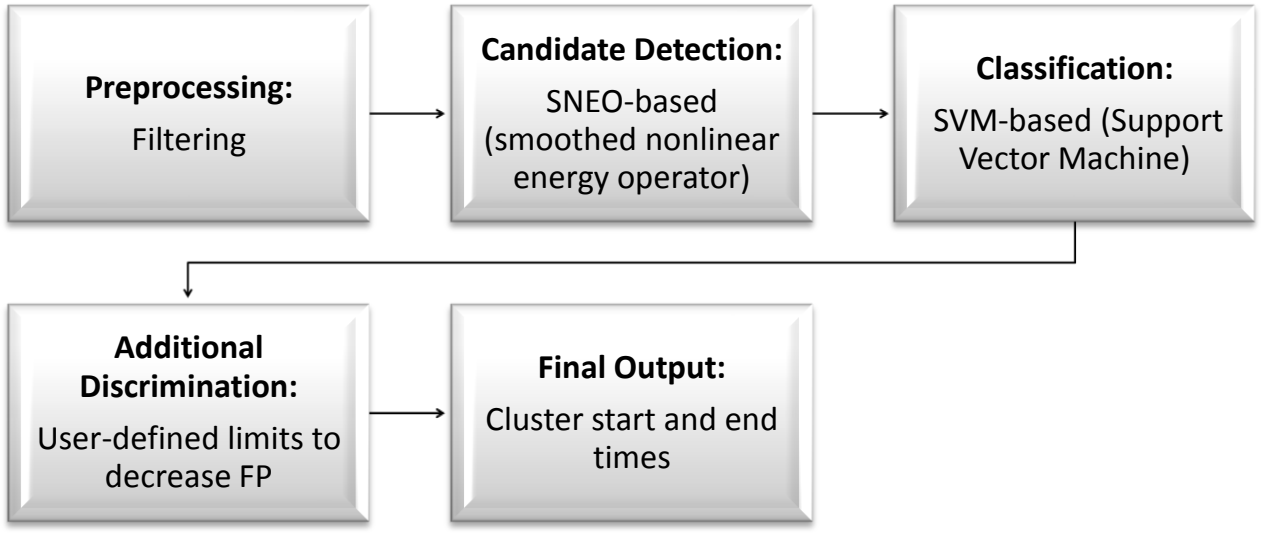

Figure 3.2. Flow chart of spike detection algorithm. See text for description of each stage.

3.5 Preprocessing

In chapter 2, section 2.3.2; we discussed the severity of signal contamination in SERs of the small intestine. It is possible to target contaminants by digitally filtering the signal. Filtering is a common initial step in many signal processing applications. We chose to filter low frequencies using a moving median (MM) filter and high frequencies using a Savitzky-Golay (SG) filter. By using the MM filter we aimed to reduce the wandering baseline and by using the SG filter we aimed to eliminate high frequency noise arising from electrical equipments. Figure 3.3 and 3.4 illustrate the MM filter: the raw signal is depicted in blue and the filtered signal in red. The removal of wandering baseline is evident. Figure 3.5 illustrates SG's ability to remove high frequency noise (likely originated in electrical equipment). Note the time scale difference between figures 3.3, 3.4 and 3.5. In order to observe SG filter effects had to zoom into a 3 second window. MM effects are observed in the larger 15 second data segment.

The specific details are described here. Raw data in the.bdf format is loaded into GEMS (v1.6) and filtered before being export into a .mat file. We used the MM filter with windows size 0.5 or 1 and the SG

filter with polynomial 9 and windows size between 0.08 and 0.1. These values were derived from trial and error observations and previous work done by GEMS developers with slow waves.

These filter settings do not affect artifacts or the cardiac waveform. Thus, these contaminants will be carried forward and should be addressed in the later stages of the algorithm. Moreover, the high frequency filter should be set carefully so as to avoid any possible distortion of true spikes. That is, the low pass filter should be set at a frequency much higher than the typical frequency for spikes.

3.5.1 Preprocessing examples

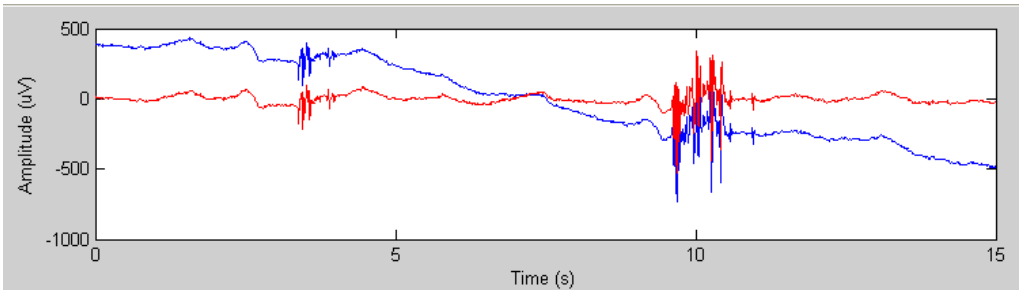

Figure 3.3. Moving median filter. Raw signal is depicted in blue and filtered signal in red. The removal of wandering baseline is evident. Filter executed with window size 1.

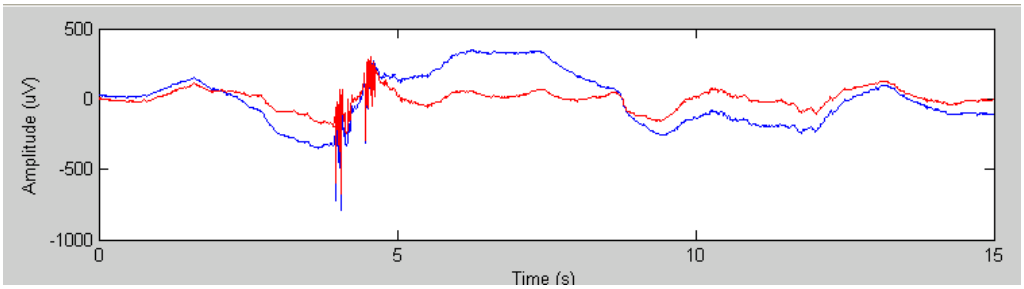

Figure 3.4. Moving median filter . Raw signal is depicted in blue and filtered signal in red. The removal of wandering baseline is evident. Filter executed with window size 1.

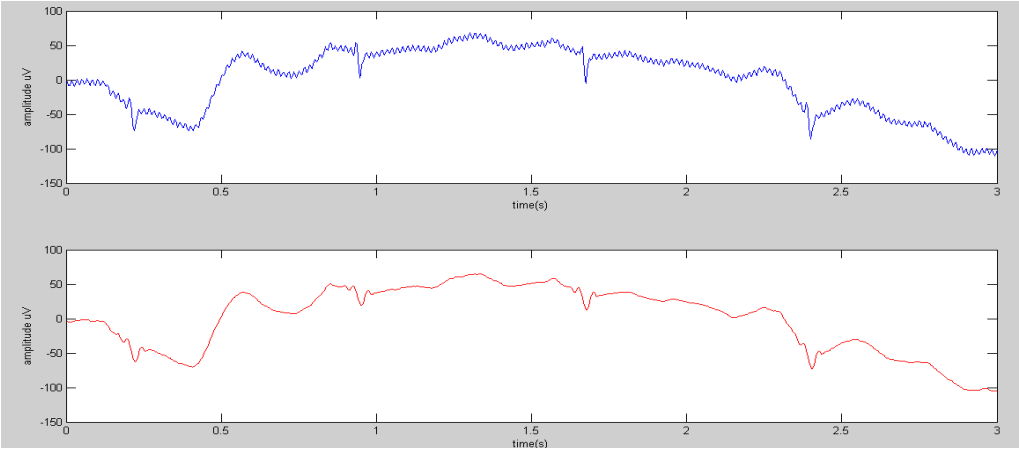

Figure 3.5.Savitzky-Golay Filter. In blue raw signal and in red filtered signal. Removal of high frequency noise is evident. Executed with polynomial 9 and windows size 0.1.

3.6 Candidate Detection

As mentioned in chapter 2 section 2.31, the data sets generated by the induced ischemia experiments are extensive; in particular those generated with high resolution electrodes. During the detection step we focused on small regions of interest called candidates.

Energy Operator

Prof. Erickson suggested the use of a technique employed in neural spike detection: the Smoothed Non Linear Energy Operator (SNEO), which is equivalent to the Teager Energy Operator (Teager 1980, Jabloun 1999). SNEO has two great benefits: it is really fast to compute and it is computationally "inexpensive".

For a continuous signal $s(t)$, the SNEO operator E_c is: $E_c[s(t)] = [\dot{s}(t)]^2 - s(t) \times \ddot{s}(t)$

For a discrete signal $s(n)$, the SNEO operator E_d is: $E_d[s(n)] = s(n)^2 - s(n+1) \times s(n-1)$

Moreover it has been shown that the energy E of a sine wave with amplitude A and frequency f is proportional to: $E \propto A^2 \times f^2$.

Spike waveforms have large amplitudes and high frequencies (figure 3.6). Given the proportional relation between SNEO and these two variables it is expected to see spikes having large SNEO values (figure 3.7). However, large SNEO values are not always indicative of spikes. Artifacts also have large amplitudes and high frequencies which will result in large SNEO values. We will refer to the SNEO as $E(n)$.

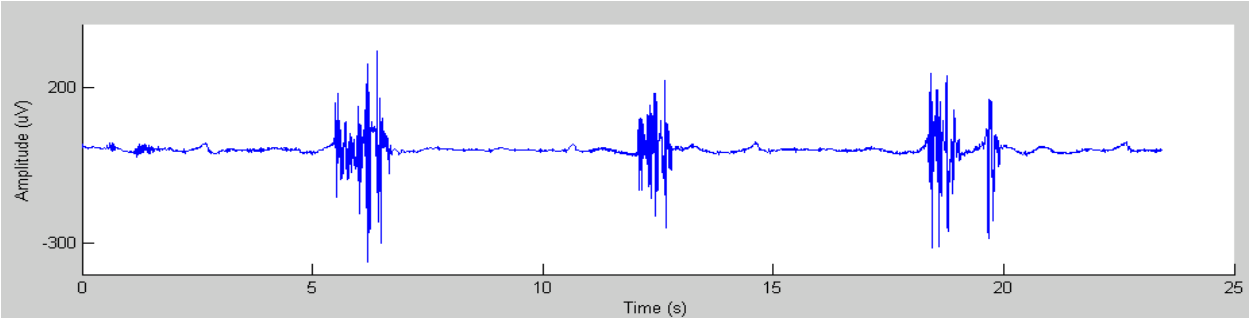

Figure 3.6.Filtered signal. Three evident spike clusters. See figure 3.7 for SNEO of this signal.

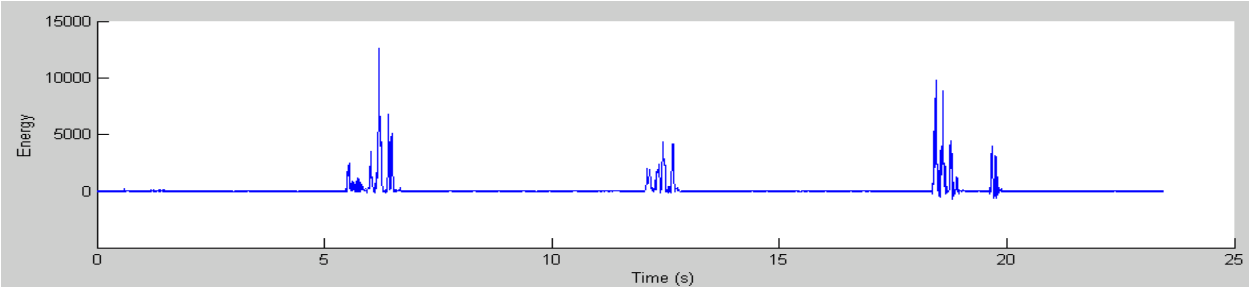

Figure 3.7. SNEO of signal in figure 3.6. Note high energy regions and energy scale.

Noise

We estimated the RMS noise ($\hat{\sigma}$) in the energy signal E(n). $\hat{\sigma}$ was obtained by computing the median of the absolute deviation of E(n) (Nenadic 2005, Erickson 2009). For a signal S(N), $\hat{\sigma}$ is defined as:

$$\hat{\sigma} = M\{|S(0) - \overline{S(t)}|, \dots, |S(N) - \overline{S(t)}|\} \div 0.6745$$

Where $\overline{S(t)}$ is the sample mean of $S(t)$ and $M\{\cdot\}$ denotes the sample median. This is a robust estimate of noise because it is not sensitive to outliers (Erickson 2009).

Detection Threshold

A detection threshold is set by the product of the estimated noise ($\hat{\sigma}$) and parameter k.

$$E_{threshold} = \hat{\sigma} \times \text{k}$$

Data samples with E(n) above $E_{threshold}$ are selected to move forward in the process.

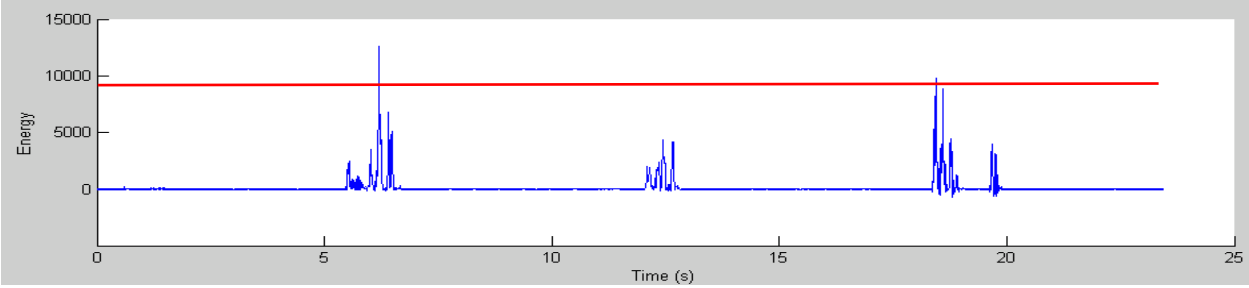

Figure 3.8. Detection threshold based on noise and parameter k. Contrast high detection threshold in this figure to threshold in figure 3.9. Different detection thresholds yield different candidates.

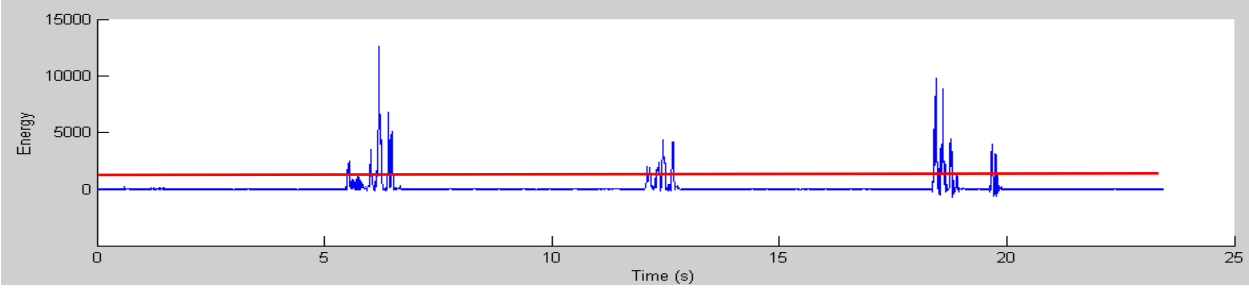

Figure 3.9. Detection threshold based on noise and parameter k. Low detection threshold captures a larger number of candidates

Grouping Samples into Clusters

The next step is to group the selected data samples into clusters. Samples separated by less than a preset threshold will be grouped together; else they will be separated into different clusters. The sample separation threshold is calculated based on the product of sampling frequency fs and the parameter DT. For example, samples S(N) and S(N + x) will be grouped together if:

$$(N + x) - (N) < fs \times DT$$

These clusters are known as the spike candidates. The information regarding the first and last data samples in a cluster is passed forward. These are treated as the beginning and ending of a spike burst.

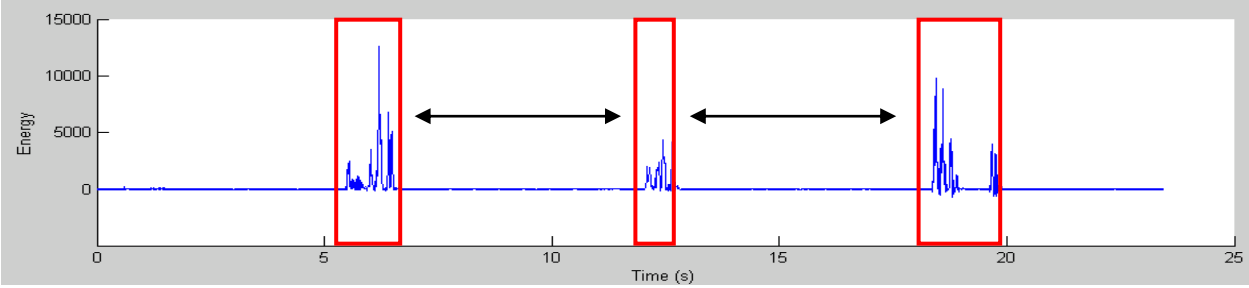

Figure 3.10. Clustering based on threshold. In this example large DT results in 3 spike clusters. Contrast to figure 3.11.

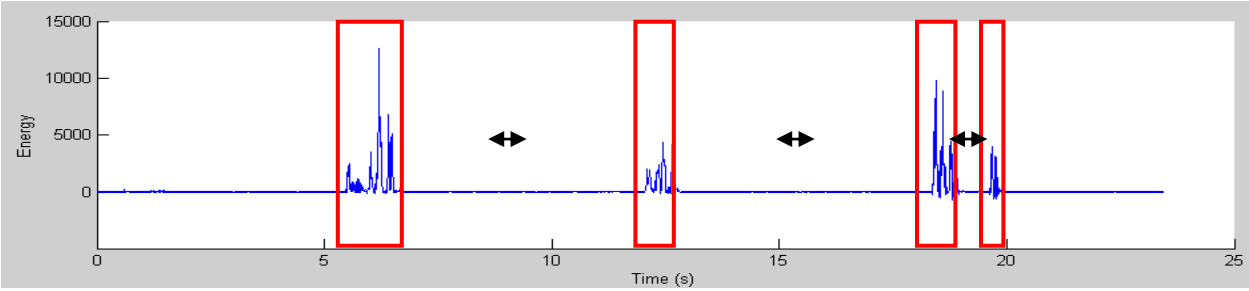

Figure 3.11. Clustering based on threshold. In this example small DTresults in 4 spike clusters.

Parameters

It is important to acknowledge the role played by the two detection parameters k and DT. As seen in figure 3.8, 3.9, 3.10 and 3.11, different parameter values often yield different results. We will analyze parameters effects on the algorithm's performance (AROC) in chapter 4 and suggest optimal values for these.

Initial Classification: Cluster Length

An initial classification step is candidate discrimination by cluster length. We compute the cluster length (in seconds) based on the start and end times. The clusters determined to be too short or too long according to user-defined limits are eliminated. We chose these restrictions:

$0.02 \text{ sec} \leq \text{Cluster length} < 3.5 \text{ sec}$

These limits are set according to physiological or waveform observations. For example, it is physiologically unlikely to observe a spike cluster which lasts 3 seconds. Clusters are usually shorter than that. Similarly, given that spikes occur in clusters it is unlikely to have a cluster which consists of two

data samples. For a 256 Hz sampling rate, the time between two samples is 0.0039 seconds; far too short to be a spike cluster.

3.7 Machine Classification:

The result of SNEO detection is a large number of candidates including spikes and non spikes. It is essential to classify these waveforms and select only spikes to move forward in the process. As we discussed in section _, the first step is simple cluster length discrimination. Next, we needed a more powerful method to classify waveforms based on their characteristics. Preliminary observations guided us toward choosing Support Vector Machines (SVM).

Machine learning is a powerful tool which relies on a computer's ability to recognize patterns in data and make intelligent decisions. As humans, we are always classifying objects in our minds based on their characteristics. Machine learning follows the same principle, but takes advantage of the computer's computational ability. A computer carries out complex mathematical operations and processes large quantities of information in a very short time. In chapter 2 section _, we discussed the difficulties that arise in the visual analysis of small intestine SERs. In comparison to the human eye, the machine is far better equipped to recognize underlying patterns in data; particularly for complex waveforms such as those in SERs.

Next, we will introduce the concept lying at the core of machine learning with a straightforward example. This example is intended particularly for the reader with no previous knowledge regarding machine learning.

Figure 3.12 shows fictitious data for the height and weight of children between the ages 3-5 and adults 18 and older. It is easy to see a pattern in the distribution of the data points. The majority of adults are clustered in the upper right corner; at higher weights and heights. On the other hand, children are clustered in the lower left corner; at lower weights and heights.

In SVM theory, weight and height are called feature vectors as they describe a particular characteristic of a data piece. The set of data containing feature vectors and their classification (child or adult) is referred to as the training set in SVM theory. The user must provide a training set to the SVM algorithm from which it will attempt to recognize any underlying patterns.

Training set = [weight, height, child or adult?]
Training set = [vector A, vector B, classification]

By modifying figure 3.12 it is easier to observe the data distribution. See figure 3.13.

However, the overlap between children and adults at the boundaries of the quadrants also becomes noticeable (figure 3.14). In figure 3.14, the green rectangle indicates the area where overlap is observed. The SVM algorithm also notices the overlap and more importantly it draws a separating plane between the two objects (figure 3.15).

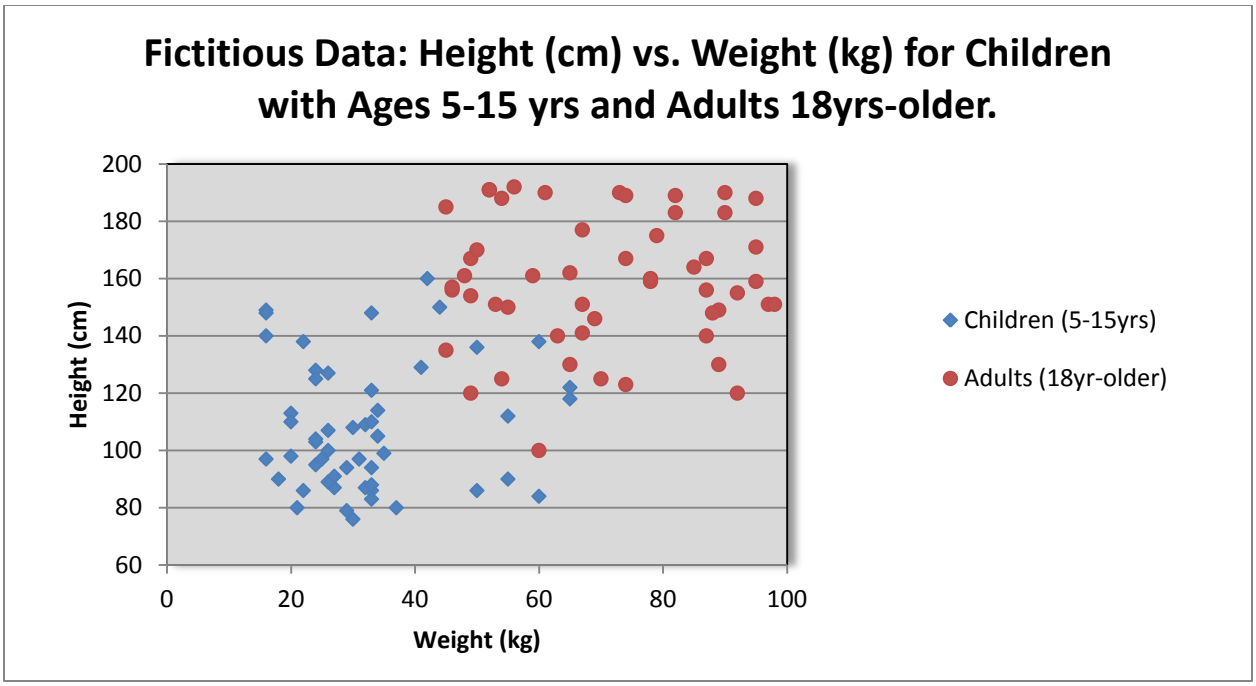

Figure 3.12. Fictitious data for height and weight of children and adults. Note evident data distribution.

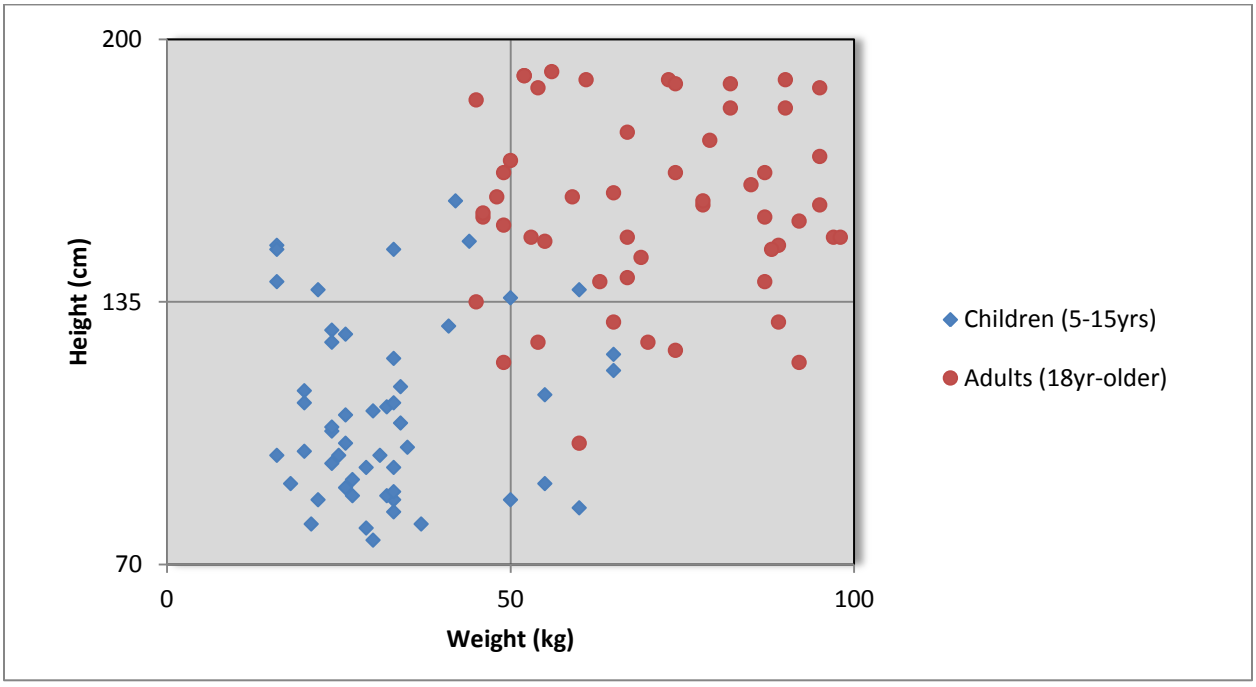

Figure 3.13. Fictitious data for height and weight of children and adults Plot area has been divided into four quadrants. Note that data distribution becomes more evident. Adults are clustered in upper right quadrant while children are clustered in lower left quadrant.

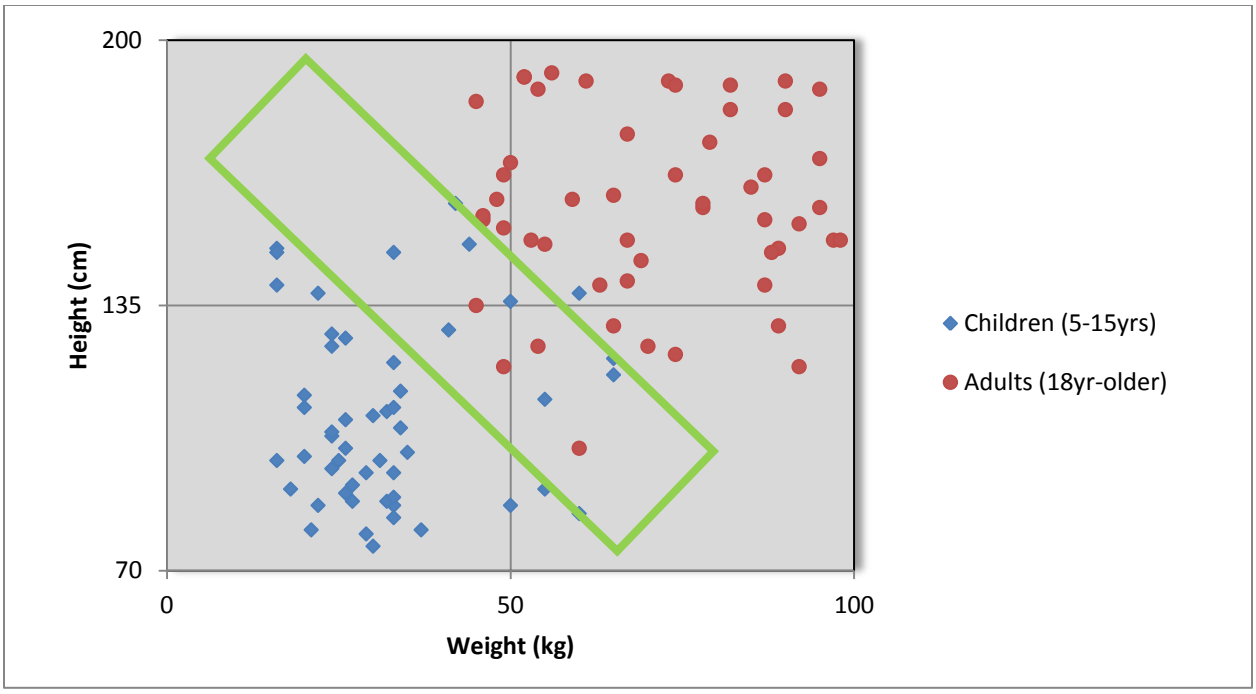

Figure 3.14. Fictitious data for height and weight of children and adults. Note overlap area emphasized by green rectangle.

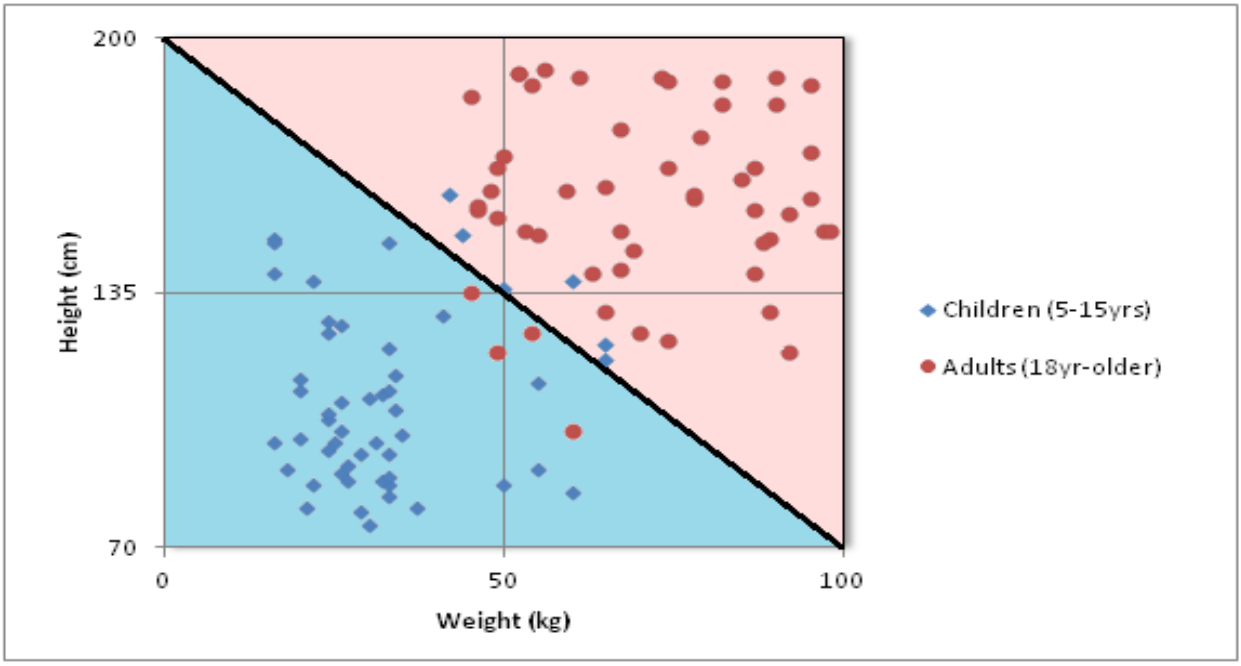

Figure 3.15. Fictitious data for height and weight of children and adults. Pink and blue regions indicate areas separated by the SVM-generated plane.

Figure 3.15 is an example of a separating plane that could be generated by an SVM algorithm on a 2 dimensional space (based on 2 feature vectors). The separating plane is calculated based on the training set characteristics. The pink region in the plot is the region suggested for adults and the blue region is suggested for children. New data will be classified either into a child or an adult based on its location in the relative to the separating plane (figure 3.16). Note that some adults fall into the light blue child region and some children fall into the pink adult region. Classification at the boundaries is complex due to the overlap but SVM produces a separating plane which will minimize errors. Following this stage we say that SVM has been "trained" and it is ready to classify new data.

Let's test the SVM classification with an example. We have two data points with the following characteristics: height 169 cm and weight 70 kg, height 100 cm and weight 35kg. If this information is passed onto a trained SVM, what will they be classified as? See figure 3.16.

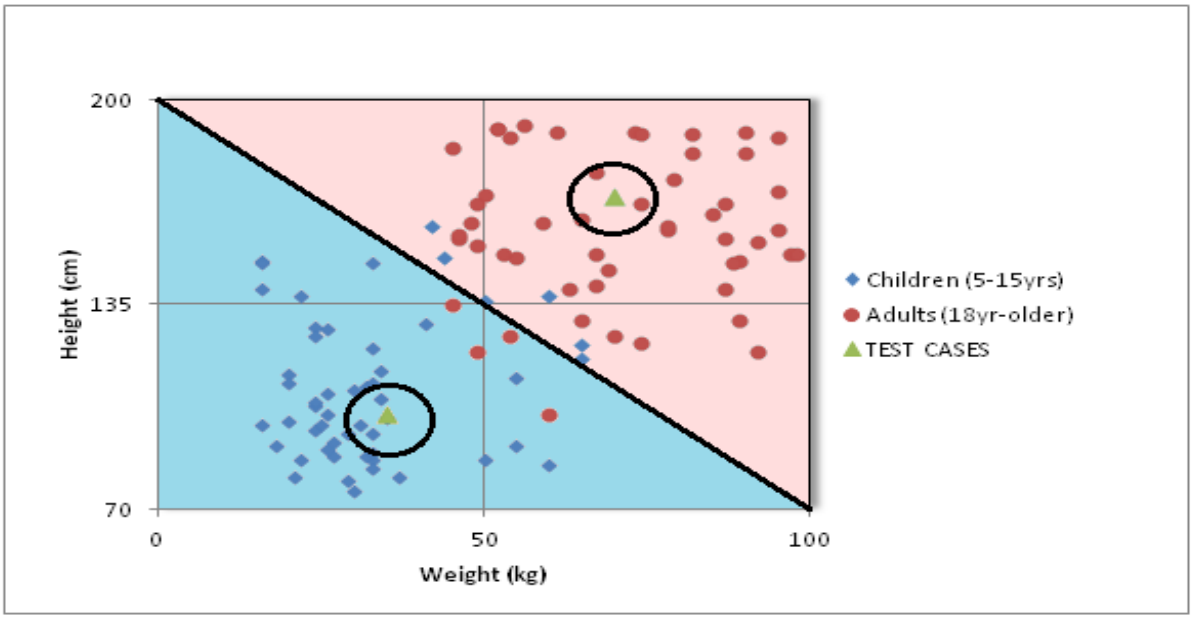

Figure 3.16. SVM test classification outcome.

According to figure 3.16, the test case [70,169] was classified as and adult. The test case [35, 100] was classified as a child. Once SVM is trained, the user only needs to provide information regarding the feature vectors. SVM will make a decision and return a classification.

Test Case = [weight, height] or Test Case = [feature vectors]

Returned by SVM = [feature vectors, classification]

Even though this example is very simple, it exposes an important point: real data overlaps and as such classification at the boundaries is difficult. Thus, SVM provides a powerful and consistent method for classifying data and optimizing classification at the boundaries.

Considerations about SVM

In the previous example we saw how SVM generated a separating plane between the data sets based on the feature vectors height and weight. As explained by Prof. Erickson: SVM tries to optimize the hyperplane such that it maximizes the minimum distance from any of the feature points. Refer back to figure 3.13. SVM "wants" to find the plane that separates children from adults, but stay as far away from both children and adults as possible. The points that are closest to the plane (figure 3.15) are actually called the "support vectors", because they "support" the drawing of the hyperplane.

The mathematics concerning SVM are complex and more detail is available in Lutz 2009: We implemented Matlab's SVM function from its Bioinformatics Toolbox. We used the Gaussian Radial Basis Function (RBF) to train SVM. In this approach, data is separated on radial symmetry. The influence of a data point falls off like a Gaussian curve in the radial direction. Prof. Erickson suggested RBF because it allows the generation of non-linear hyperplanes. A non-linear hyperplane is more flexible and could model our data more appropriately.

Moreover, it is important to acknowledge that SVM classification will not be perfect. The planes are drawn so as to optimize results, but some samples will be misclassified. Data overlap, even at a small extent, is always likely to occur.

3.8 Candidate Windows

In order to carry out classification, we need to provide SVM with the features vector describing a waveform. We computed four features for every candidate cluster: signal to noise ratio (SNR), integrated energy per unit time (IEpsec), mean-crossing points (MCPpsec) and median time between mean-crossing points (MTimeMCP).However, there is an intermediate step previous to feature computation: the conversion of candidate clusters into candidate windows of a given length.

From SNEO detection we are provided with the alleged start and end coordinates of candidate clusters. However, it is possible that these start and end points do not coincide with the actual start and end coordinates of the clusters. This arises from the fact that the initial and final spikes in a cluster are smaller than those in the middle section. Thus, it is possible that SNEO detects a cluster shorter than the actual one. See figure 3.17 and 3.18.

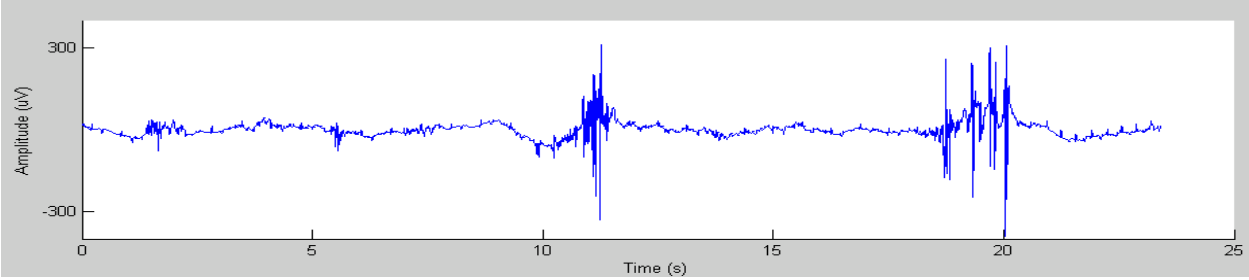

Figure 3.17. Raw signal. Two evident spike clusters.

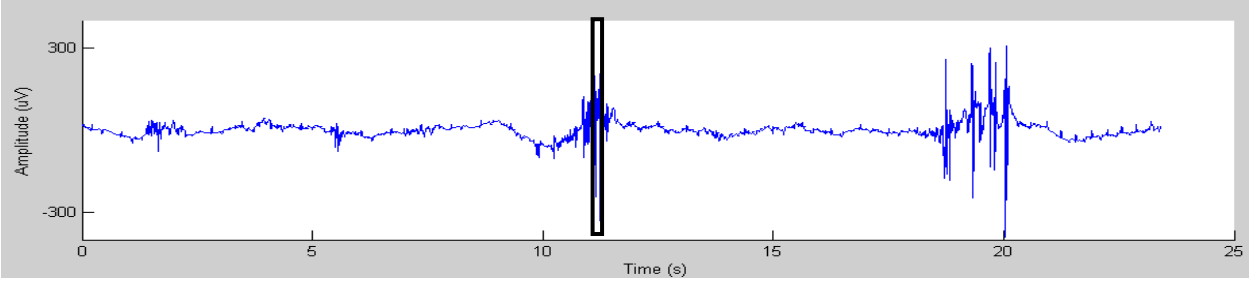

Figure 3.18. First cluster is detected by SNEO. However, starting point is shifted to the right. Detected cluster is shorter than actual cluster.

In figure 3.15 we observe that the detected cluster is shorter than the actual; the start point is shifted rightwards. In order to minimize cluster limits inaccuracies and for ease of data processing we decided to expand the clusters into data windows of a given length. Window length is equal to twice the parameter windowL.

A data window is obtained by: computing the midpoint of the spike cluster and centering the window on this midpoint. Figures 3.19 and 3.20 show the effect of generating a larger window around a short cluster.

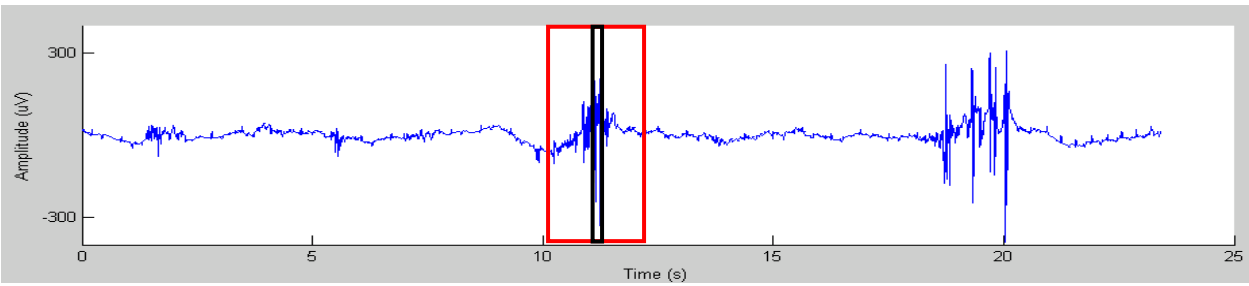

Figure 3.19. Cluster detected by SNEO is shown by black rectangle. Candidate window is shown by red rectangle. Note that window encompasses a larger area than cluster.

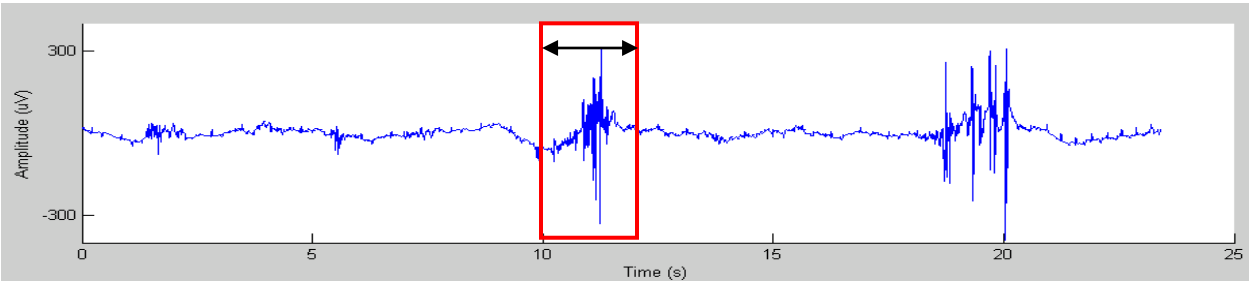

Figure 3.20. Candidate Window. Note that the entire cluster is found within the window. Arrow indicates window length (2 x windowL).

3.9 Feature Vectors

Signal to Noise Ratio (SNR)

This feature calculates the ratio between the signal in the candidate window and noise. The signal is estimated by calculating the standard deviation σ for the samples S(n) in the small candidate window.

$$\sigma = \sqrt{\frac{\sum_{i=1}^{N} S(i)^2}{N} - \left(\frac{\sum_{i=1}^{N} S(i)}{N}\right)^2}$$

Where N is the total number of samples in the window.

Noise is estimated by computing the median of the absolute deviation. See section 3.5 for more details. Importantly, noise is computed over the entire data length for the channel, not just within the small window.

We expect spike windows to have high SNR. However, a high SNR is not always indicative of a spike cluster. Artifacts and the fast component of the slow wave could also yield high SNR.

Integrated Energy per Unit of Time (IEpsec)

We saw the energy operator SNEO is utilized previously in candidate detection. The energy operator is utilized again for calculating this feature. The IEpsec; as the name indicates; is the integration of E_d for the whole candidate window divided by the window length. (Remember that E(n) refers to the SNEO). See below for illustration.

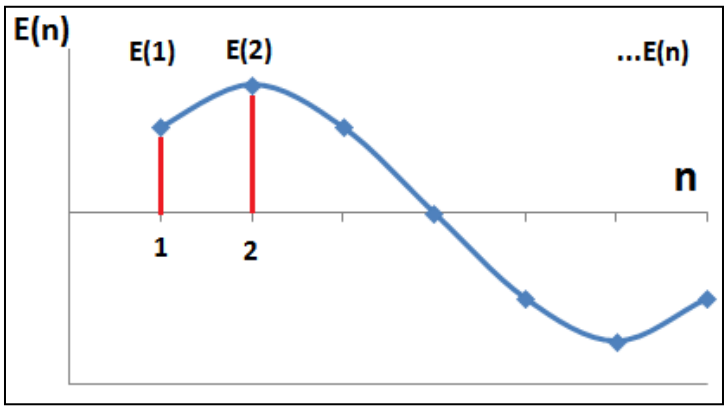

Figure 3.21. Illustration of SNEO signal or E(n).

$$\mathrm{IE} = \sum_{i=1}^{n} E(i)$$

$$\mathrm{IE} = \big(\mathrm{E}(1)\big) + \big(\mathrm{E}(2)\big) + \ldots + \big(\mathrm{E}(\mathrm{n})\big)$$

$$\mathrm{IEpsec} = \frac{\mathrm{IE}}{2 \times \mathrm{windowL}}$$

We expect spike windows to have large values of IEpsec.

Mean-Crossing Points per Unit of Time (MCPpsec):

The feature called "mean-crossing" aims to trace how many times the signal goes above and below a certain value. The threshold value chosen is the mean for all the data points in the candidate window. The "mean-crossing" feature is based on the idea that if you draw a horizontal line through a typical spike you will observe the signal going up and down through it several times. Thus, we say that a spike has a large number of mean-crossings in a small amount of time. On the other hand, if we draw the same horizontal line across a slow wave we will observe that the signal crosses once, twice or at most thrice through the line. The mean-crossing feature attempts to quantify the fast upward and downward deflections of typical of spikes. It is a simplified approach of the one presented by Liang et al. (1997) where they focus on: amplitude spectrum and maximum derivative. MM filtering is extremely important for this feature because it removes the wandering baseline and allows capturing the deflections crossing through a straight horizontal line.

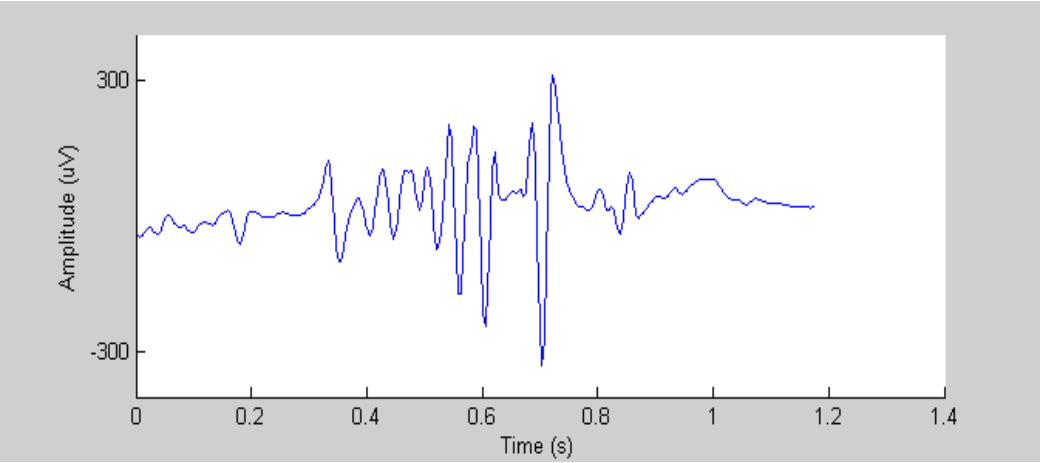

Figure 3.22. Example showing candidate window with spike cluster

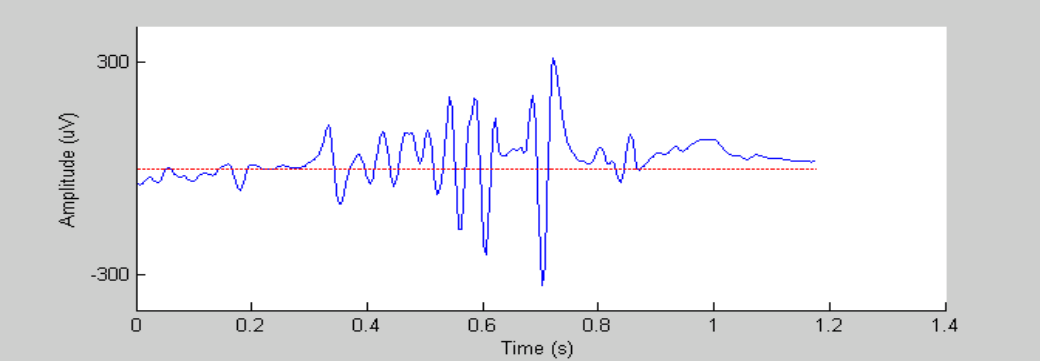

Figure 3.23 Example showing that a spike cluster generally has a high number of MCPpsec. In this example, number of mean crossing points is 26. In reality, steps are taken to discriminate crossings that have low amplitudes; i.e. points that to cross the mean but do not go far up.

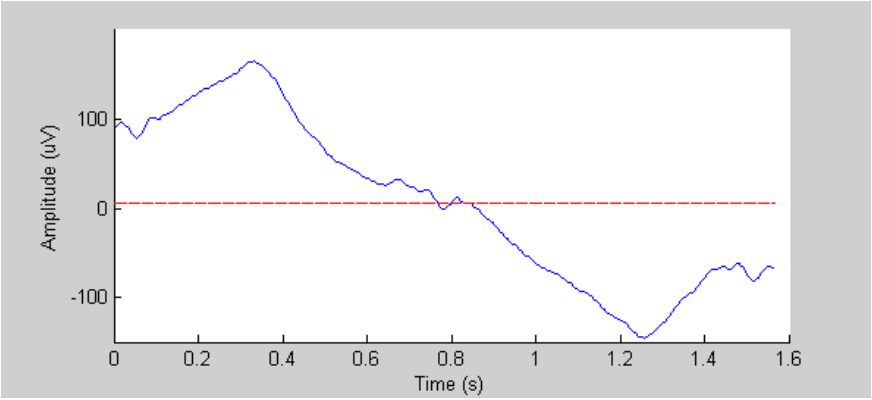

Figure 3.24. Slow frequency waveform. These waveforms usually very low MCPpsec. For this case number of mean crossing points is 3. In reality, steps are taken to discriminate crossings that do not reach far up like the ones observed here. The number of mean crossing points could be reduced to 1 or 2.

While it is expected that spike clusters will have a larger number of MCPpsec; a large number of MCPpsec is not always indicative of a spike. The example in figures 3.25- 3.27 illustrates this claim.

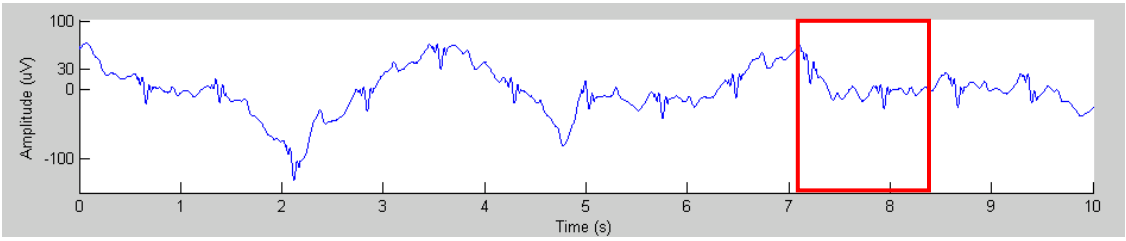

Figure 3.25. Selected candidate window shown by red square. It is evident that candidate is not a spike cluster. Furthermore, data in channel does not reach amplitudes higher than 100 uV.

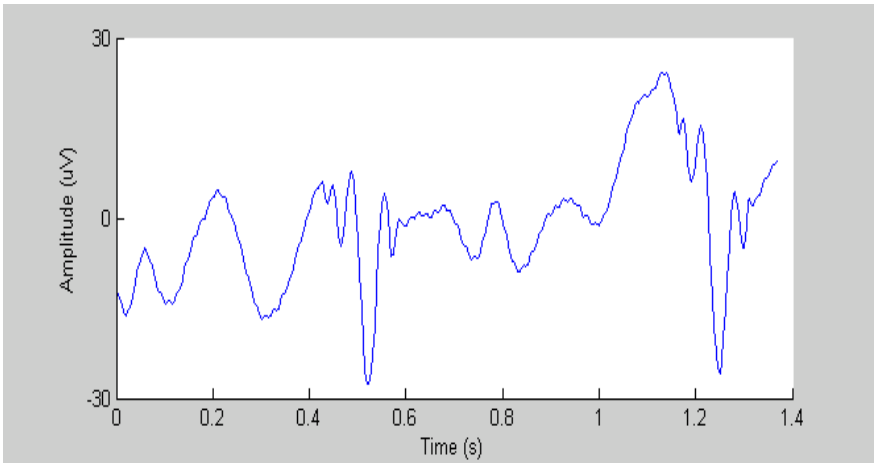

Figure 3.26. Zoomed in view of candidate window reveals it is a noisy signal with very small amplitude (30uV)

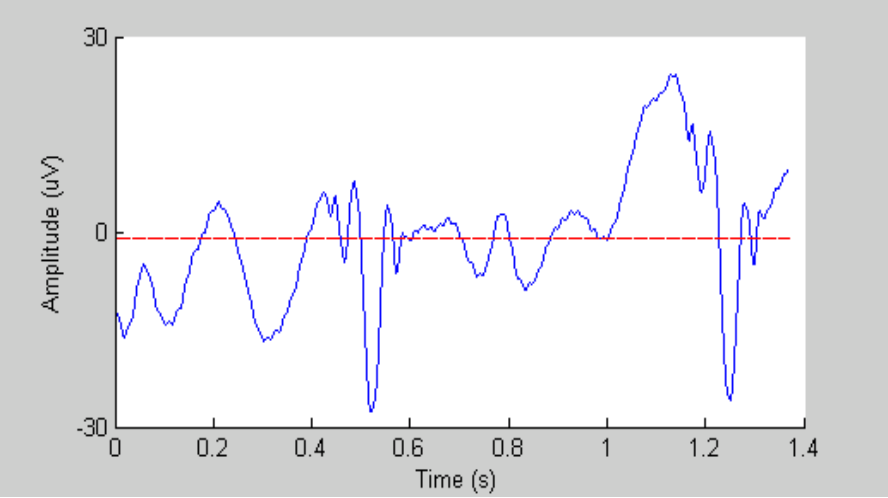

Figure 3.27. This candidate results in a high number of MCPpsec in spite of not being a spike cluster. Number of mean crossings is 23; comparable to spike cluster in figure 3.23.

The MCPpsec computation includes small modifications to eliminate crossing points that are too close to each other or points located on peaks which do not go up to high amplitudes.

Median Time between Mean-Crossing Points (MTimeMCP)

The fourth and final feature computes the times between mean-crossings points in a window, sorts them out and selects the median value. We expect spike clusters with large number of MCPpsec to have a short MTimeMCP.

The final features vector is summarized below:

Feature vector for signal s(t) = [SNR, IEpsec, MCPpsec, MTimeMCP]

While SNR and IEpsec are more widely used in signal processing, MCPpsec and MTimeMCP are based on initial empirical observations and serve a trial-and-error purpose. The usefulness of each feature in the vector will be evaluated during the cross validation in chapter 4. If results indicate that MCPpsec and MTimeMCP do not provide benefits they will be removed and new features could be investigated if necessary

3.10 Training Set for SVM classification

Training Samples Classification

In order to train SVM we generated a large number of training samples. We ran SNEO threshold detection on several data segments and obtained 1-second long candidate windows. SNEO detection was performed with a low k parameter (k=5) to detect spikes as well non spikes (See figures 3.28 and 3.29). Candidates were analyzed within a 30 second display of channel data. An observer classified each sample through visual inspection. Classification of each sample was done conservatively. Classification was stored in the following format: 1 for spikes and 0 for non spikes.

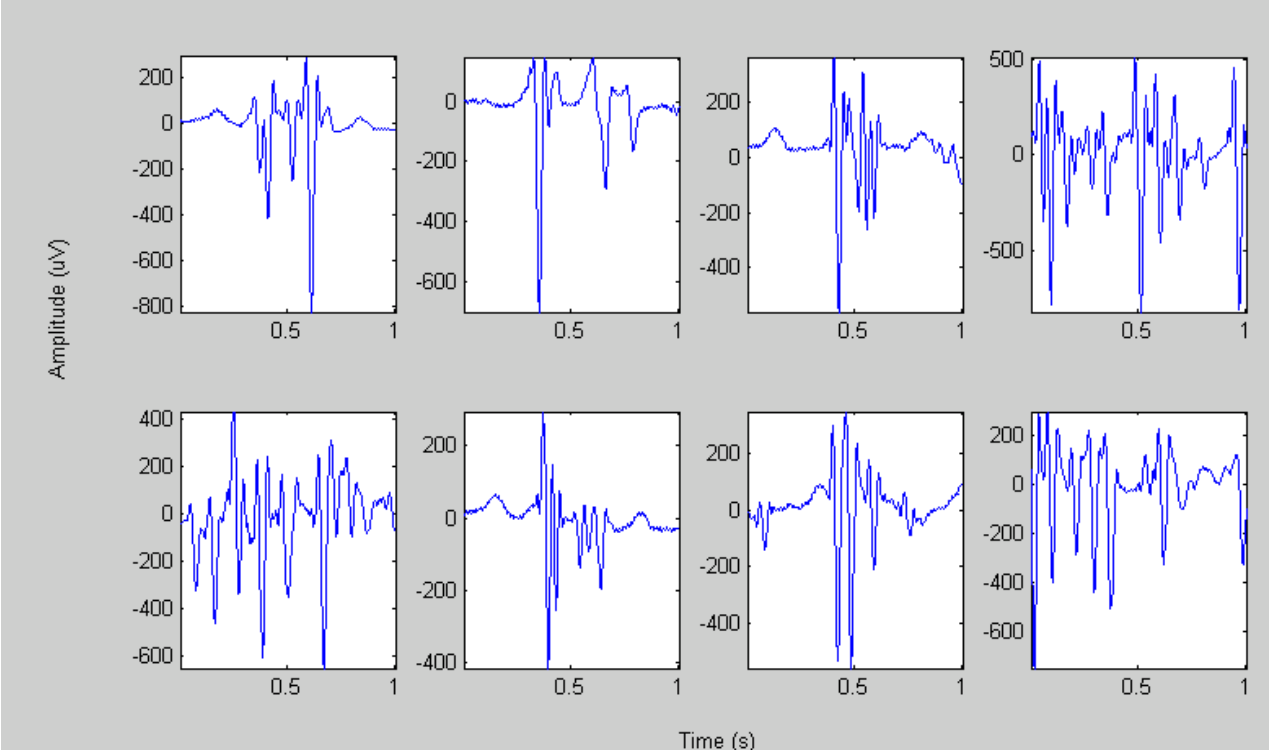

Figure 3.28. Training samples passed onto SVM. All of the samples here were classified as spikes given their waveform characteristics: amplitude, frequency.

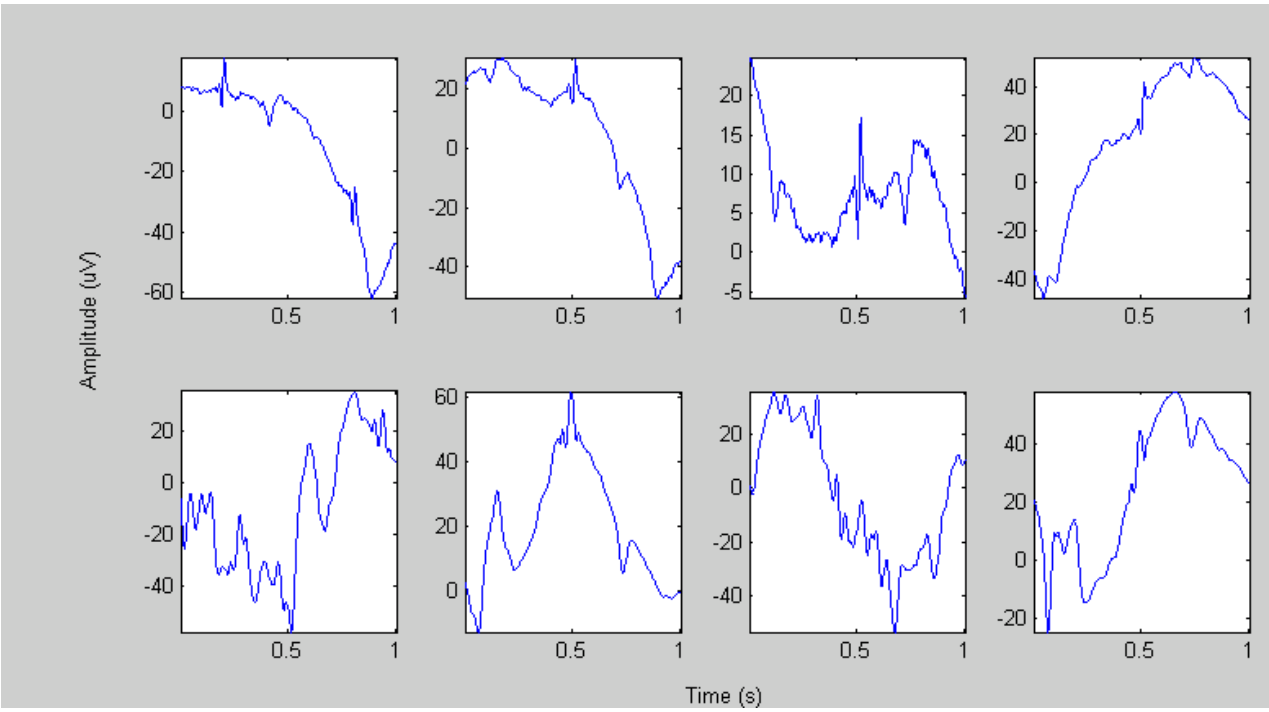

Figure 3.29. Training samples passed onto SVM. All of the samples here were classified as non spikes given their waveform characteristics: amplitude, frequency

Training Set

Consisted of approximately 2300 training samples of which 80% are non spikes and 20% are spikes. Training samples were selected from following data sets:

Table 3.2. Information of data sources used to generate the training samples set.

	Data set	Experiment	Time	Filter		General Observations
			(40 channels)	SG	Mov. Median	
1	01.22.10	01b	415_445s			Cardiac + few spikes
		01b	365_395s			Cardiac + few spikes
2	04.14.09	c	60_90s			Few spikes
		c	960_990s			
		a	1110_1170s			baseline
3	04.15.09	c	1090_1120s			
4	04.16.09	d	130_160s			
5	04.17.09	c	500_530s	0.09	0.5	Strong cardiac/ no clear spikes
6	05.03.11 Auckland	Pig 33 exp 9	260_280s	0.1	0.5	Baseline +slow wave
		Pig 33 exp10	210_230s			Long spike clusters, spread through channels
		Pig33exp10	270_290s	0.1	0.5	
7	05.22.09	b	25_85s			Few spikes
		a	600_660s			Baseline
8	05.28.09	01b	2700_2730	0.09	0.5	Noisy data, artifacts, cardiac , baseline wander
9	05.29.09	b	31_61s	0.09	0.5	Nice spikes, can see spread through channels
		b	151_181s	0.09	0.5	Lots of spikes, spread through channels
		a	200_230s	0.09	0.1	Baseline, Slow wave
10	06.01.11 Auckland	Pig 34 exp 10				Baseline
		Pig 35 exp 12	300_330s			
		Pig 35 exp 13	1210_1240s			

3.11 Final Algorithm Step: Additional Discrimination:

This is the final step in the algorithm and it consists of several user-defined restrictions on the signal features. This final step aims to reduce the number of FPs; signals misclassified by SVM. These restrictions are set to be lenient, only targeting candidates with features which are evidently uncommon for spikes. For example, MPCpsec is required to be greater or equal to 1. A signal having MCPpsec=0 could have been classified erroneously by SVM given its other features (SNR, IEpsec, etc). However, we will argue that a candidate with MCPpsec= 0 is unlikely to be a spike and should be eliminated. Furthermore, we expect spikes to have MPCpsec much larger than 1, between 15 and 30. However, the restriction is set to 1 because we only want to eliminate candidates which have evident non spikes

features. Otherwise, if we set strict restrictions based on observed values we would be undermining SVM's classification power.

The values for the restrictions were obtained from analyzing the training samples. See chapter 4 for more details. Typical values for spikes were compared to values for non spikes and these limits were chosen. This is an additional step and the restrictions can be modified by the user.

The conditions were the following:

- $0.5 < SNR < 15$
- $0 < IEpsec < 30{,}000$
- $1 \leq MCPpsec$
- MTimeMCP < 0.15 seconds

3.12 Algorithm Design Summary

In chapter 3 we introduced the metrics used to measure the algorithm's performance and described in detail each step in the algorithm. Moreover, we saw examples for every processing step and gained understanding about how spikes are detected and classified. Figure 3.30 provides a detailed summary of the algorithm; this is an expanded version of the diagram presented at the beginning of this chapter (figure 3.2). Chapter 4 will present the results obtained from algorithm validation and discuss the algorithm's performance.

Figure 3.30. Diagram: Summarize Algorithm Flow. See text under each heading for details regarding each step.

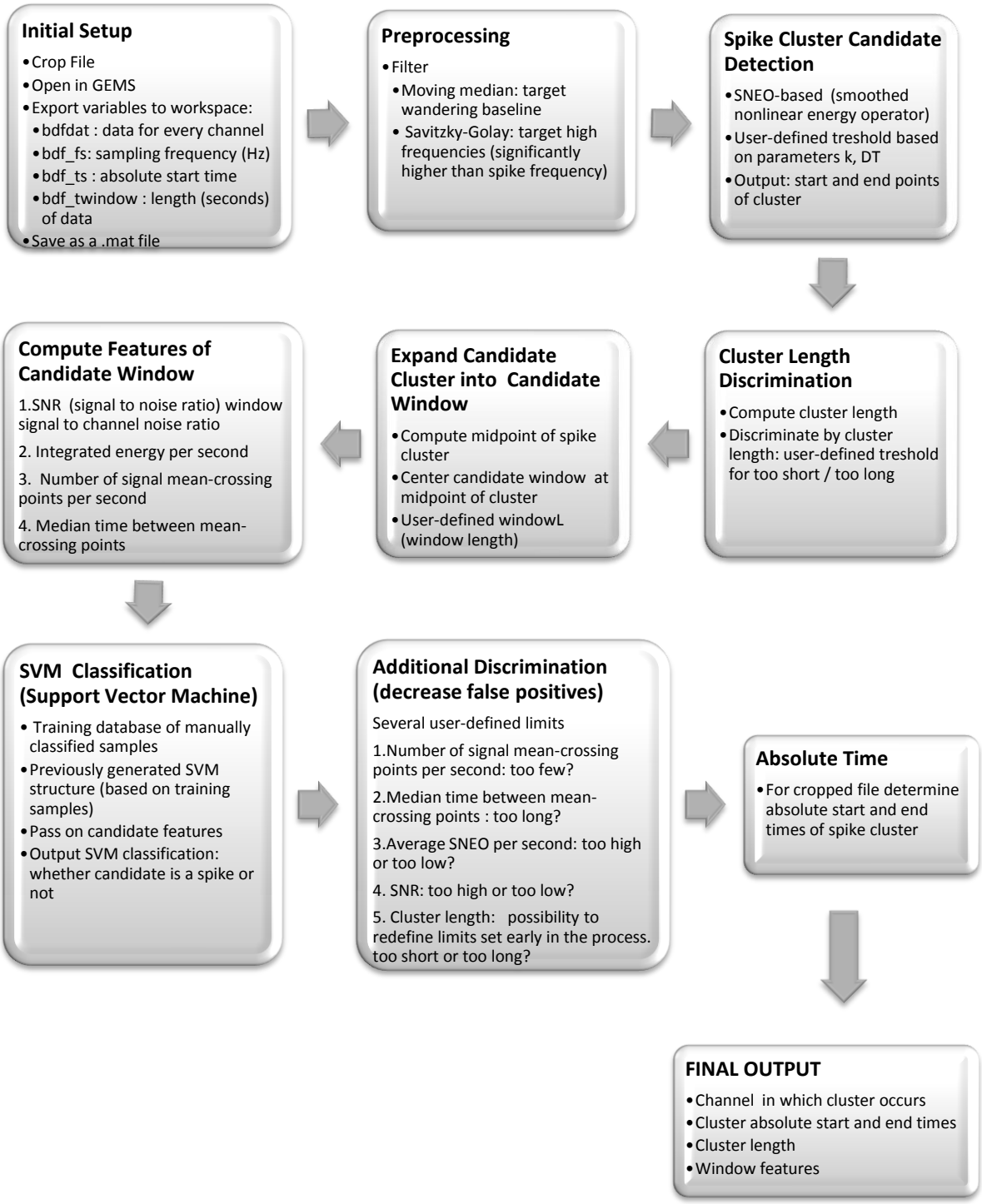

Chapter 4

Results: Tendencies in Data and Algorithm Validation

4.1 Training Samples: Tendencies in Data

As mentioned in chapter 3 we generated 2300 samples for SVM training. Samples were classified by an observer as spikes or non spikes. In this section we analyze the data tendencies observed in these samples. We will focus on three features computed for the training samples: SNR, IEpsec, MCPpsec (introduced in chapter 2). See figures 4.1 through 4.7 for illustrations of observations.

Summary of observations:

- Low levels of SNR: overlap amongst spikes and nonspikes. (figure 4.1)
- Low levels of IEpsec: overlap amongst spikes and nonspikes. (figure 4.2)
- Non spikes are clustered at very low levels of IEpsec. (figure 4.2)
- Extensive overlap amongst spikes and nonspikes for all levels of MCPsec. (figure 4.3)
- 3D: Spikes and non spikes seem are clustered in the low SNR, low-medium MCPsec area. (figure 4.5)
- 3D:Data separation between spikes and non spikes becomes evident at high levels of MCPsec. At high levels of MCPpsec spikes have higher SNR than non spikes. This could arise from non spikes which have high levels of noise and thus high MCPpsec but low SNR. Spikes with high MCPpsec tend to have high SNR. (figure 4.6)
- 3D: It is possible to observe data separation between spikes and non spikes along the vertical IEpsec axis. Spikes extend into regions of higher IEpsec. (figure 4.7)

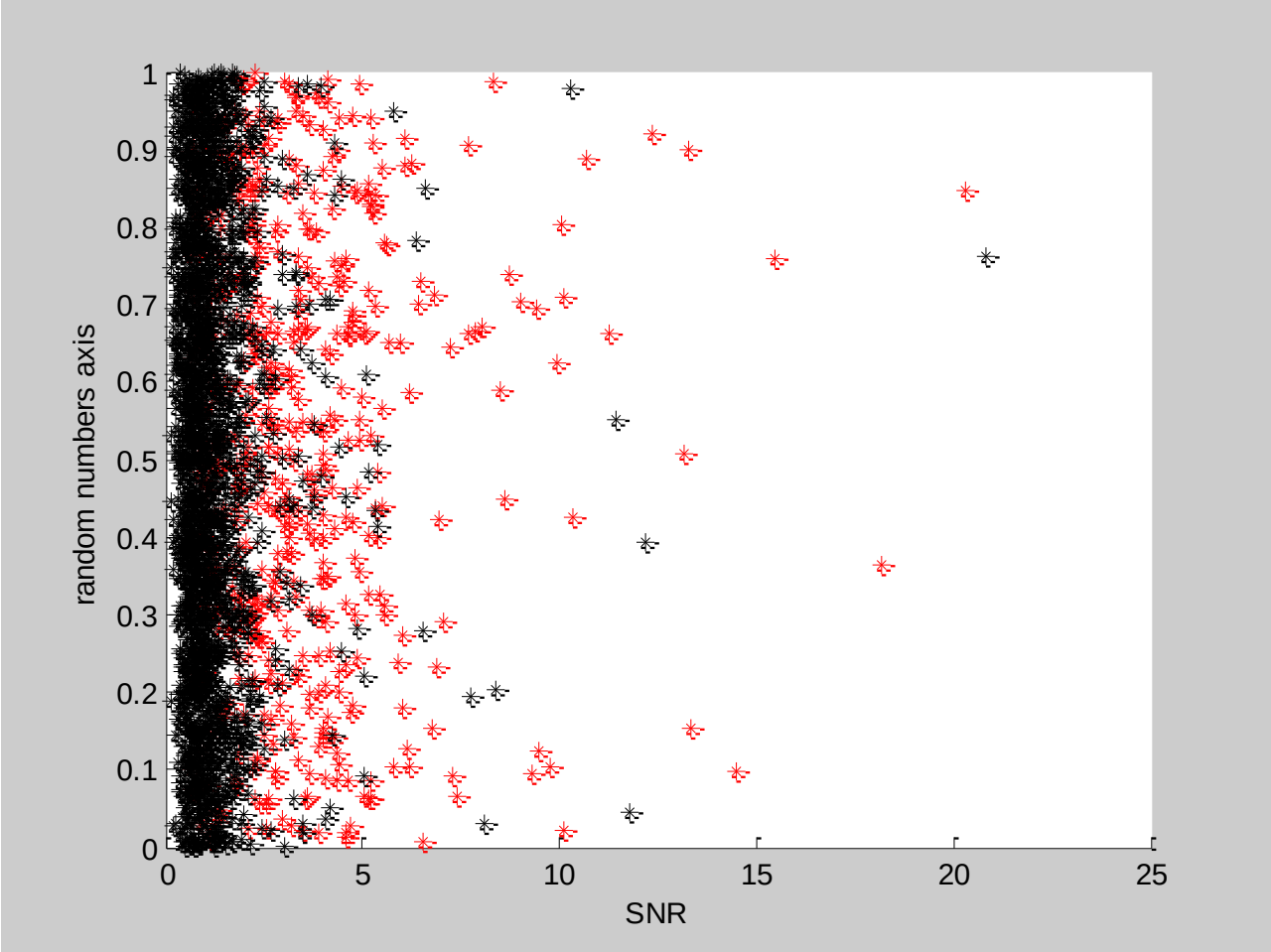

Figure 4.1.Red:spikes. Black: non spikes. For low levels of SNR there is overlap amongst spikes and nonspikes. Separation between waveforms starts close to 0.5 SNR.

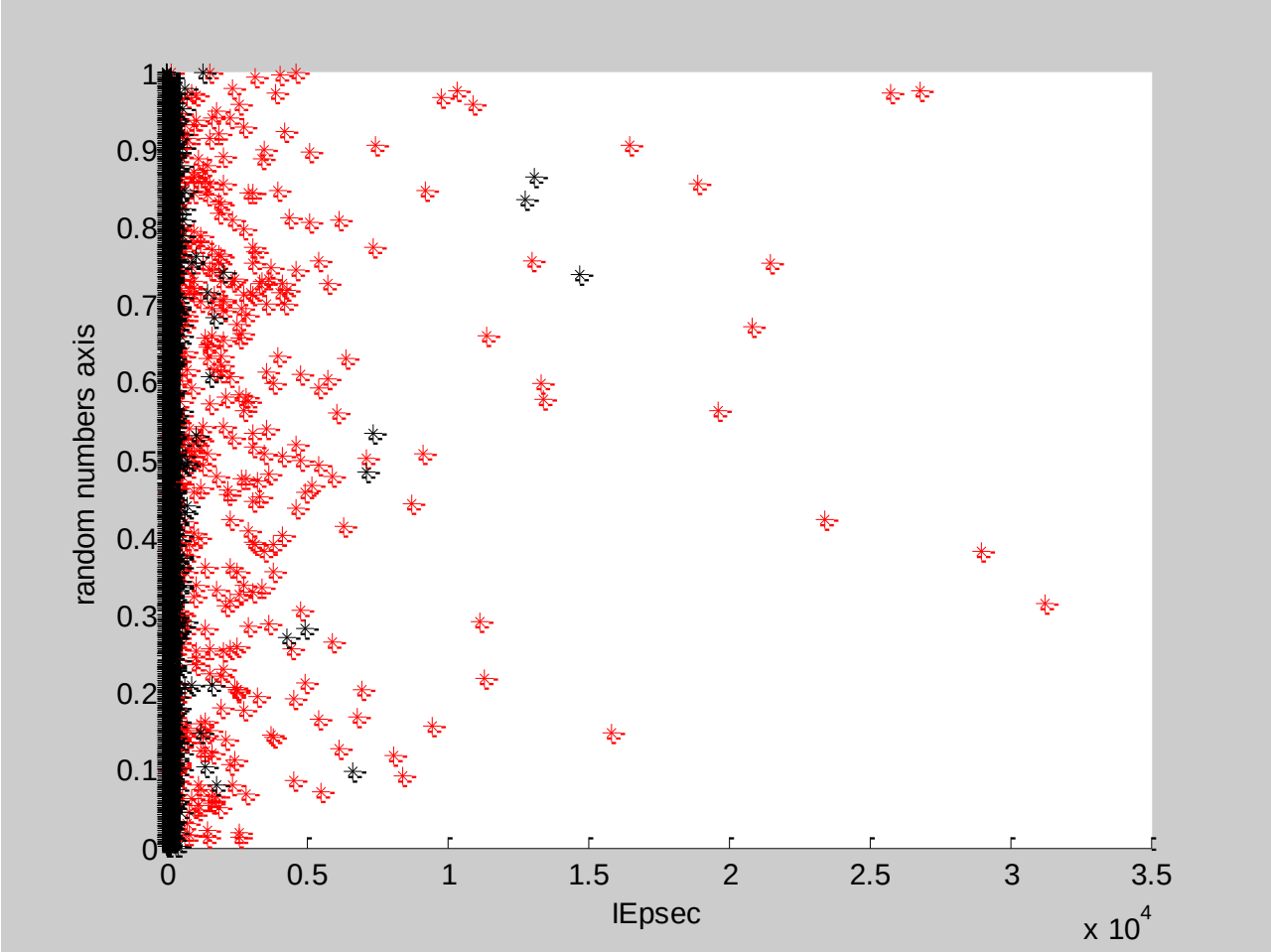

Figure 4.2. Red:spikes. Black: non spikes. For low levels of IEpsec there is overlap amongst spikes and nonspikes. Separation amongst waveforms starts at higher levels of IEpsec. Non spikes are clustered at very low levels of IEpsec.

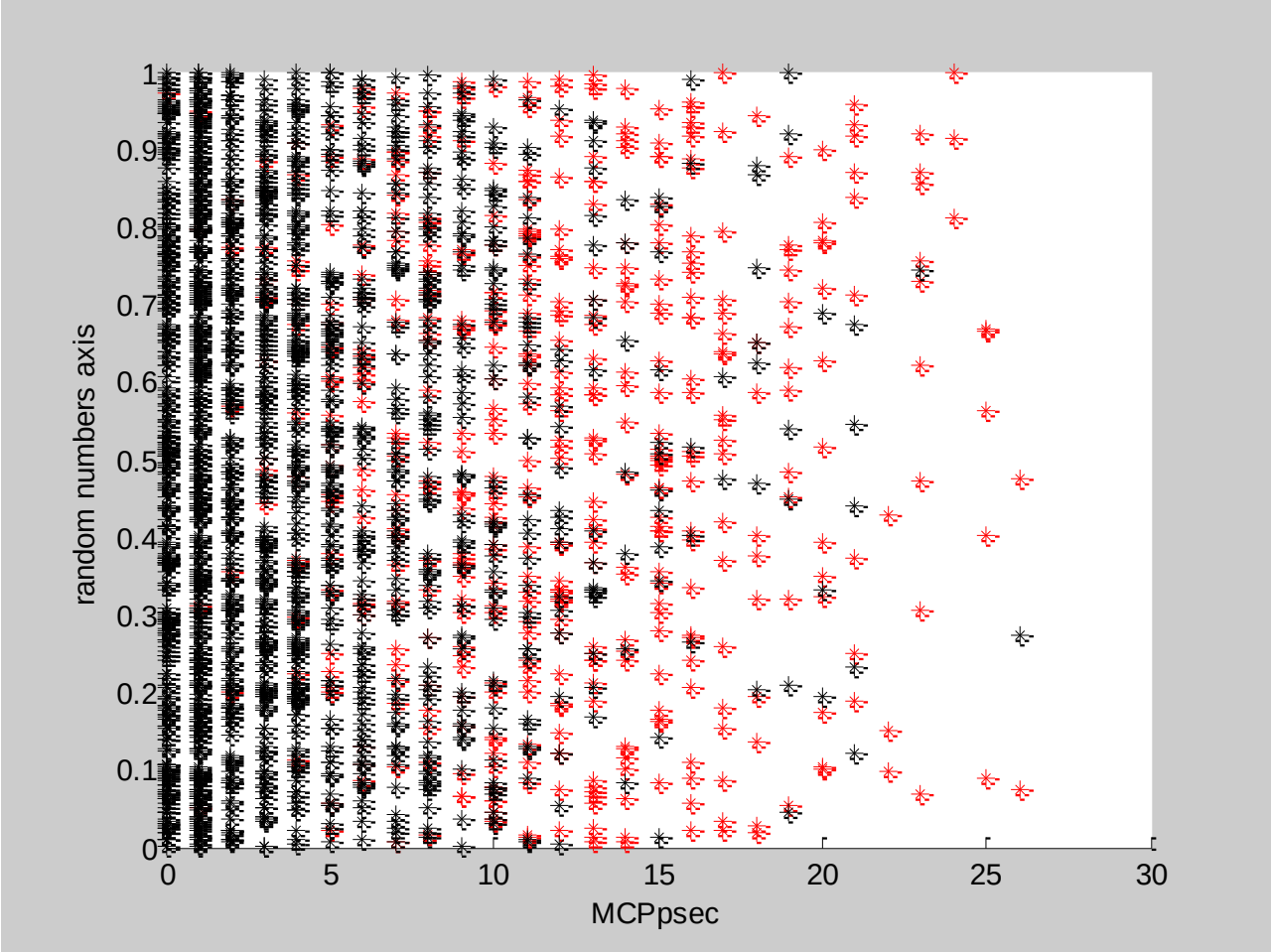

Figure 4.3. Red:spikes. Black: non spikes. There is extensive overlap amongst spikes and nonspikes for all levels of MCPsec. Slightly more spikes at levels of 15 MCPsec and higher.

Three-dimensional Space: SNR ,.IEpsec , MCPpsec

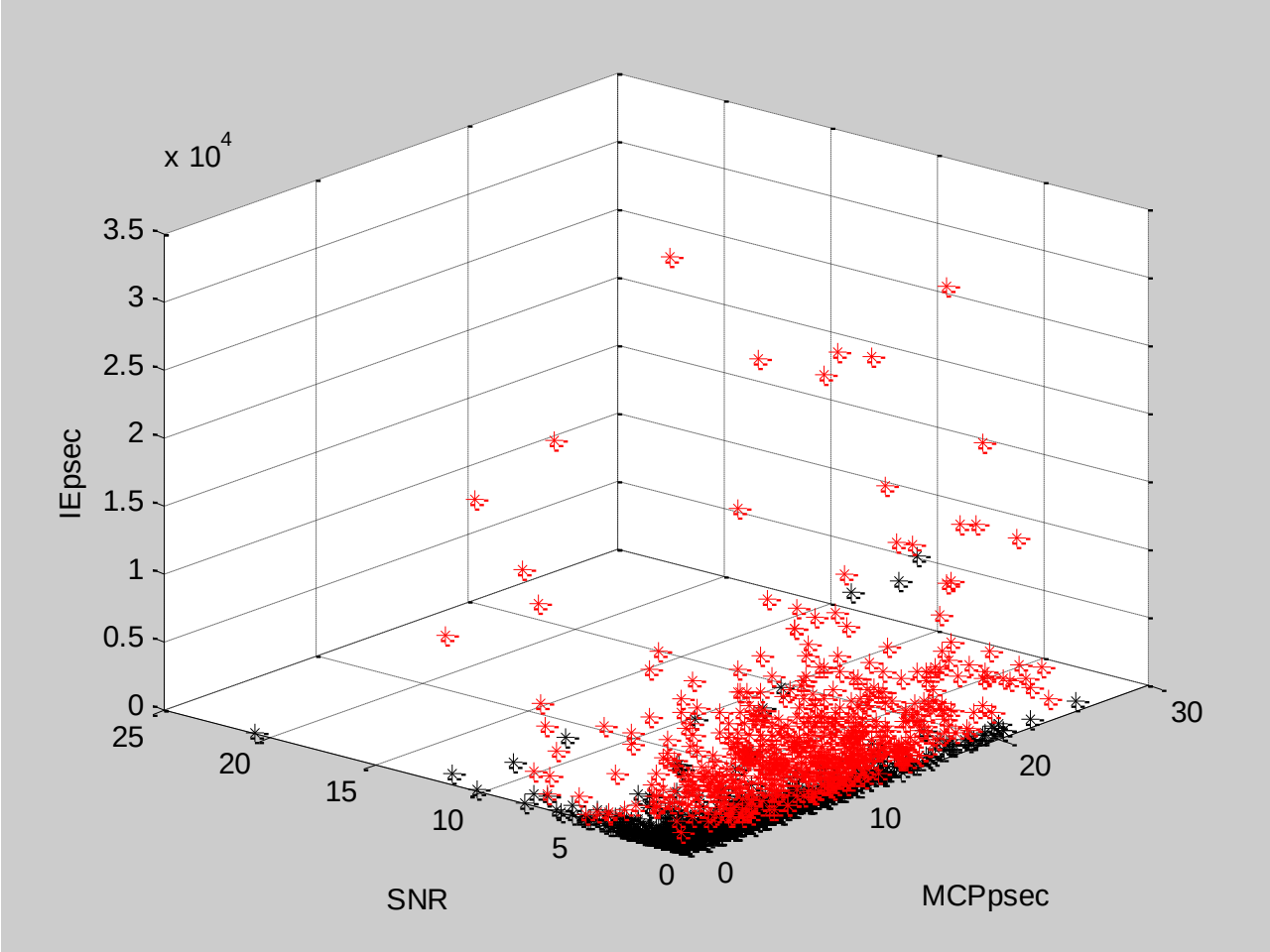

Figure 4.4. Red:spikes. Black: non spikes. Both spikes and non spikes seem are clustered in the low SNR, low-medium MCPsec area.

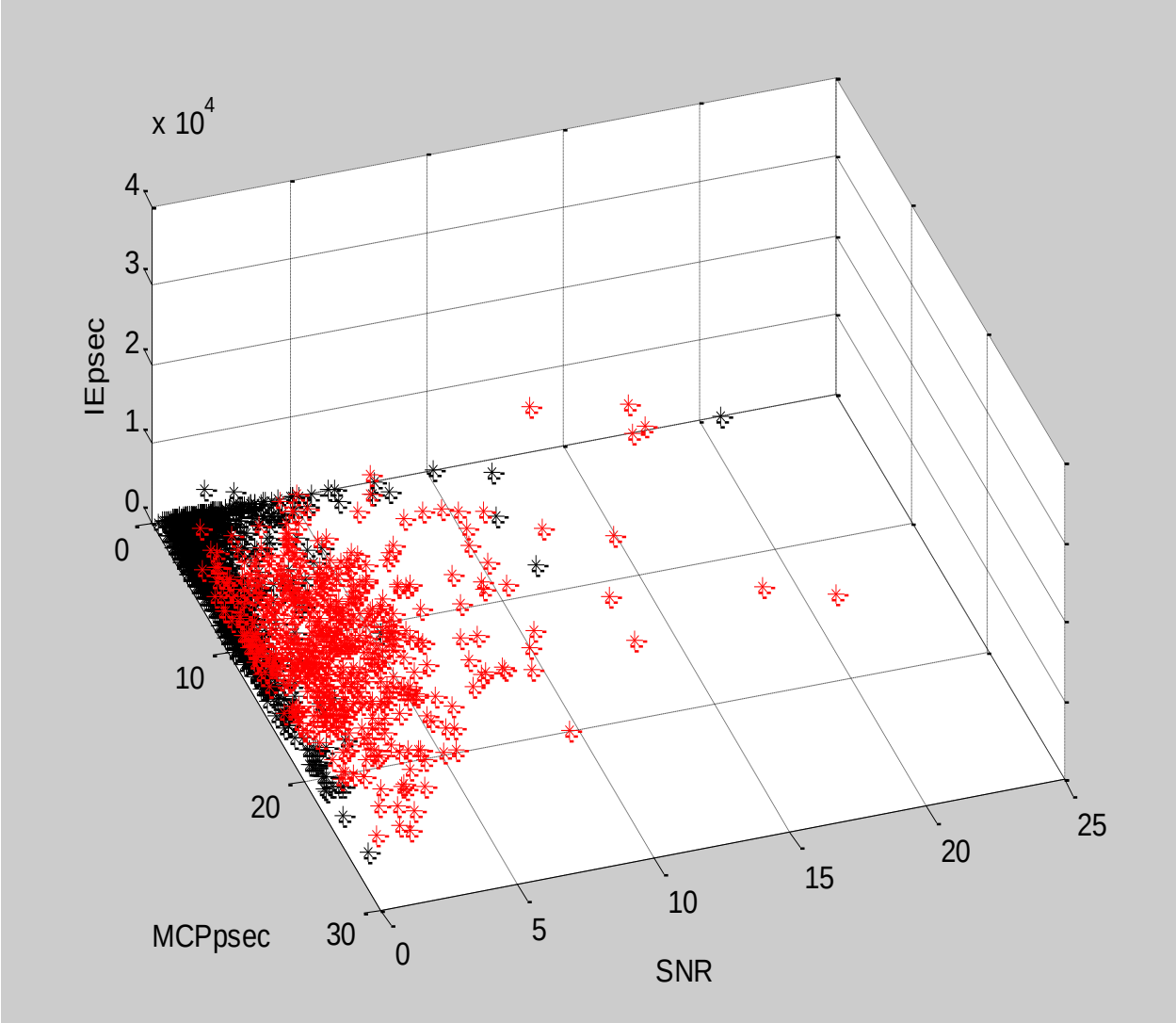

Figure 4.5. Red:spikes. Black: non spikes. Start to see some data separation in the plane MCPpsec vs. SNR.

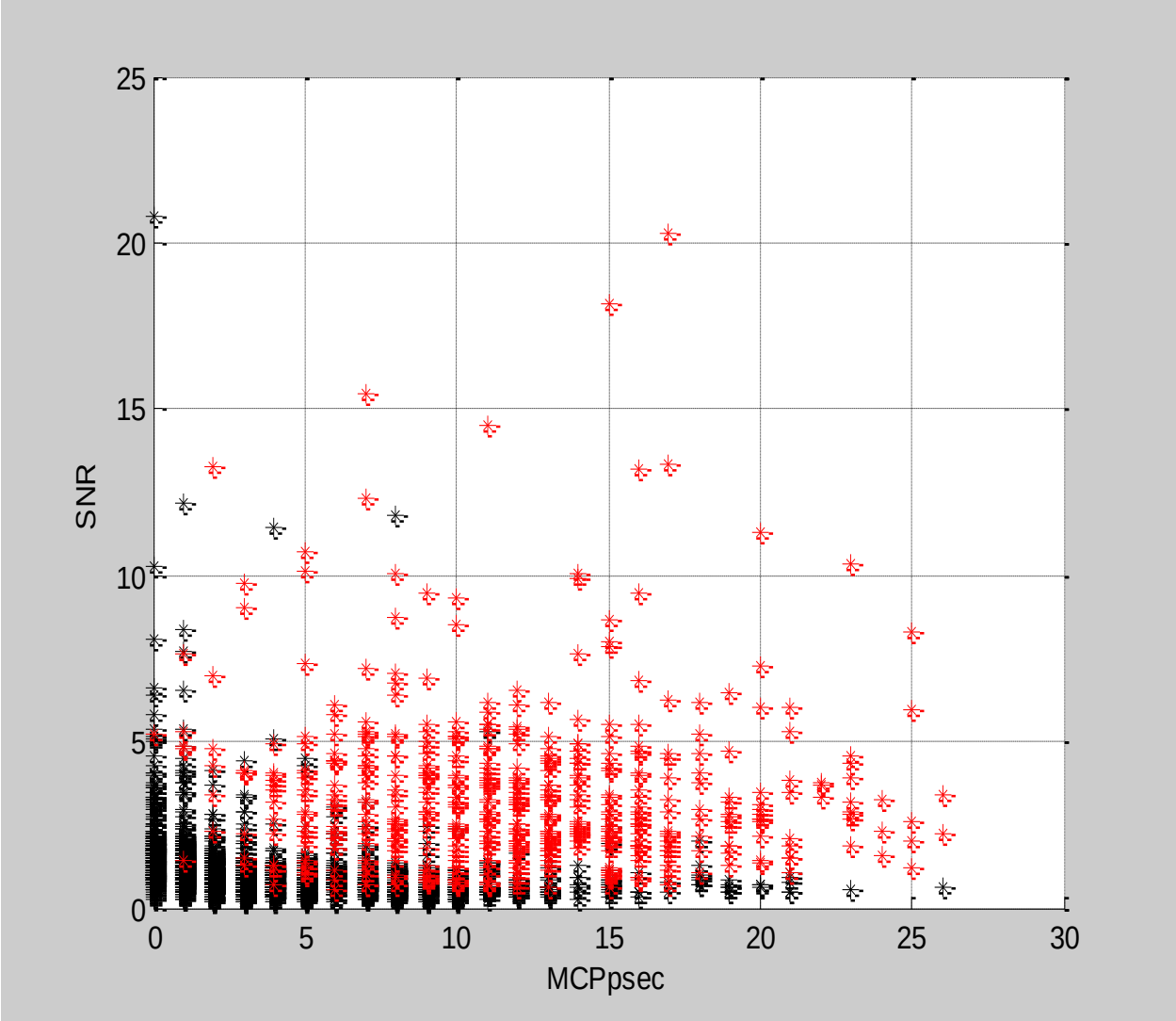

Figure 4.6. Red:spikes. Black: non spikes. Data separation between spikes and non spikes becomes evident at high levels of MCPsec. At high levels of MCPpsec spikes have higher SNR than non spikes. This could arise from non spikes which have high levels of noise and thus high MCPpsec but low SNR. Spikes with high MCPpsec tend to have high SNR.

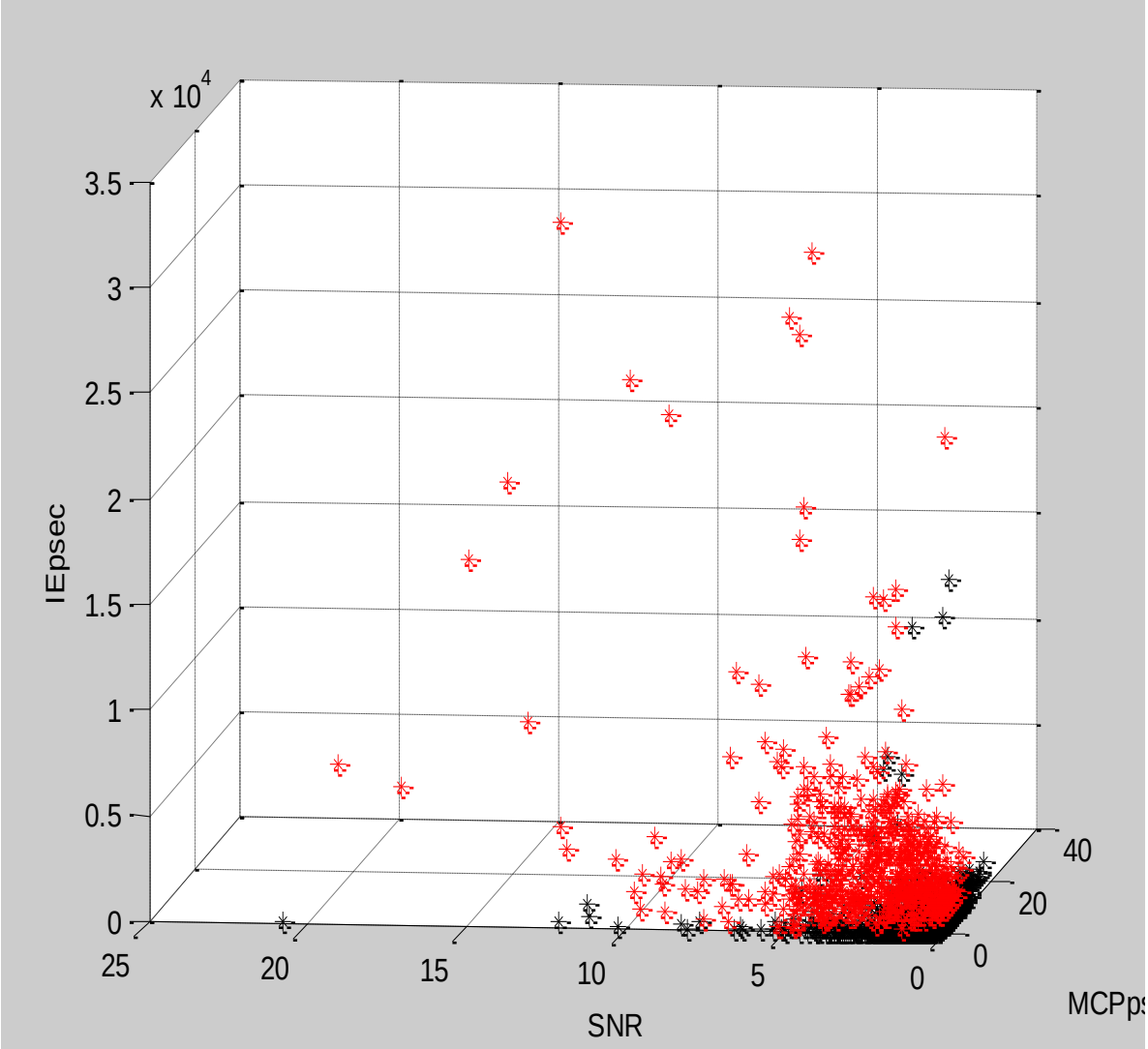

Figure 4.7. Red:spikes. Black: non spikes. It is possible to observe data separation between spikes and non spikes along the vertical IEpsec axis. Spikes extend into regions of larger IEpsec.

4.2 Algorithm Validation

Validation of the algorithm was two-folded: the first part tested the ability of SVM to classify data into spikes and non spikes, the second part tested the ability of the algorithm to detect spikes in comparison to human markers.

SVM 10-Fold Cross Validation

As mentioned in chapter 3, the SVM algorithm was trained with 2300 training samples of which 80% were non spikes and 20% were spikes. These samples were selected using SNEO threshold detection and classified as spikes or non spikes by a single observer. Classification made by SVM is compared to the manual classification. The 10-fold cross validation measures the ability of SVM to classify the data available. More importantly, cross validation also reveals whether data is separable/ classifiable given the chosen features; this is not always the case. The example provided in chapter 3 figures 3.12-3.15 showed data which could be separated into children and adults given height and weight values. However, if we

had data about children between the ages 2-4 and children between the ages 4-6, it would be harder to separate. These two age groups are likely to overlap on height and weight and could not be easily separated.Each training sample consists of:

Training Sample= [Feature Vector, Manual Classification] which expanded is

Training Sample= [SNR, IEpsec, MCPpsec, MTimeMCP, Manual Classification]

We executed SVM in Matlab and we ran a 10-fold cross validation. The 2300 samples were distributed randomly into 10 groups of approximate equal size.The steps are the following:

1. 9 groups are chosen as a TRAINING SET while the remaining group is determined to be a TESTING SET.
2. SVM is trained with the training set feature vector and manual classification. Once training is finalized, a SVM structure is generated and SVM is ready to classify new data.
3. Only the testing set feature vector is passed onto SVM for classification.
4. Then, the testing set manual classification is compared to the output produced by SVM. Several metrics are calculated to measure the performance of the automated classification. See table 4.1 for detail on cross-validation metrics.
5. This entire sequence is repeated 10 times; every time having a different group as a testing set.
6. Finally, the average metrics for the 10 combinations is computed and reported.

Table 4.1.Cross validation statistics: definitions and abbreviations.

Abbreviation	**Definition**	**Formula**
Absolute values		
TP	Number of true positives	
FP	Number of false positives	
FN	Number of false negatives	
TN	Number of true positives	
Nmarks	Number of marks	$Nmarks = TP + FN + FP + TN$
Metrics. Value ranges 0-1.		
TPR	True positive rate	$TPR = \frac{TP}{TP + FN}$
FPR	False positive rate	$FPR = \frac{FP}{TP + FP}$
FNR	False negative rate	$FNR = \frac{FN}{Nmarks}$
SPC	Specificity	$SPC = \frac{TN}{TN + FP}$
SN	Sensitivity	$SN = \frac{TP}{TP + \boldsymbol{FN}}$
PPV	Positive prediction value	$PPV = \frac{TP}{TP + \boldsymbol{FP}}$

While all the metrics mentioned in table 4.1 provide important information, we will focus on PPV and SN as discussed in chapter 3. The product of these two yields AROC; a measure of the test's performance.

Results: 10-fold Cross-Validation

10-fold cross validation was done with the four features SNR, IEpsec, MCPpsec, and MTimeMCP (see table 4.2 for explanation of abbreviations). These features were defined and illustrated in chapter 3. Average PPV was 0.9567 ± 0.0118 and average SN was 0.9795 ±0.0088. Remember that perfect PPV and SN are equal to 1. These results yielded AROC = 0.9371. Table 4.3 provides detailed results of cross validation.

Table 4.2.Candidate feature names and abbreviations

Abbreviation	Definition
SNR	Signal to noise ratio
IEpsec	Integrated candidate energy per unit time
MCPpsec	Number of mean-crossing points per unit time
MTimeMCP	Median time between mean-crossing points (seconds)

Table 4.3. Average metrics for cross-validation with 4 features: SNR, IEpsec, MCPpsec, MTimeMCP.

Metric	Average	Standard deviation (STDV)
Nmarks	223.4	11.4426
TP	209.5	10.4376
FP	**9.5**	**2.7183**
FN	4.4	1.9551
TPR	0.9380	0.0157
FPR	0.0424	0.0115
FNR	0.0196	0.0083
PPV	**0.9567**	**0.0118**
SN	**0.9795**	**0.0088**
SPC	0.9576	0.0115

The repetition of 10-fold cross validation (trial 1- trial 5) yielded different numerical results. See table 4.4. This is because early in the validation stage samples are assigned randomly to groups. So for every repetition, samples are distributed differently amongst groups. However, the numerical difference does not indicate a real difference. The mean SPC and mean SN vary within the standard deviation window.

Table 4.4. Five trials of 10-fold cross validation.

	TRIAL 1	TRIAL 2	TRIAL 3	TRIAL 4	TRIAL 5
< PPV > ± STDV	95.89 ± 1.35	95.64 ± 1.75	95.70 ±1.88	95.74 ± 1.13	95.67 ± 1.18
< SN > ± STDV	98.00 ± 0.97	97.92 ± 0.99	97.90 ± 0.47	97.99 ± 1.34	97.95 ± 0.88

We can report that SVM classification with the four aforementioned features yields: average PPV= 95 ± 1 % and average SN= 98 ± 1 %. Then, average AROC= 0.93 ± 0.02 .

Table 4.5. Performance summary 4-feature SVM classification

Performance Summary
PPV= 95 ± 1%
SN= 98 ± 1 %.
AROC= 0.93 ± 0.02

These results are satisfactory and provide support for the use of SVM in classification of new data. High PPV and SN indicate that the SVM structure has an adequate distribution of training samples and is able to generate an appropriate separating hyperplane.

Results in table 4.5 show a slightly lower PPV compared to SN. This arises from a relatively larger number of FPs. SVM is able to detect the majority of spikes present (high SN). However, it also classified erroneously some non spikes giving rise to FPs (lower PPV). These are likely to be artifacts and contaminants with features (SNR, IEpsec, MCPpsec, and MTimeMCP) similar to spikes.

4.3 Feature Vector Assessment

Results for 10-fold cross validation of SVM with the four features SNR, IEpsec, MCPpsec, MTimeMCP were: average PPV= 95 ± 1 %, average SN= 98 ± 1 % and AROC= 0.93 ± 0.02.

These results were deemed satisfactory. Nevertheless, before proceeding into SVM classification of new data we assessed the legitimacy of every feature in the feature vector. In other words, we investigated whether a feature improved SVM performance by providing useful information.

For this purpose we conducted a series of cross validations using different feature vectors. See table 4.6 for results summary. Figure 4.8 and 4.9 illustrate the results. Figure 4.8 suggests that several combinations of features have comparable performance. Lowest performance when only used MCPpsec or MTimeMCP .Combinations of two or more features yields 90% or higher AROC. Figure 4.9 shows that for the majority of feature combinations SN is always higher than PPV. This observation suggests that SVM is able to detect the majority of spikes. However, it also marks non spikes erroneously; thus, SVM has lower ability to distinct between spikes and non spikes. As we mentioned in chapter 3, we do not expect perfect performance from SVM. Thus, the presence of a few FPs is expected.

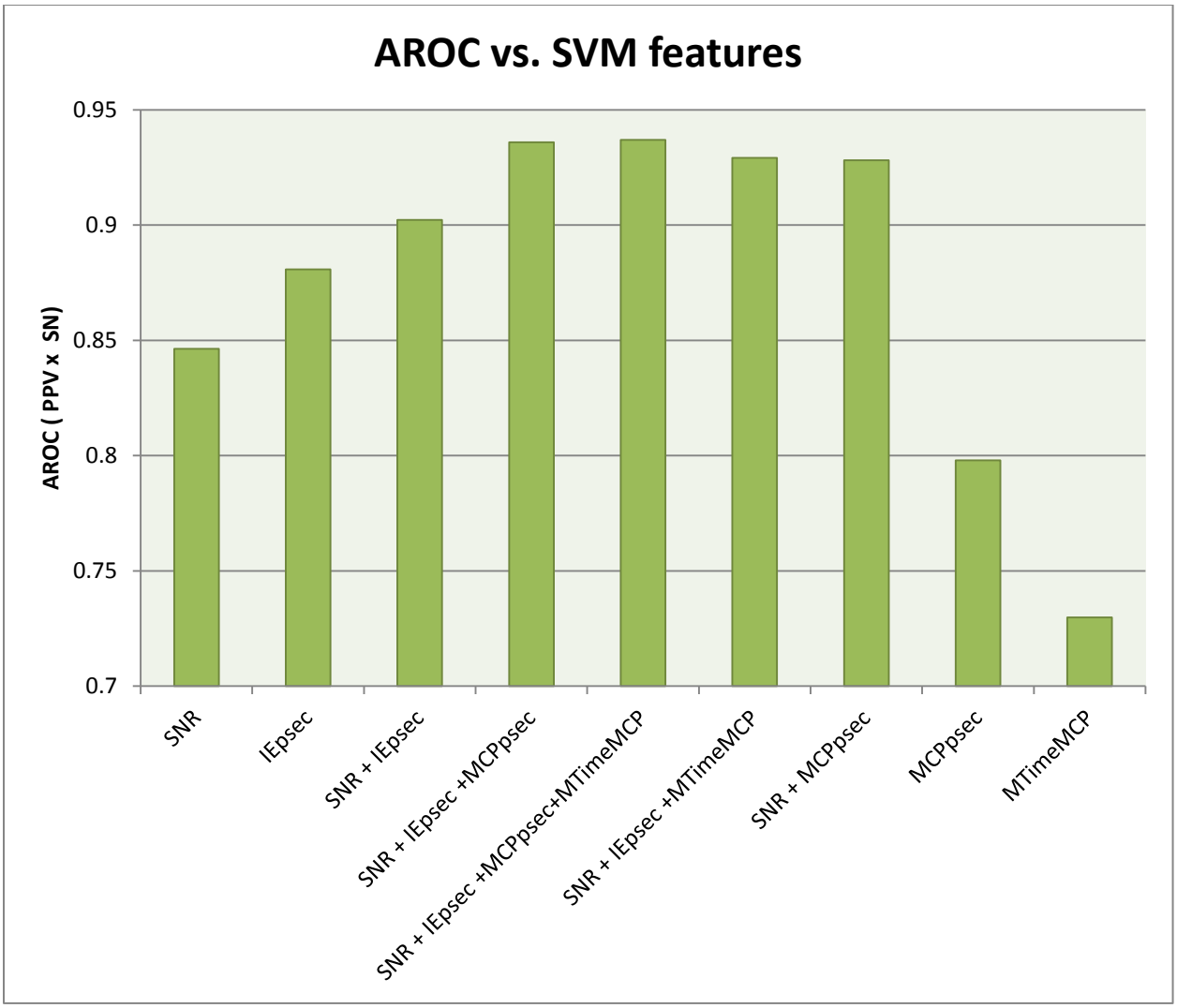

Figure 4.8. Changes in SVM performance for different combinations of feature vectors.

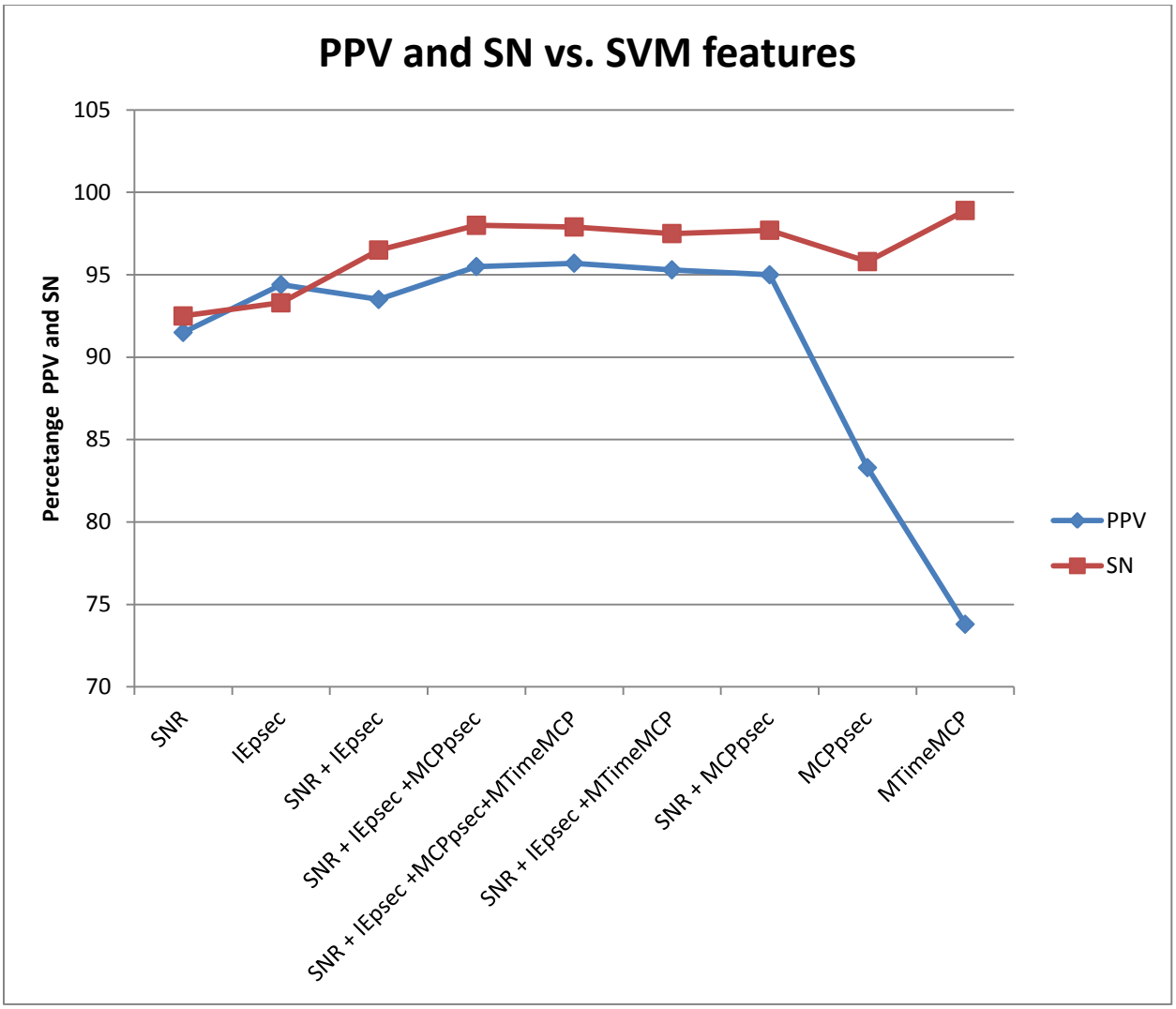

Figure 4.9. Changes in PPV and SN for different combinations of feature vectors. Note interrelation between PPV and SN. Also, for the majority of cases SN is always higher than PPV.

Table 4.6. Summary of Cross validation for different feature vectors.

Feature vector = [SNR]					
Cross-validation	TRIAL 1	TRIAL 2	TRIAL 3	TRIAL 4	TRIAL 5
< PPV > ± STDV	91.84 ± 2.87	91.12 ± 2.17	91.65 ± 1.88	91.22 ± 2.48	91.43 ± 3.30
< SN > ± STDV	91.70 ± 3.87	93.46 ± 2.36	92.80 ± 3.44	92.87 ± 2.57	91.78 ± 4.12
Feature vector = [IEpsec]					
< PPV > ± STDV	94.49± 1.89	94.43 ± 1.27	94.36± 2.37	94.51 ± 1.88	94.16 ± 1.69
< SN > ± STDV	93.43± 2.33	93.41 ± 3.29	93.31± 3.41	92.59± 2.76	93.79± 2.40
Feature vector = [SNR, IEpsec]					
< PPV > ± STDV	93.50 ± 1.29	93.44 ±1.31	93.52 ± 2.32	93.52 ± 1.97	93.52 ± 1.25
< SN > ± STDV	96.46 ± 1.35	96.39 ± 0.99	96.48 ± 1.36	96.45 ± 1.16	96.54 ± 1.38
Feature vector = [SNR, IEpsec , MCPpsec]					
< PPV > ± STDV	95.45 ± 1.16	95.41± 2.14	95.51 ± 1.32	95.50 ± 1.23	95.38± 1.41
< SN > ± STDV	97.91± 1.00	97.91± 0.80	97.95± 0.80	98.05 ± 1.23	97.96± 1.16
Feature vector =[SNR, IEpsec, MCPpsec, MTimeMCP]					
< PPV > ± STDV	95.89 ± 1.35	95.64 ± 1.75	95.70 ±1.88	95.74 ± 1.13	95.67 ± 1.18
< SN > ± STDV	98.00 ± 0.97	97.92 ± 0.99	97.90 ± 0.47	97.99 ± 1.34	97.95 ± 0.88
Feature vector =[SNR, IEpsec, MTimeMCP]					
< PPV > ± STDV	95.24± 0.46	95.26± 1.87	95.22± 1.22	95.34± 0.86	95.28± 1.76
< SN > ± STDV	97.52±0.90	97.43 ± 1.19	97.51± 0.98	97.45±1.44	97.54 ±1.39
Feature vector =[MCPpsec]					
< PPV > ± STDV	83.32 ±2.48	83.31 ±1.92	83.26 ± 2.33	83.28 ±1.63	83.27± 1.88
< SN > ± STDV	95.82 ±1.96	95.80± 1.26	95.82 ±1.36	95.82 ±1.12	95.87 ±1.60
Feature vector =[MTimeMCP]					
< PPV > ± STDV	73.89± 3.45	73.87 ±2.67	73.64± 3.31	73.94± 3.26	73.97± 3.55
< SN > ± STDV	98.93 ±1.18	98.87± 0.95	98.86± 0.77	98.95± 1.09	98.88± 1.12
Feature vector = [SNR, MCPpsec]					
< PPV > ± STDV	95.16 ±1.29	95.15± 2.29	95.13 ±1.25	95.28± 1.88	95.06 ±1.11
< SN > ± STDV	97.72 ±0.84	97.68 ±0.96	97.68 ±0.80	97.65± 0.82	97.85± 1.23

4.4 Additional Discrimination

The final step in the algorithm (post SVM classification) consisted of an additional discrimination step. As discussed in chapter 3, this additional discrimination was designed to possibly reduce the number of FPs. We tested the impact of this final step by running it following SVM classification. Table 4.6 contrasts the 10-fold cross validation results for SVM classification only against SVM classification plus additional step. The final discrimination step does not affect significantly the results. We observe a small numerical difference for metrics like PPV (0.9567 vs. 0.9676). However, a numerical difference does not indicate a real difference. The metrics vary within the standard deviation window.

Table 4.7. Cross validation results comparison. SVM classification vs. SVM classification + add. discrimination

SVM classification				**SVM classification + add. discrimination**	
Metric	**Mean**	**Standard deviation (STDV)**		**Mean**	**Standard deviation (STDV)**
Nmarks	223.4	11.4426		223.4	11.4426
TP	209.5	10.4376		211.4	10.88
FP	9.5	2.7183		7.1	2.2336
FN	4.4	1.9551		4.9	1.9692
TPR	0.9380	0.0157		0.9464	0.0126
FPR	0.0424	0.0115		0.0317	0.0097
FNR	0.0196	0.0083		0.0219	0.0086
PPV	**0.9567**	**0.0118**		**0.9676**	**0.0099**
SN	**0.9795**	**0.0088**		**0.9773**	**0.0089**
SPC	0.9576	0.0115		0.9683	0.0097

4.5 Algorithm Validation: Automated Results vs. Standard and Parameter Analysis

As mentioned in chapter 3, several segments of data were marked manually by three observers experienced in recognizing spikes. The manual marks were pooled in together and the spike clusters marked by the three observers regardless of any small time difference were selected. Then, the manual marks were compared to automated marks generated by the algorithm. This is a validation of the algorithm in its entirety; in contrast to the 10-fold cross validation which only investigated SVM performance.

The algorithm was run for 840 combinations of parameters in order to determine the optimal combination. Parameters used:
k= { 3 , 6 , 9 , 12 , 15 , 18}
DT= {0.3 , 0.5 , 0.7, 0.9 , 1.1, 1.3 , 1.5}
windowL= {0.25 , 0.5, 0.75, 1} (window length=2 x windowL)

Next, AROC (PPV x SN) was calculated and plotted against k and DT. In this case, AROC is a measure of the algorithm's performance for a set of parameters. AROC 0.8 or higher is regarded as a good performance, which results from 0.9% SN and 0.9% PPV.

Figures 4.10 through 4.13 illustrate the relation between AROC and the parameters. From these we can observe that AROC is dependent on k, DT. The maximum AROC values observed were in the range 0.7-

0.76 for k=5 and DT=1.5. These were deemed satisfactory. This is the performance one could expect when running a new data set on the algorithm with those parameters.

Furthermore, figure 4.11 reveals important information regarding the robustness of the algorithm The AROC surface plot is nearly flat near high DT and low k. This allows the user to select parameter values within this region and get good algorithm performance. The algorithm is not oversensitive to these parameters. Table 4.8 summarizes the optimal algorithm performance for each data set.

Table 4.8. Optimal performance for each set of standards

File	k	DT (s)	windowL (s)	Aroc	Sens	PPV	TP	FP	FN	Ncands	Nspks
05.22.09b	18	0.9-1.5	0.5	0.89470	0.91764	0.975	78	2	7	355	80
05.03.11	3	1.5	0.75	0.88506	0.92968	0.952	238	12	18	276	250
05.29.09	3	1.3	0.5	0.85388	0.89843	0.95041	115	6	13	258	121
04.14.09	3,15	1.3	1	0.84424	0.97647	0.86458	83	13	2	265	96
06.01.11	15	1.5	1	0.69879	0.89024	0.78494	73	20	9	122	93

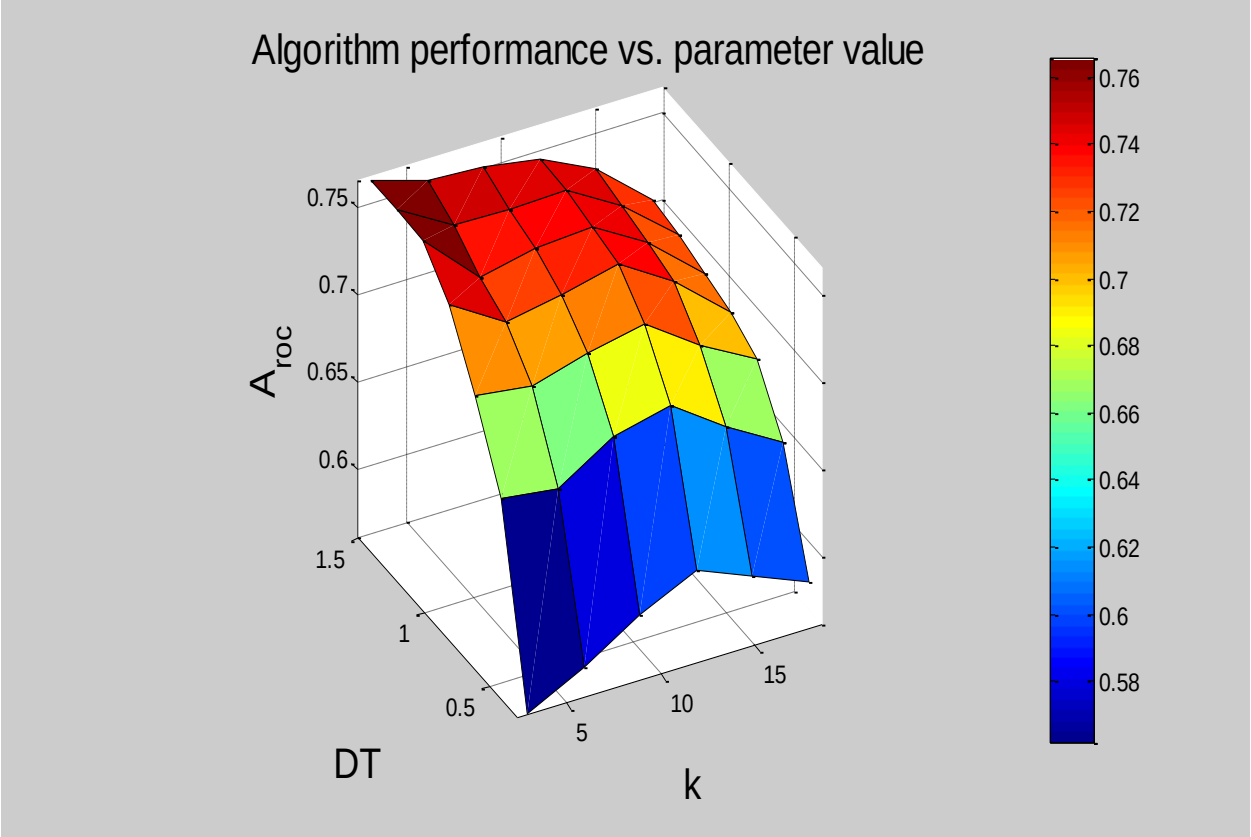

Figure 4.10. AROC surface for parameters DT, k.

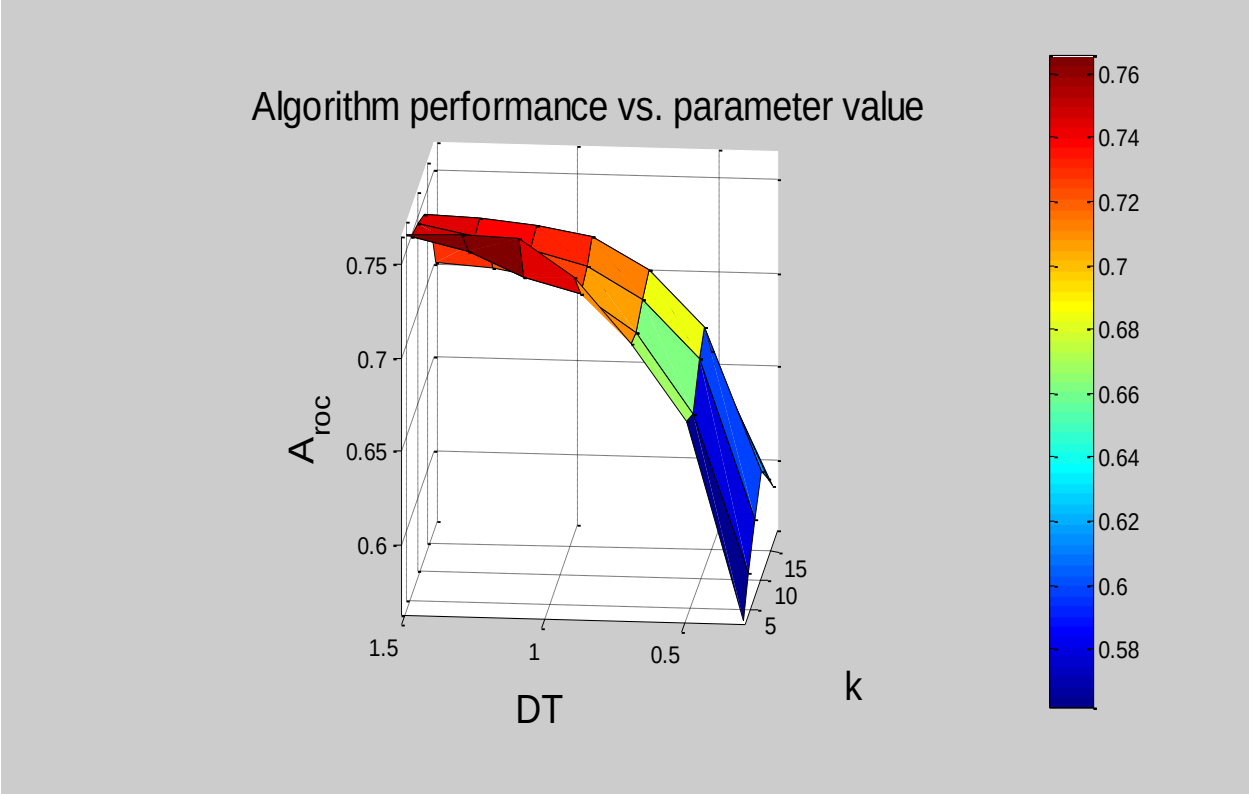

Figure 4.11. AROC is directly proportional to DT. Future work should be carried with DT=1.5

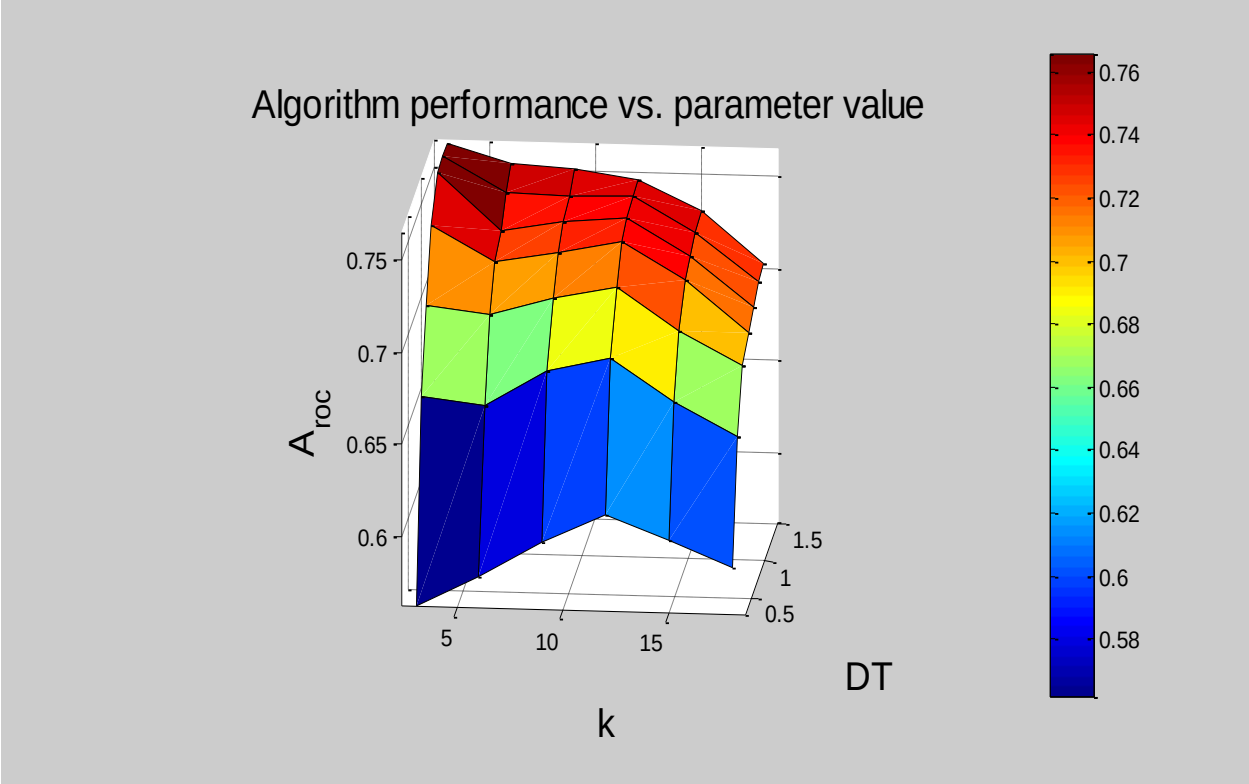

Figure 4.12. Not a clear relationship between AROC and k. However, highest AROC at small k. Future work could be carried with k=5.

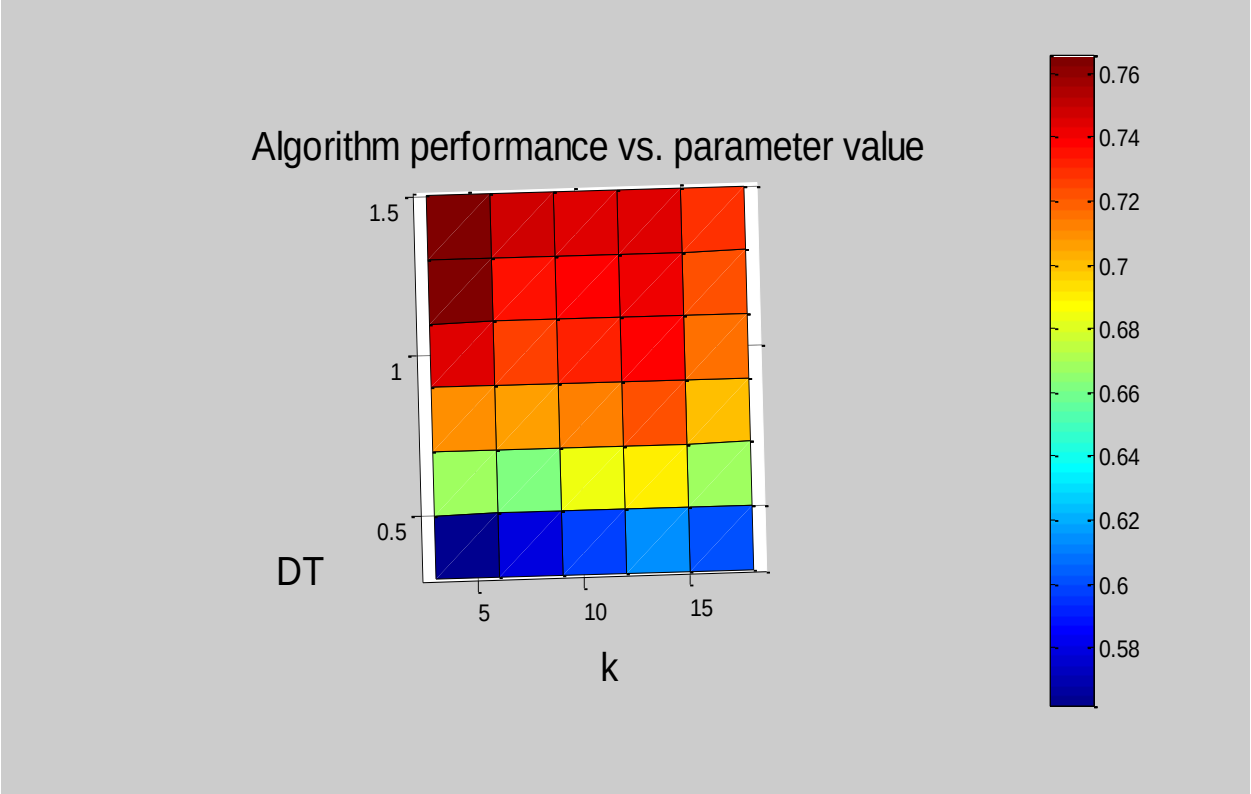

Figure 4.13. Highest algorithm performance at low k, high DT (observe maroon blocks in plot)

Validation Overview

As we discussed in chapter 3 the algorithm consisted of the following processes:

Filtered Signal →SNEO threshold detection + SVM + additional discrimination = Spike cluster information

Now, the algorithm is validated and can be used to analyze spike activity in ischemic intestines.

Chapter 5

Preliminary Results: Induced Ischemia and Spike Activity

5.1 Ischemic Intestine Data Analysis

Table 5.1.Details Regarding Preliminary spike detection with algorithm.

	Channels	FILE	5min	5min	5min	5min	TOTAL
		PIG 1					
baseline	49chan	04.14.09_a	60-360s	360-660s	1000-1300s	1300-1600s	
		# of spikes detected	9	2	14	21	46
75%ischemia	49chan	04.14.09_d	60-360s	360-660s	700-100s	1000-1300s	
		# of spikes detected	364	22	11	93	490
		PIG 2					
baseline	49chan	05.29.09a	60-360s	500-800s	1000-1300s	1400-1700s	
		# of spikes detected	0	1	0	0	1
segmental	49chan	05.29.09b	60-360s	500-800s	1000-1300s	1800-2100s	
		# of spikes detected	512	544	135	18	1209

Spike Activity: Ischemic Intestine vs. Baseline

(Figures 5.1 and 5.2). Number of spike clusters per minute per channel. For 20-minute long experiments. Compared to spike rate in baseline recordings. Vanderbilt experiments 04.14.09 and 05.29.09.

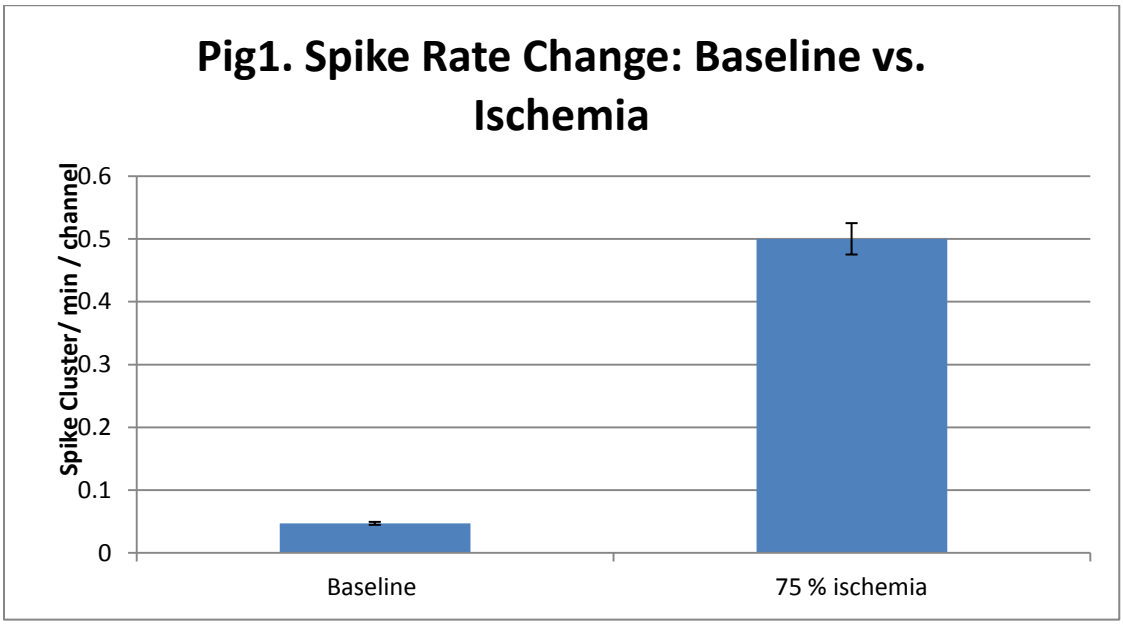

Figure 5.1. Number of spike clusters per minute per channel. For 20-minute long experiment.

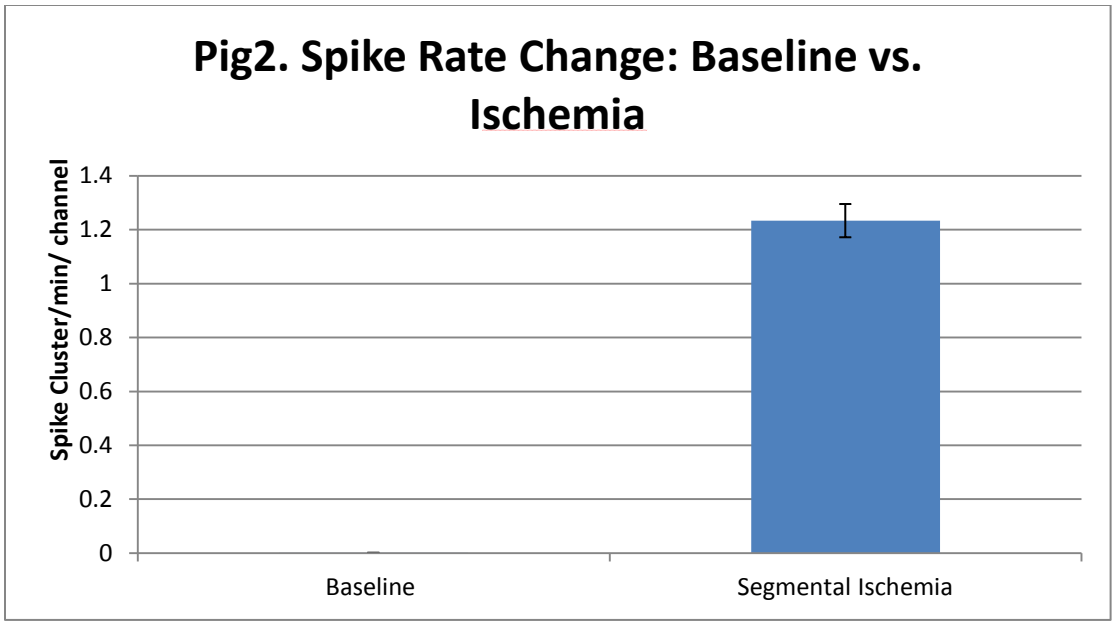

Figure 5.2. Number of spike clusters per minute per channel. For 20-minute long experiment.

Spike Rate in Ischemic Intestine

(Figure 5.3 and 5.4) Average number of spikes per channel during partial ischemia experiment (75%). Spike rate changes throughout experiment. (x axis is the time coordinate during the experiment). Vanderbilt experiments 04.14.09 and 05.29.09.

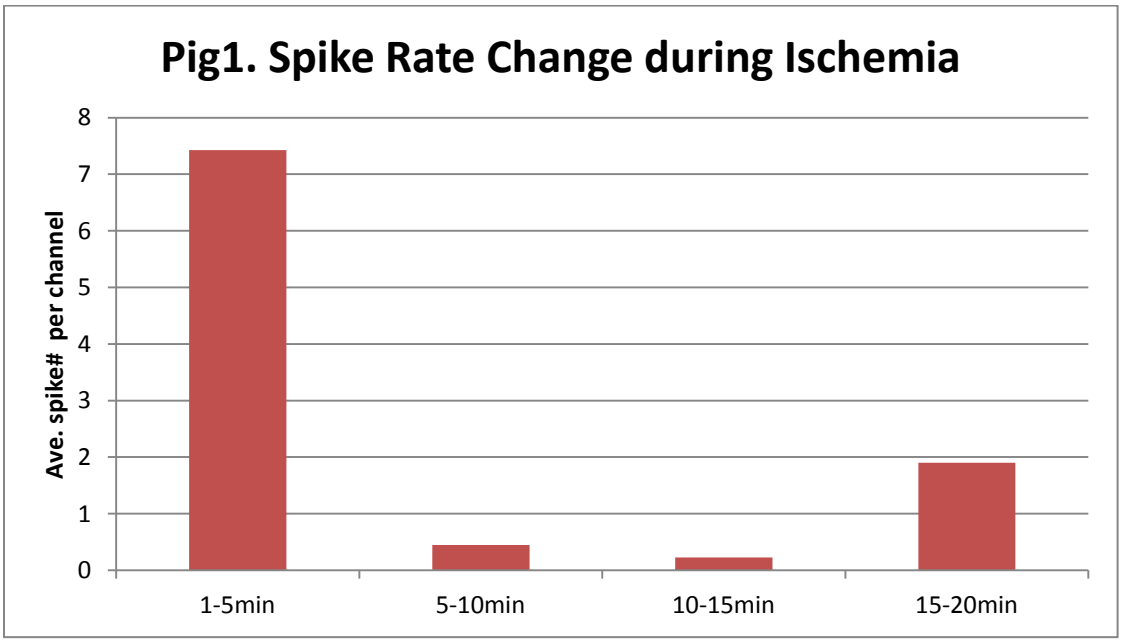

Figure 5.3. Average number of spikes per channel during partial ischemia experiment (75%).

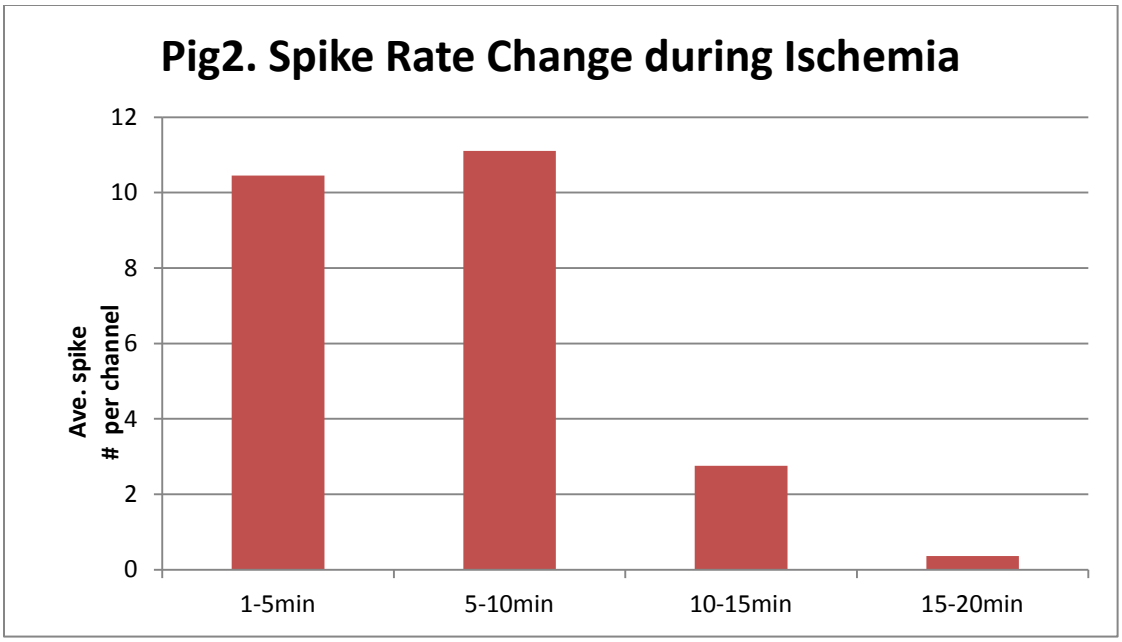

Figure 5.4. Average number of spikes per channel during partial ischemia experiment (75%).

5.2 Spatial Spike Propagation Analysis

Once spike detection has been conducted it is possible to analyze the wave's spatial propagation. A preliminary attempt to model spike spatial propagation was performed by using the cycle partitioning algorithm REGROUPS (Erickson 2010). This algorithm was designed for gastric slow wave activity but could be appropriate for spike analysis; testing to be conducted in the future. Figure 5.5 provides an example of how REGROUPS can partition spike wave fronts. Figure 5.6 illustrates the spatial propagation of the 3 wavefronts detected by REGROUPS.

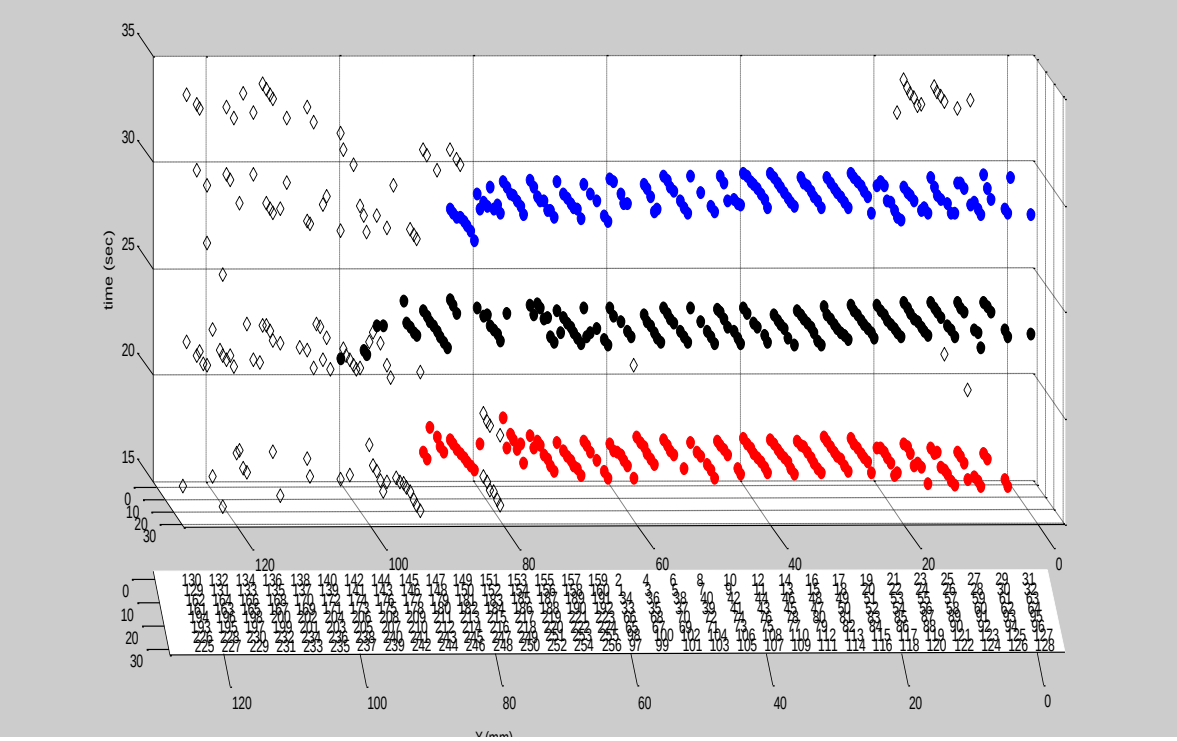

Figure 5.5. Cycle Partitioning analysis conducted with REGROUPS. Electrode placement information is necessary.

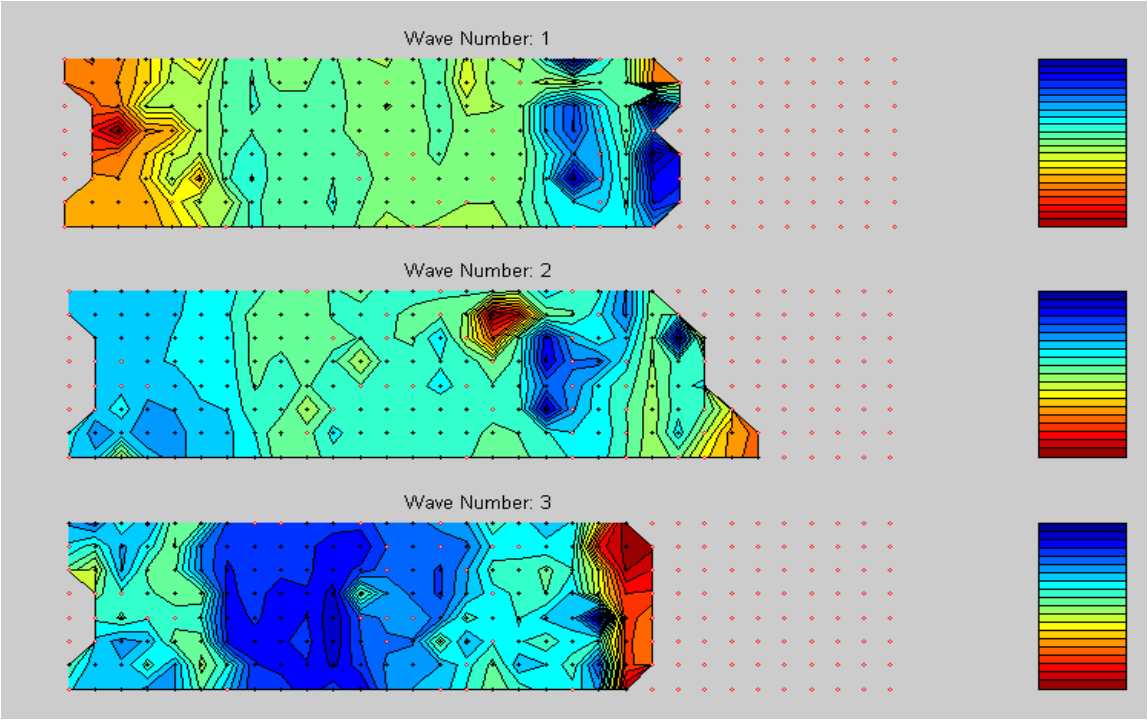

Figure 5.6. Spatial propagation of spike wave fronts detected by REGROUPS in figure 5.5. Scale red to blue indicates time delay. Red: first. Blue: last.

5.3 Results Overview

The design and validation of the spike detection algorithm presented in this thesis was the first step in the process to investigate the effects of intestinal ischemia on spike activity. Based on AROC analysis we deemed the algorithm satisfactory it is current state. Detailed discussion of the algorithm validation will be published shortly. Moreover, the spike detection algorithm has been incorporated to the GEMS v1.6 software (GastroIntestinal Mapping Suite) for additional testing. Figure 5.7 shows data display in GEMS.

The ischemia analysis results presented here are preliminary and are intended to show possible applications of the algorithm. Future research will involve the use of the algorithm for spike rate analysis and spike spatial propagation analysis.

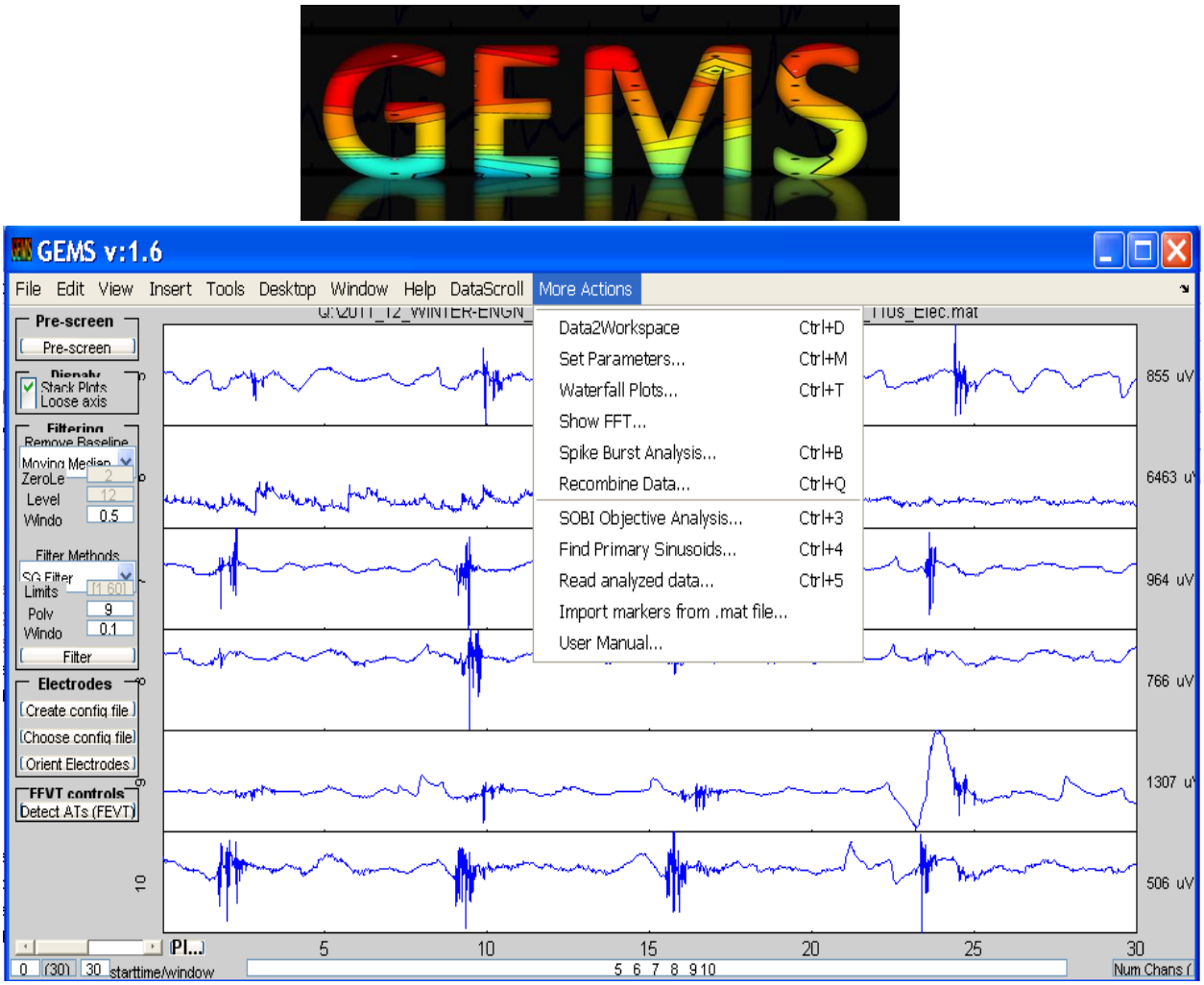

Figure 5.7

Acknowledgments

Dr. Jonathan C. Erickson. (research project advisor, thesis advisor, literature suggestions, Matlab wizard,etc).

R.E. Lee Undergraduate Research Program at Washington and Lee University (funded summer 2011 research)

Department of Physics- Engineering, Washington and Lee University. Lexington,VA.

Departments of Physics, Vanderbilt University. Nashville,TN.

Departments of Surgery, Vanderbilt University School of Medicine. Nashville,TN.

Alan Bradshaw and Bill Richards (original experiments and sharing data).

Dr. Chibuike Obioha (suggesting the investigation based on initial observations).

Auckland Bioengineering Institute, the University of Auckland, Auckland, New Zealand.

Tim Angeli (general help, progress feedback and support with everything related to small intestine).

Greg O'Grady (immensely helpful expert discussion and input, literaturesuggestions).

Leo Cheng (lab leader, sharing data and helpful comments).

Bibliography

Bortoff, A. (1967). Configuration of Intestinal Slow Waves Obtained by Monopolar Recording Techniques. *American Journal of Physiology , 213* (1), 157-162.

Cabot, R. M., & Kohatsu, S. (1978). The Effects of Ischemia on the Electrical and Contractile Activities of the Canine Small Intestine. *The American Journal of Surgery , 136*, 242-246.

Chou, C. C. (1982). Relationship Between Intestinal Blood Flow and Motility. *Annual Review of Physiology , 44*, 29-42.

Daniel, E. E., & Chapman, K. M. (1963). Electrical Activity of the Gastrointestinal Tract as an Indication of Mechanical Activity. *American Journal of Digestive Diseases , 8*, 54-102.

Du, P., O'Grady, G., Egbuji, J. U., Lammers, W. J., Budgett, N. P., Windsor, J. A., et al. (2009). High-resolution Mapping of In Vivo Gastrointestinal Slow Wave Activity Using Flexible Printed Circuit Board Electrodes: Methodology and Validation. *Annals of Bioengineering* , Published Online.

Erickson, J. C., Obioha, C., Goodale, A. L., Bradshaw, A., & Richards, W. O. (2009). Detection of Small Bowel Slow-Wave Frequencies from Noninvasive Biomagnetic Measurements. *IEEE Transactions on Biomedical Engineering , 56*, 2181-2189.

Erickson, J. C., O'Grady, G., Du, P., Chibuike, O., Qiao, W., Richards, W. O., et al. (2009). Falling-Edge, Variable Threshold (FEVT) Method for the Automated Detection of Gastric Slow Wave Events in High-Resolution Serosal Electrode Readings. *Annals of Biomedical Engineering , 38* (4), 1511-1529.

Erickson, J. C., O'Grady, G., Du, P., Egbuji, J. U., Pullan, A. J., & Cheng, L. K. (2010). Automate Gastric Slow Wave Cycle Partitioning and Visualization for High-resolution Activation Time Maps. *Annals of Biomedical Engineering* , Published Online.

Farrugia, G. (2008). Interstitial Cells of Cajal in Health and Disease. *Neurogastroenterology and Motility , 20* (Supplement 1), 54-63.

Groh, W. J., Takahashi, I., Sarna, S., Dodds, W. J., & Hogan, W. J. (1984). Computerized Analysis of Spike-Brust Activity of the Upper Gastrointestinal Tract. *Digestive Diseases and Sciences , 29* (5), 422-426.

Guisan, Y. J., Hreno, A., & Gurd, F. N. (1975). Effect of acute ischemia on the motility of the small bowel in the awake dog. *Eur.Surg.Res. , 7*, 23-33.

Jabloun, F., Cetin, E., & Erzin, E. (1999). Teager Energy Based Feature Parameters for Speech Recognition in Car Noise. *IEEE Signal Processing Letters , 6* (10), 259-261.

Kyi, J. K., & Daniel, E. E. (1970). The effects of ischemia on intestinal nerves and electrical slow waves. *Am.J.Dig. , 15*, 959-981.

Lammers, W. J., & Slack, J. (2001). Of Slow Waves and Spike Patches. *News in Physiological Sciences , 16*, 138-144.

Lammers, W. J., & Stephen, B. (2008). Origin and Propagation of Individual Slow Waves Along the Intact Feline Small Intestine. *Experimental Physiology* , 334-346.

Lammers, W. J., El-Kays, A., Manefield, G. W., Arafat, K., & El-Sharkawy, T. Y. (1997). Disturbances in the Propagation of the Slow Wave During Acute Local Ischaemia in the Feline Small Intestine. *European Journal of Gastroenterology & Hepatology , 9*, 381-388.

Lammers, W. J., Michiels, B., Voeten, J., Ver Donck, L., & Schuurkes, J. A. (2008). Mapping Slow Waves and Spikes in Chronically Instrumented Conscious Dogs: Automated On-line Electrogram Analysis. *Medical & Biological Engineering & Computing , 46*, 121-129.

Lammers, W. J., Ver Donck, L., Schuurkes, J. A., & Stephen, B. (2003). Longitudinal and Circumferential Spike Patches in the Canine Small Intestine in Vivo. *American Journal of Physiology: Gastrointestinal and Liver Physiology , 285*, G1014-G1027.

Lammers, W. J., Ver Donck, L., Schuurkes, J. A., & Stephen, B. (2005). Peripheral Pacemakers and Patterns of Slow Wave Propagation in the Canine Small Intestine in Vivo. *Canadian Journal of Physiology and Pharmacology , 83*, 1031-1043.

Liang, J., Cheung, J. Y., & Chen, J. D. (1997). Detection and Deletion of Motion Artifacts in Electrogastrogram. *Annals of Biomedical Engineering , 25*, 850-857.

Meissner, A., Bowes, K. L., & Sarna, S. K. (1976). Effects of ambietn and stagnat hypoxia on the mechanical and electrical activity of the canine upper jejunum. *Can.J.Surg. , 19*, 316-321.

Nenadic, Z., & Burdick, J. W. (2005). Spike Detection Using the Continous Wavelet Transform. *IEEE Transactions on Biomedical Engineering , 52* (1), 74-87.

Summers, R. W., Cramer, J., & Flatt, A. J. (1982). Computerized Analysis of Spike Burst Activity in the Small Intestine. *IEEE Transactions on Biomedical Engineering , BME-29* (5), 309-314.

Szurszewski, J., & Steggerda, F. R. (1968). The Effect of Hypoxia on the Electrical Slow Wave of the Canine Small Intestine. *American Journal of Digestive Diseases , 13* (2), 168-177.

Taxi, J. (1952). Cellules de Schwann et “cellules interstitielles de Cajal” au niveau des plexus nerveux de la musculeuse intestinale du cobaye: Retour aux définitions. *Arch Anat Microsc , 41*, 281–304.

Teager, H. M. (1980). Some observations on oral air flow during phonation. *IEEE Trans. Acoust., Speech, Signal Processing , ASSP-28*, 599-601.

Thuneberg, L. (1999). One hundred years of interstitial cells of Cajal. *Microscopy Research and Techniques , 47*, 223–238.

Yakovle, V. G. (1977). Algorithm for Detecting Spikes of Physiological Curves. *Avtomatika i Telemekhanika* (12), 94-105

Other Sources Relevant

Hamel,Lutz. (2009). *Knowledge Discovery with Support Vector Machines.* Hoboken, NJ: John Wiley & Sons.

Hertz, J., Krogh, A., & Palmer, R. G. (1991). *Introduction to the Theory of Neural Computation.* Redwood City, CA: Addison-Wesley Publishing Company.

Addison, P. S. (2002). *The Illustrated Wavelet Transform Handbook: Introductory Theory and Applications in Science, Engineering, Medicine and Finance.* New York: Taylor & Francis Group.

Wang,Zhishun. (2001).Blind Separation of Slow Wave and Spikes from Gastrointestinal Myoelectrical Recordings.*IEEE Transactions of Information Technology on Biomedicine, 5(2),*133-137.

Belouchrani,Adel,Abed-Meraim,Cardoso Jean-Francois,Moulines,Eric. (1997). A Blind Source Separation Technique Using Second-Order Statistics. *IEEE Transactions on Signal Processing, 45(2*),434-444.

Image Sources

Figure 1.4 and 2.3Auckland Bioengineering Institute: http://sites.google.com/site/gimappingsuite/research-projects

Figure 1.1 and 1.3 Encyclopedia Britannica: http://www.britannica.com/EBchecked/media/1087/The-human-digestive-system-as-seen-from-the-front and http://kids.britannica.com/comptons/art-53188

Figure 1.2 Mayo Clinic: http://www.mayoclinic.com/health/medical/IM00140

Figure 1.6 GIST Support Int.:http://www.gistsupport.org/for-new-gist-patients/understanding-your-pathology-report-for-gist/diagnosing-gist.php

Figure 1.7 W.J. Lammers Video (Uploaded in 2007): http://www.youtube.com/watch?v=PH6zkPoEOc4

Figure 1.12 Martin P. Mintchev Website: http://www.enel.ucalgary.ca/People/Mintchev/stomach.htm

Figure 2.1 and 2.2 W.J. Lammers 2003

Fig 2.4 W.J. Lammers 1997

Fig. 2.5 Kent Scientific, Medical Supplies Retail: https://www.kentscientific.com/products/

Online Resources

Electro-Mechanical Coupling http://www.enel.ucalgary.ca/People/Mintchev/stomach.htm

SVM classification: www.dtreg.com/svm.htm

Intestinal Ischemia: http://www.mayoclinic.com/health/intestinal-ischemia/ds00459/dsection=causes

Digestive Disease Statistics: National Institute of Diabetes and Digestive and Kidney Diseases. http://digestive.niddk.nih.gov/statistics/statistics.aspx

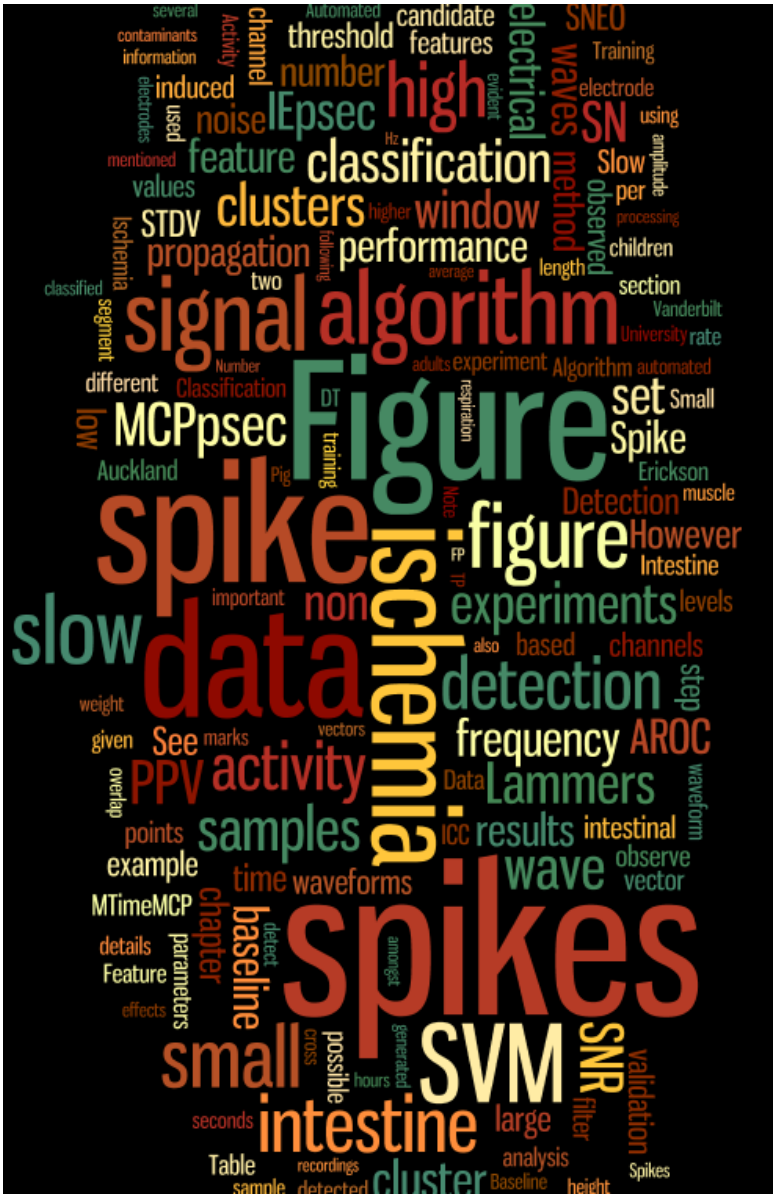

(Thesis wordle by www.wordle.net)